Modelling Primary Production in Seasonally Ice-Covered Regions of the Arctic Ocean and its Response to Climate Change

by

Diane Lavoie
B.A., Laval University, 1992
M.A., University of Quebec at Rimouski, 1997

A Dissertation Submitted in Partial Fulfillment of the
Requirements for the Degree of

DOCTOR OF PHILOSOPHY

in the School of Earth and Ocean Sciences

Modelling Primary Production in Seasonally Ice-Covered Regions of the Arctic Ocean and its Response to Climate Change

by

Diane Lavoie
B.A., Laval University, 1992
M.A., University of Quebec at Rimouski, 1997

Supervisory Committee

Dr. Kenneth L. Denman, Co-supervisor
(School of Earth and Ocean Sciences)

Dr. Andrew J. Weaver, Co-supervisor
(School of Earth and Ocean Sciences)

Dr. Fiona McLaughlin, Departmental member
(School of Earth and Ocean Sciences)

Dr. John F. Dower, Outside member
(Department of Biology)

Dr. Greg M. Flato, Additional member
(School of Earth and Ocean Sciences)

Supervisory Committee

Dr. Kenneth L. Denman, Co-supervisor
(School of Earth and Ocean Sciences)

Dr. Andrew J. Weaver, Co-supervisor
(School of Earth and Ocean Sciences)

Dr. Fiona McLaughlin, Departmental member
(School of Earth and Ocean Sciences)

Dr. John F. Dower, Outside member
(Department of Biology)

Dr. Greg M. Flato, Additional member
(School of Earth and Ocean Sciences)

Abstract

I developed a 1D coupled sea ice-ocean-biological (including ice algae) model to study the controlling effect of sea ice on primary and biogenic particle export production in the western Arctic and the impacts of climate change (reduction in sea ice cover duration and thickness, and in surface freshwater fluxes) on these productions. The model was developed in two steps to maximize validation of model results with as much data as possible. I first developed a coupled snow-ice-ice algae model for bottom landfast ice in Resolute (Canadian Archipelago). Next, I developed and coupled a pelagic component (NPZD type) to the ice algal model. The coupled model was implemented on the Mackenzie shelf in the Canadian Beaufort Sea. And finally, I used simulations of future climate change from the Canadian Global Climate Model (CGCM2) to force the 1D model and obtain projections of future primary production on the Beaufort Sea shelf for two 18-year periods (2042-2059, and 2082-2099).

The model results show that ice algae are light limited at the beginning of the bloom, then fluctuate between light and nutrient limitation, to finally remain nutrient limited toward the end of the bloom. The bottom ice melt rate regulates the maximum biomass attained in Resolute, while biomass accumulation remains low in the Beaufort Sea due to nutrient

limitation. The termination of the bloom is triggered by melting of the snow cover and results from (i) increased ice algal losses due to high bottom ice melt rate and (ii) decreased ice algal growth due to nutrient limitation caused by the formation of a meltwater lens below the ice. The snow and sea ice cover melt and/or break-up also controls the timing of the phytoplankton bloom. However, primary producers on the Beaufort Sea outer shelf are essentially nutrient limited and total annual primary production is controlled in part by nutrient "pre-conditioning" in the previous fall and winter and by the depth of winter convective mixing, that are controlled in part by the supply of fresh water from runoff and ice melt. The spring bloom sometimes represents an important fraction of the total annual primary production, which occurs in great part at the base of the mixed layer. Future projections show an increase in average annual primary production of 6% between the periods 1975-1992 and 2042-2059, and of 9% between 1975-1992 and 2082-2099. The relative contribution of the ice algal and spring phytoplankton blooms to annual primary production is reduced in the future runs due to a reduction in the length of the ice algal growth season (resulting from earlier snow and ice melt) and to a reduction in the replenishment of nutrient to the mixed layer in winter. The duration of the summer subsurface phytoplankton bloom increases, which favours the development of the main copepod species and leads to an increase in export production (16% between 1975-1992 and 2082-2099) that is greater than the increase in primary production. This leads to an increase in averaged simulated *e*-ratio of 10% between the first and last period.

Table of contents

List of Tables

List of Figures

Acknowledgements

Financial support was provided by Fisheries and Oceans Canada, through an educational leave granted to myself, and by the US PARADIGM project through funds granted to my supervisor Ken Denman. Indirect support was also provided by the University of Victoria Climate Lab and by the Meteorological Service of Canada (CCCMA) (physical setting, computer, printers, technical support, etc; special thanks to Mike Berkley and Ed Wiebe for computing support). Observational data sets against which to compare the model results were collected with Science Strategic funds granted to Christine Michel (DFO), and under the Northern Oil and Gas Action Program (NOGAP, project B.6). A special thank goes to Christine Michel for providing ice algae data that were essential for the ice algal model validation. Similarly, a special thank goes to Robie Macdonald (DFO) for providing data from the Beaufort Sea and for his great availability and helpful comments. I also thank Ross Brown (Environment Canada) for his help in obtaining weather data from Resolute, Jacqueline Dumas for her help in obtaining weather data from Tuktoyaktuk, Rick Marsden (Royal Military College of Canada) for mixing coefficient, friction velocity values and meteorological data, and late Grant Ingram (UBC) for the Sea-Bird data. I would like to thank Greg Flato (EC) for his general help in obtaining sea ice related information and data and for his advices on modelling the albedo of ice cover. A special thank goes to Lakshmi Kantha (U. Colorado) for providing the sea-ice model code on which my work is based.

I would like to thank my supervisors, Ken Denman and Andrew Weaver. Thank you Andrew for making me part of your wonderful lab, for your teaching and helpful comments, and for always being ready to help. Thank you Ken for your supervision, availability, patience, and for your wonderful personality: you are a real mentor for me, both in my professional and personal life

I would also like to thank late François Saucier (DFO) for letting me know about the existence of the educational leave in DFO, for believing in me, and for all his help in making this project a reality. I would also like to thank my previous and current

supervisors and directors at MLI (Yvan Simard, Michel Starr, Jacques A. Gagné, Jean-Claude Therriault, Serge Gosselin and Michel Gilbert) for believing in me, and for their continuous encouragements to complete the work after my return to MLI.

Thanks to all my great friends at the University of Victoria for the scientific exchanges, but most importantly, for the great times spent together. These moments were an essential ingredient in keeping a balanced and healthy life.

Warm thanks goes to my mother-in-law, Georgette Eskandar, for taking care of me with her wonderful Lebanese dishes during my stay in Victoria, and for taking care of my baby girl Léa in Rimouski to allow me to complete this thesis. A deep thank also goes to my parents, Estelle Ross and Paul-André Lavoie, for their continuous support, and with my step mother, Monique Saint-Laurent, for taking care of Léa on numerous afternoons in order for me to work on my thesis.

Finally, a deep thank goes to my husband, Michel Eskandar, for his continuous love and support throughout this sometimes-painful process.

I dedicate this thesis to my little angel Léa.

1. General Introduction

Globally-averaged surface air temperature has increased by a substantial amount (0.74°C) in the last century [IPCC, 2007]. It is now well accepted that this warming is attributable to human activities (mainly fossil fuel burning) [IPCC, 2007]. As the emission of greenhouse gases is expected to increase, so too is the globally-averaged surface air temperature. Compared with other regions of the globe, the Arctic is expected to respond, and is responding, more rapidly to climate changes due to a variety of positive feedback mechanisms [IPCC, 2007; Anisimov et al., 2001], such as, for example, the ice-albedo feedback [Curry et al., 1995]. Indeed, significant changes have already been recorded in the last decades [Stroeve et al., 2007, 2008; IPCC, 2007; ACIA, 2005; SEARCH SSC, 2001; Anisimov et al., 2001; Dickson, 1999; Johannessen et al., 1999, 2004; Morison et al. 2000; Parkinson et al., 1999; Serreze et al., 2000; Vinnikov et al., 1999]. The most striking changes include the rate of increase of the average Arctic air temperature (twice the global average rate in the past 100 years [IPCC, 2007]), and the rapid decline in the summer ice extent [Stroeve et al., 2008]. Although some observed changes reflect what climate models are predicting for the future [Anisimov et al., 2001; Kattsov et al., 2005], others, such as the decrease in the extent of the perennial ice cover, are occurring more rapidly than all major climate models predict [Stroeve et al., 2007]. It is very likely that the predicted environmental changes will have a significant impact on primary production [e.g., Gradinger, 1995; Loeng et al., 2005], which drives the Arctic marine foodweb and leads to export of atmospheric carbon dioxide and its sequestering into the ocean interior. The observed and forecasted climate change in the Arctic, its potential impact on primary production, as well as the physical and biological characteristics of the Arctic Ocean, are described below.

1.1 The Arctic Ocean

1.1.1 Physical setting and oceanography

The Arctic Ocean and its bordering seas occupy an area of $14x10^6$ km^2. The Nordic Seas (Greenland, Iceland and Norwegian Seas), which are influenced by the Gulf Stream, are usually excluded from the definition of the Arctic Ocean [e.g., Carmack, 1990]. The Arctic Ocean is divided into two major basins by the Lomonosov Ridge: the Canadian Basin (~ 3800 m deep), which with its bordering seas is referred to here as the 'western Arctic', and the Eurasian Basin (~ 4200 m deep), referred to here as the 'eastern Arctic'. These two basins are further subdivided into the Canada and Makarov basins and the Nansen and Amundsen basins, respectively (Figure 1.1). These basins are surrounded by shallow shelves (< 200 m) that are typically broad (600-800 km) along the Eurasian side and narrow on the Canadian side [e.g., Carmack, 1990]. These shelves represent 50% of the Arctic Ocean area and 25% of the world shelves' area. Water from the Pacific and Atlantic Oceans flows into the Arctic Ocean (Figure 1.2) mostly through Fram Strait (~1-1.5 Sv) and the Barents Sea (~2 Sv) [Rudels and Friedrich, 2000], and from the Bering Strait (~0.8 Sv) [Roach et al., 1995]. Outflow from the Arctic Ocean to the Atlantic occurs through Fram Strait (~3-3.5 Sv) [Rudels and Friedrich, 2000] and the Canadian Archipelago (~1 Sv) [Melling, 2000]. Surface currents and ice drift in the Arctic Ocean are largely wind driven, with the most significant elements being the anticyclonic Beaufort Gyre in the Canada Basin and the Transpolar Drift (Figure 1.2). The Arctic Ocean physical settings and oceanography are discussed in more detail in Carmack [1990], Aagaard and Carmack [1994], and Macdonald et al. [2004].

Until the end of the 1990s, about 50% of the Arctic Ocean (~$7x10^6$ km^2) used to be covered with 2-3 m of multiyear ice throughout the entire year (with ice thicknesses reaching 20 m in some pressure ridges). However, in 2008, this is no longer true. The coverage of multiyear ice in the central Arctic Ocean is quickly declining, as is the summer sea ice extent which reached unprecedented low values in 2007 ($4.28x10^6$ km^2 [Stroeve et al., 2008]) and 2008 ($4.52x10^6$ km^2, Online Nature news, doi:10.1038/news.2008.1115). The surrounding marginal seas undergo a characteristic

seasonal cycle of ice formation and melt, with the minimum extent observed in September and maximum extent in late February or March [Walsh and Johnson, 1979]. First-year sea ice reaches a thickness of about 2 m. Depth of convective mixing during ice formation determines the depth of the winter mixed layer (less than ~50 m; e.g. Macdonald et al. [2004]), while melting in the summer causes a strong salinity stratification that stabilizes the water column. Winter snow accumulation averages about 40 cm on level ice but can drift up to depths of 1 m around hummocks and ridges [Barry, 1989].

The bathymetric features and the differences in the properties of inflowing water on each side of the Arctic Ocean lead to a separation of hydrographic structures between the eastern and western Arctic [McLaughlin et al., 1996]. The warm and salty (~34 psu) Atlantic layer entering the Arctic Ocean sinks beneath the colder and fresher surface water [Rudels et al., 1994]. It forms an intermediate water mass that can be found throughout the entire Arctic Ocean (Figure 1.3). A cold halocline layer is found just below the surface layer and insulates it (as well as sea ice) from the heat contained in the Atlantic layer below [e.g., Aagaard et al., 1981; Steele and Boyd, 1998]. The relatively fresh inflow of Pacific water (~30 psu), combined with freshwater runoff from large rivers in Siberia and North American rivers in Canada (Figure 1.4), lead to a surface mixed layer that is fresher and shallower on the western side of the Arctic Ocean [e.g., Steele and Boyd, 1998]. Thus, a complex halocline extends deeper on the western side (down to 200 m) dominated by the presence of Pacific origin water [e.g., McLaughlin et al., 1996; Steele et al., 2004].

The distribution and availability of nutrients are also affected by the Pacific and Atlantic water mass distribution, as well as by river runoff and the ice growth-melt cycle. Water of Pacific origin is nutrient-rich while water of Atlantic origin contains lower concentrations of nutrients, particularly silica [Rudels et al., 1991; Wheeler et al., 1996; Jones et al., 1998]. In the western Arctic, the maximum concentration of nutrients is found in the middle part of the halocline at a salinity of ~33.1 psu [e.g., Kinney et al., 1970; Coachman and Barnes, 1961], and results from inflow of Pacific waters transported

through and “transformed” over the Bering and Chukchi Seas in winter [Coachman and Barnes, 1961; Codispoti et al., 2005; Mathis et al., 2007]. The upper part and lower parts of the halocline contain fewer nutrients. The upper part is supplied with Pacific summer water, while the lower part consists of by winter Eurasian shelf water [e.g., *Jones and Anderson, 1986; Steele et al., 1995; Rudels et al., 1996; McLaughlin et al.,* 1996], and by a mixture of upwelled Atlantic layer water with shelf-bottom/upper halocline water [Codispoti et al., 2005; Woodgate et al., 2005]. The surface mixed layer has a low nutrient concentration year-round in the Arctic Ocean, except for the Chuckchi and Barents Seas. The nutrient concentration increases slightly towards the end of the winter but becomes depleted in the summer (nitrate is usually the limiting nutrient). Winter convection, which can entrain nutrients into the surface layer, is usually not sufficiently deep to increase the surface nutrient concentrations substantially [e.g., Carmack et al., 2004; Sakshaug, 2004], particularly in the western Arctic because of its stronger haline stratification (see above). Storm-driven mixing events have been observed to penetrate the upper halocline but their effect on the overall heat, salt and nutrient distributions of the Arctic Ocean mixed layer is not known [Yang et al., 2004]. The nutrient distribution and dynamics in turn influence the spatial pattern of primary production.

1.1.2 Primary production

Diatoms dominate primary production in the Arctic, both within the ice and in the water column [Horner, 1985; von Quillfeldt, 2000]. Most primary production occurs over the shelves, which are covered with first-year ice in the winter and are largely ice-free in the summer [Subba Rao and Platt, 1984; Legendre et al., 1992]. Ice algae start to grow at the end of the winter when solar radiation reappears [Cota and Smith, 1991]. As the ice starts to melt in spring, ice algae are released into the water column and a phytoplankton bloom develops, triggered by the increase in irradiance and haline stratification. However, the strong stratification leads to rapid nutrient depletion in the mixed layer [e.g., Harrison and Cota, 1991]. A progressive deepening of the phytoplankton biomass maximum, eroding the nitracline from above, is then observed over the course of the summer [e.g., Carmack

et al., 2004; Cota et al., 1996], sometimes reaching depths below the pycnocline [e.g., Rey and Loeng, 1985; Tremblay et al., 2008].

Estimates of total primary production are high for the Chukchi Sea (>200 g-C m^{-2} yr^{-1} [Walsh et al., 1989; Walsh and Dieterle, 1994]) and the Barents Sea (~110 g-C m^{-2} yr^{-1} [Sakshaug and Slagstad, 1992]). For most other shelf seas in the Arctic Ocean, total primary production ranges between 25 and 50 g-C m^{-2} yr^{-1} [Subba Rao and Platt, 1984; Legendre et al., 1992; Macdonald et al., 1987; Wallace et al., 1987; Walsh et al., 1989; also see review by Sakshaug, 2004]. The high primary production observed in the Chukchi and Barents Seas results from the nutrient-rich inflow of Pacific water through the Bering Strait [e.g., Springer, 2000; Walsh et al., 1989] and from increased vertical mixing due to cooling and mixing of the Atlantic inflow [Reigstad et al., 2002] respectively. Subba Rao and Platt [1984] estimated the central Arctic Ocean water productivity to be ~ 9 g-C m^{-2} yr^{-1}. Adding the primary production taking place in sea ice to these estimates, Legendre et al. [1992] obtained a total production for the Arctic Ocean of 0.21-0.28 Gt-C yr^{-1}. However, recent measurements suggest that the value for ice algal production in multi-year ice used by Legendre et al. [1992] may be too low [Wheeler et al., 1996; Gosselin et al., 1997]. Also, Sakshaug [2004] estimated that the total primary production would be higher than 0.33 Gt-C yr^{-1}. The Arctic Ocean represents 4% of the total oceans surface area, but its contribution to the global ocean primary production is smaller than 4% (0.33 Gt-C yr^{-1} compared with ~45 Gt-C yr^{-1} [Prentice et al., 2001]). However, the fraction of the total production that is exported below the mixed layer would be greater in the Arctic than at lower latitudes [e.g., Wassmann, 1990; Wassmann et al., 2004; Laws et al., 2000; Codispoti et al., 1991], and thus carbon export per unit area may be comparable. The Arctic Ocean's contribution to the global primary and export production could also increase as its multiyear ice cover shrinks [e.g., Stroeve et al., 2008], and as primary production at lower latitudes decreases [Behrenfeld et al., 2006; Polovina et al., 2008].

1.1.3 Export fluxes

Export production is the fraction of total primary production that is transported from the surface layer to the deep ocean, mainly through sinking of phytoplankton cells, detritus, and zooplankton faecal pellets and any net downward transport of dissolved organic matter (DOM). New production is the fraction of primary production that has its nitrogen requirement satisfied by the input of exogenous (to the mixed layer for example) nitrogen [Dugdale and Goering, 1967]. This input usually consists of an upward flux of nitrate from deeper water, plus smaller fluxes from nitrogen fixation, atmospheric deposition and rivers. In a steady-state system, any exported nitrogen must be balanced by nitrogen input. Thus, export production may be used as a measure of new production and vice-versa [see Platt et al., 1992]. Measurements and estimates of nitrate uptake by phytoplankton in the mixed layer have thus been widely used to estimate new and export production, with a property known as the *f*-ratio (new production divided by total primary production [Eppley and Peterson, 1979]). However, the use of nitrate uptake measurements as a proxy for new production has been challenged lately [Yool et al., 2007] due to recent findings that an important amount of nitrification (oxidation of ammonium) occurs in the euphotic zone and not only below it. The fraction of nitrate resulting from *in situ* recycling of ammonium thus contributes to regenerated production and not to new production. This should be kept in mind when comparing the ratio of export production to total primary production obtained with the model with published *f*-ratios, even though *in situ* nitrification appears to be less important in the Arctic [Yool et al., 2007; Codispoti et al., 1991, 2005]. Carbon export in the Arctic tends to be dominated by sinking particles [Laws et al., 2000; Moore et al., 2002]. The simulated export of carbon below the mixed layer is thus estimated from the downward flux of particulate material only, even though downward mixing and advection of DOM may occur. Labile (utilized on timescales of hours to weeks) dissolved organic carbon (DOC) export from the western Arctic shelves to halocline water of the Canada Basin has been observed but the DOC most likely originated from the shelf sediments and was transported via eddies [e.g., Davis and Benner, 2007; Mathis et al., 2007].

The ratio of export production to total or net primary production in the Arctic Ocean is higher than at low- and mid-latitudes [Wassmann, 1990; Codispoti et al., 1991], apparently due to a decoupling between phytoplankton and zooplankton, most likely due to variability in the timing of the bloom [Wassmann et al., 2004], and to lower water temperatures [Laws et al., 2000], both of which would reduce the rate of recycling of nutrients via a 'microbial loop'. The *f*-ratio in the Arctic Ocean is generally between 0.4 and 0.6, with an average value of 0.53 [Harrison et al., 1982]. Assuming these published *f*-ratios are representative of the fraction of export production relative to total production, we can apply the average *f*-ratio to the average primary production in Arctic shelf seas to obtain average organic carbon export fluxes between 10 and 25 g-C m^{-2} yr^{-1}, with higher values in the Chukchi and Barents Seas and smaller values in the central Arctic. Export fluxes in the ice-covered central Arctic are lower (0.5-1.3 g-C m^{-2} yr^{-1} [Anderson et al., 2003]) as most of the production appears to be recycled in the surface layer. Measured export fluxes are highly variable spatially and temporally [Wassmann et al., 2004], but the estimates obtained above compare relatively well with those obtained using ^{234}Th as a tracer (17-31 g-C m^{-2} yr^{-1} in shelf waters) and water chemical constituent analysis (28-32 g-C m^{-2} yr^{-1} in the Barents Sea [Fransson et al., 2001]). The estimates obtained with the *f*-ratio are also comparable with different estimates of new production (16-23 g-C m^{-2} yr^{-1} in the Beaufort Sea [Macdonald et al., 1987]). However, large uncertainties in fluxes and processes remain. There is a need to understand how fluxes of organic matter to the seafloor in the Arctic are regulated and how they will be affected by climate change, as they support some of the richest benthic communities in the world ocean [Wassmann et al., 2004 and references therein]. Changes in these benthic communities would in turn affect the distribution and reproductive success of marine mammals that feed on them [Tynan and DeMaster, 1997].

1.2 Climate Change in the Arctic and Its Potential Impacts

1.2.1 Observed and projected changes in the Arctic

Many environmental changes have already been observed in the Arctic [e.g., Dickson, 1999; Morison et al. 2000; Serreze et al., 2000], and show a trend that is (i) consistent

with greenhouse gas warming and (ii) similar to or greater than changes predicted by climate models [Anisimov et al., 2001; Kattsov et al., 2005; Stroeve et al, 2007]. There is a strong natural variability in Arctic surface air temperatures (SAT) resulting in part from variability in atmospheric patterns (e.g. the Arctic Oscillation, [Thompson and Wallace, 1998]), and in oceanic heat advection [e.g., Shimada et al., 2006]. This important variability has led some authors to question whether the observed trends were indeed anthropogenically-induced. However, recent modelling studies showed the importance of greenhouse gas forcing in reproducing observed trends [Zhang and Walsh, 2006; Stroeve et al., 2007]. Overland and Walsh [2008] suggest that the greenhouse impacts will start to emerge from this high decadal variability by the year 2020.

The average surface air temperature in the Arctic has increased approximately 0.09°C per decade since 1875 [Polyakov et al., 2003], while sea level atmospheric pressure has decreased, especially during the 1980s and 1990s [Polyakov et al., 2003; Walsh et al., 1996]. The last two decades have also seen an increase in the number of stormy days [*Yang et al.*, 2004]. Sea ice extent [Stroeve et al., 2007, 2008; Comiso and Parkinson, 2004; Johannessen et al., 1999, 2004; Parkinson et al., 1999; Vinnikov et al., 1999] and thickness [Rothrock et al., 1999] have been decreasing, although trends in ice thickness are more difficult to assess [Holloway and Sou, 2002; Johannessen et al., 2004]. The decrease in the extent of multi-year sea ice leads to a change in the composition of winter sea ice, as multi-year ice is being replaced with first-year sea ice [e.g., Kinnard et al., 2008].

Changes have also been observed in the water column in the 1990s and early 2000s. The Atlantic layer has shoaled, its temperature and horizontal distribution have increased, [Carmack et al., 1995; Morison et al., 1998; McLaughlin et al., 2002], and the front between waters of Pacific and Atlantic origin has shifted from the Lomonosov Ridge to the Alpha-Mendeleyev Ridge [McLaughlin et al., 1996; Morison et al., 1998]. These changes in the Atlantic layer result from an increased inflow of Atlantic water, via the Barents Sea and Fram Strait [Steele and Boyd, 1998; Dickson, 1999; McLaughlin et al., 2002; Karcher et al., 2007]. The cold halocline in the Eurasian Basin has also retreated

[Steele and Boyd, 1998], and the runoff of Russian rivers has been diverted eastward [Dickson, 1999; Ekwurzel et al., 2001], leading to a fresher surface layer in the western Arctic and a saltier surface layer in the eastern Arctic [Steele and Boyd, 1998]. An increase in Eurasian river runoff [Peterson et al., 2002], linked to an increase in precipitation [Serreze et al., 2000] and ice melt, has also contributed to the areally averaged thinning and freshening of the surface layer.

The changes described above reflect those predicted by climate models for the 21st century [Kattsov et al., 2005; Anisimov et al., 2001]; predicted climate change in the Arctic will be discussed in more detail in Chapter 5. Changes associated with a changing climate that can affect the Arctic marine ecosystem are those that affect nutrient levels and surface mixed layer depth, which in turn can affect primary and secondary productivity, and ultimately food availability to the upper trophic levels [Loeng et al., 2005]. In the next section, we examine the potential impacts on primary production.

1.2.2 Impact on primary production

Earlier snow and ice melt are expected to lead to a decrease in ice algal primary production [e.g., Melnikov, 2000]. While a decrease in ice and snow thickness increases the availability of light for the ice algae, it also leads to an increased loss of ice algal cells to the water column. The freshening of the surface layer may also increase nutrient limitation within the ice. On the other hand, a lengthening of the ice-free period and an increase in spatial extent of ice-free areas (decrease in multi-year ice extent) may lead to an increase in primary production by open water phytoplankton [Gradinger, 1995; Anderson and Kaltin, 2001; Loeng et al., 2005]. However, the magnitude of the increase will ultimately depend on the supply of nutrient to the mixed layer [e.g., Tynan and DeMaster, 1997; Carmack et al., 2004], which is highly dependent upon local changes in upwelling, wind-driven vertical mixing, and freshwater supply from sea ice and rivers (which enhances stratification) [Loeng et al., 2005]. In the Eurasian and Beaufort Seas, a significant increase in primary production can be expected if the ice edge retreats beyond the shelf break, thereby promoting wind-forced upwelling of nutrient-rich deep water to

the shallow shelf regions [Sakshaug, 2004; Carmack et al., 2004]. An increase in primary production could potentially increase the efficiency of the biological pump, depending on whether the export production changes or not, and if so, in what direction. Changes in the timing of phytoplankton and zooplankton production and shifts in phytoplankton species composition could both affect export production [e.g., Sakshaug, 2004; Hansen et al., 2003].

1.3 Objectives and Structure of the Thesis

Despite an increase in the number of biological observations in the Arctic since the 1990s, data appropriate for determining interactions between ice cover and primary production in the Arctic are still limited. Due to logistical constraints imposed by harsh environmental conditions, fieldwork has traditionally been conducted in spring, prior to break-up, or in summer, when ships are capable of access, resulting in large spatial and temporal gaps, especially during the time period preceding and extending through sea ice break-up. These gaps limit our understanding of the processes and their relative importance in controlling primary productivity. Numerical models provide a means to fill in the temporal and spatial sampling gaps and to evaluate the importance of specific processes. Recent programs, such as the Canadian Arctic Shelf Exchange Study (CASES, see Fortier and Cochran [2008]), and others from the International Polar Year now provide year-long data that will improve our knowledge of seasonal processes and help constrain numerical models.

Strengthening bio-physical modelling of the Arctic is essential to improving the knowledge and understanding of important processes related to climate change [Loeng et al., 2005]. Due to the high spatial variability of the processes occurring in the Arctic Ocean, a 3D model is required to obtain the spatial pattern of expected primary production changes. However, 1D models can first be used to better understand the effect of specific processes and to constrain model parameters. The overall objectives of this thesis are (1) to develop a coupled snow- sea ice – ocean – biological model, which includes ice algal production, and (2) to use that model to study the effects of climate

change on biological production and export in shelf regions of the Western Arctic. The model presented here is the first coupled model that includes ice algae and simulates the complete primary production seasonal cycle in the Arctic (Figure 1.5).

Specific objectives are:

1. to investigate the relative importance of different limiting factors (light, nutrients, ice growth rate) on ice algal growth and decline, and on biomass accumulation in the bottom 2-cm of the ice. The thesis will examine (i) the role of the molecular sublayer thickness in regulating nutrient fluxes to the sea ice skeletal layer, (ii) the relative importance of light (as controlled by the snow cover) and nutrients on ice algal growth, and (iii) the importance of the ice melt rate on biomass accumulation and on the bloom decline.
2. to estimate the annual cycle and total annual primary production on the Canadian Beaufort Sea shelf in 1987, and determine the relative importance of various physical processes (i.e. snow and sea ice thickness, sea ice melt, freshwater runoff, and water column stratification and mixing) in controlling the timing and magnitude of primary production and biogenic particle export.
3. to estimate the increase in primary production and particle export resulting from climate change over the next 100 years. Specifically, I will examine the relative importance of the increase in the period when shelf waters are free of sea ice and in freshwater runoff which can have opposite effects on mixed layer stratification and nutrient supply.

The model was developed in two stages for two different regions of the western Arctic (Beaufort Sea shelf and Canadian Archipelago) where high quality data were available. The model is described in detail in Chapter 2. As Chapters 3 to 5 represent separate studies that have been or will be published as stand-alone papers, a more concise description of each part of the model development is also presented in Chapters 3 and 4. Modelling of ice algal growth for a site near Resolute is used to address the objectives of point 1 above and is presented in Chapter 3. The development of the pelagic component of the model, its coupling with the ice algae model and its implementation for a site in the

Beaufort Sea in order to address the objectives of point 2 are described in Chapter 4. In Chapter 5, I use the coupled model to investigate the response of primary production on the Beaufort Sea shelf to climate change, using 19 years of observations, projections from the Canadian Global Climate Model (CGCM2) and a standard down-scaling technique. Finally, a concluding analysis is given in Chapter 6.

1.4 Statement of authorship

I am the first author on the three manuscripts produced by this thesis to date. I developed the overall study with feedback from my thesis committee, modified the ice model code (provided by L. Kantha) to receive the ice algal model, wrote the ice algal and NPZD model code, prepared forcing for the model, analyzed and interpreted the simulated and observed data, and wrote all drafts of the manuscripts. Dr. Ken Denman is co-author on all the papers, while Dr. Christine Michel is co-author on the first paper, and Dr. Robie Macdonald is co-author on the last two papers. All provided editorial input and advice on the interpretation of the model results. Dr. Christine Michel also provided unpublished data for the validation of the ice algal model.

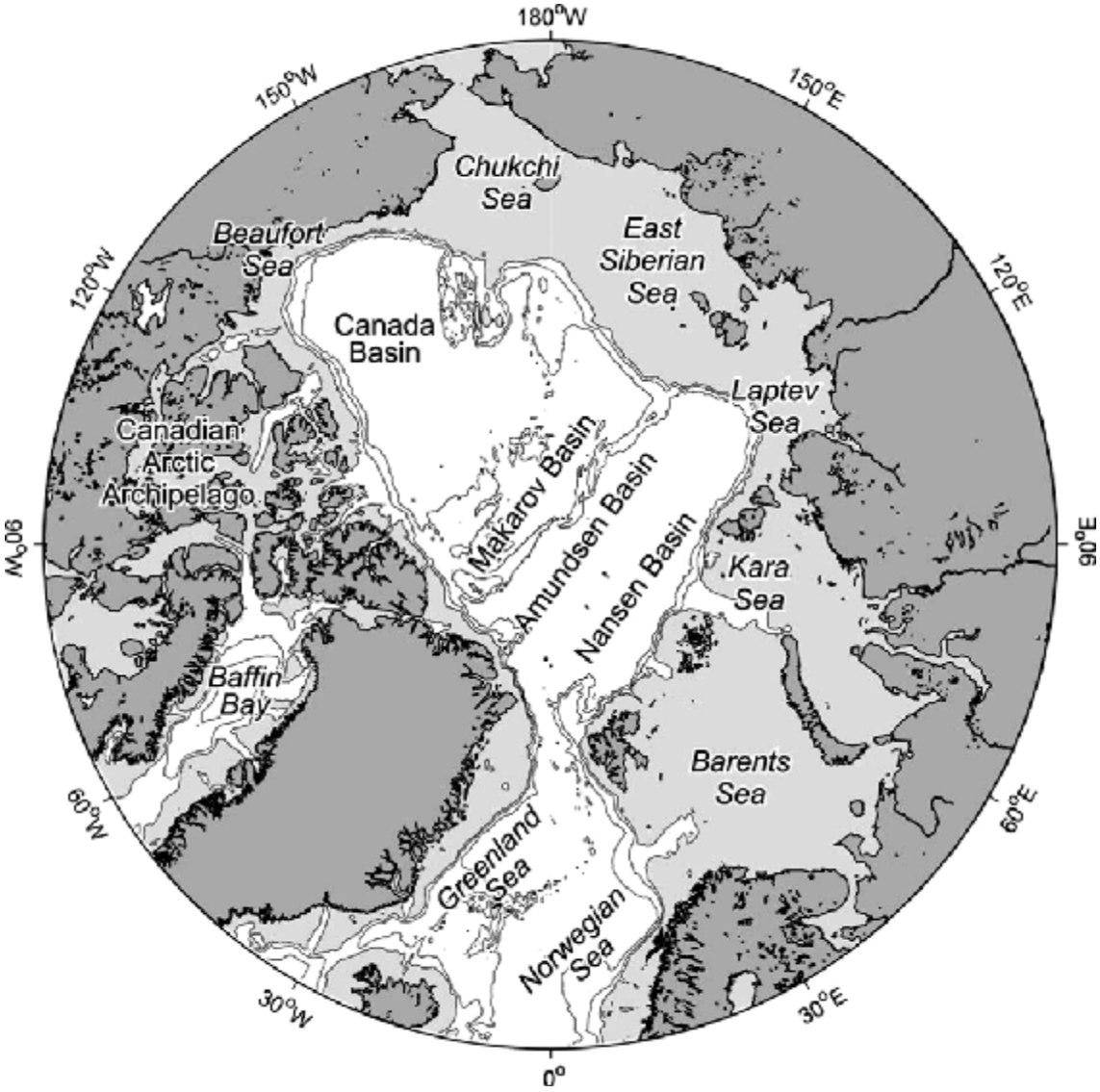

Figure 1.1 Map showing the bathymetry of the Arctic Ocean and locations of individual shelves. Isobaths are shown for 400 m and 2000 m; light grey shading denotes depths <400 m (Figure 2 from Carmack et al. [2006]).

Figure 1.2. Schematic of Arctic sea surface currents (from UNEP/GRID Arendal Maps and Graphics Library, Ocean currents and sea ice extent, http://maps.grida.no/go/graphic/ocean_currents_and_sea_ice_extent).

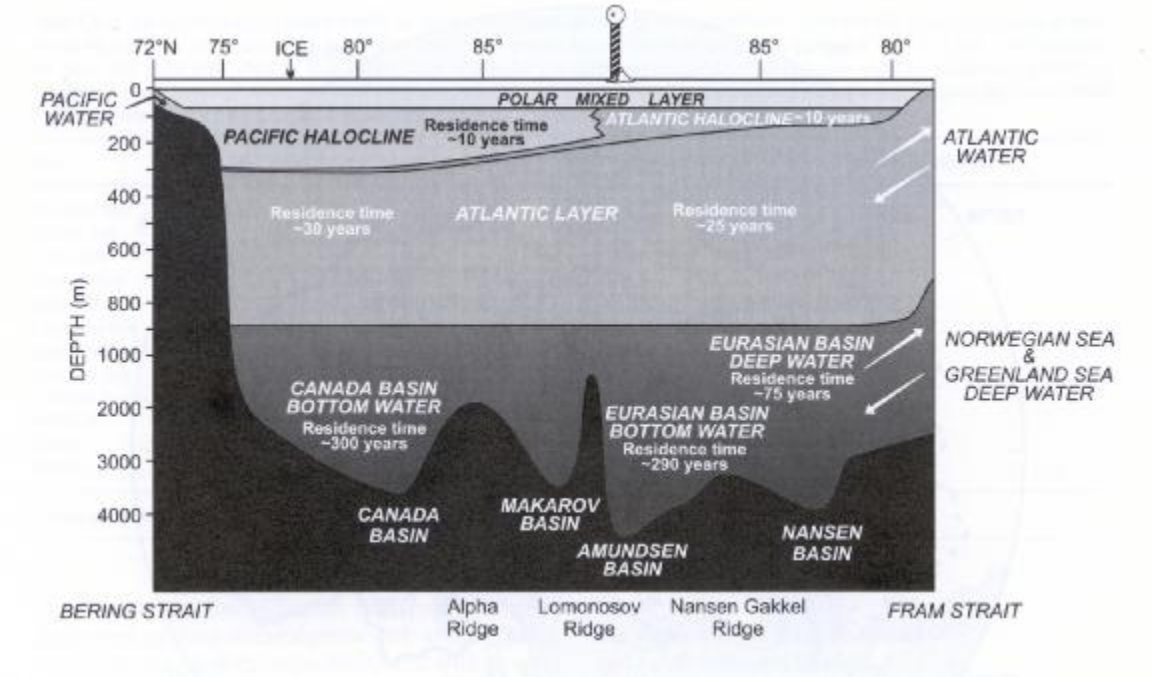

Figure 1.3. A schematic diagram showing the stratification (west to east) of the Arctic Ocean (Figure 1.2.2 from Macdonald et al. [2004]).

Figure 1.4. Map showing freshwater input to the Arctic Ocean from the main rivers (from UNEP/GRID Arendal Maps and Graphics Library, Major River Systems in the Arctic, http://maps.grida.no/go/graphic/major_river_systems_in_the_arctic). See Carmack [2000] for a more exhaustive description of freshwater inputs.

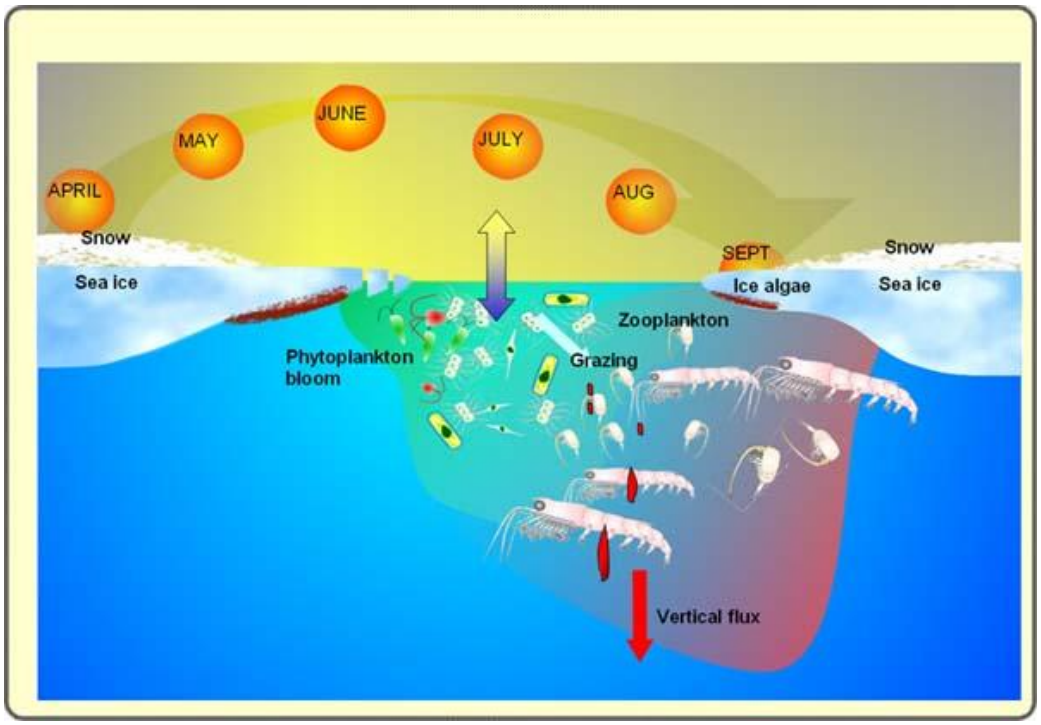

Figure 1.5. Seasonal cycle of primary production and particle export on Arctic shelves (from http://www.nfh.uit.no/arctos/background.html).

2. Model description

This chapter describes the different components of the coupled model (sea ice, ocean, ice algae, phytoplankton, zooplankton, nutrient, detritus) and how they are coupled together.

2.1 The sea ice model

The one-dimensional thermodynamic sea ice model is based on the model of Mellor and Kantha [1989], which is similar to the lowest-resolution ice model of Semtner [1976], which in turn is a simplified version of the Maykut and Untersteiner [1971] model. The model consists of one layer of snow and two layers of ice (Figure 2.1). We first constrained the thermodynamic model with observations obtained at a multi-year ice site of the Beaufort Sea during the SHEBA project (http://sheba.apl.washington.edu). Some changes have been made to the ice model of Mellor and Kantha [1989] and are described in the text (a summary of the changes can also be found at the end of Chapter 3, page 64). Variables and parameters for the sea ice model are given in Table 2.1.

2.1.1. Sea ice growth and decay

The ice growth and decay is formulated from energy balance equations at the top and bottom of the snow-ice slab, which are coupled by an equation describing the rate of heat transport between the two boundaries. The temperature within the snow or ice is governed by the one-dimensional heat equation presented by Maykut and Untersteiner [1971],

$$rc_p \frac{\partial T}{\partial t} = k \frac{\partial^2 T}{\partial z^2} + i_0 (1-a) SWke^{-kz} \qquad (2.1)$$

where ρc_p is the volumetric heat capacity, t is the time, z is the depth within the snow-ice slab, k is the thermal conductivity, i_0 is the fraction of shortwave incoming solar radiation (SW) that penetrates the upper surface (snow or ice), α is the bulk surface albedo and κ is

the attenuation coefficient. The second term on the right hand side of eq. (2.1) was added to the original equation to allow for absorption of penetrating shortwave radiation by the snow and ice (see Figure 2.1). The parameterization of a is identical to that of Flato and Brown [1996], except for the melting snow albedo which is fixed at 0.70 and the c_{12} value in eq. (2.3) which is set to 0.16 m^{-2},

$$a = \begin{cases} a_{ow} & h_i < h_{\min} \\ \min\left[a_s, a_i + h_s\left(a_s - a_i\right)/c_{10}\right] & h_i \geq h_{\min} \quad h_s \leq c_{10} \\ a_s & h_i \geq h_{\min} \quad h_s > c_{10} \end{cases} \tag{2.2}$$

$$a_i = \begin{cases} \max\left(a_{ow}, c_{11} h_i^{0.28} + 0.08\right) & T_2 < T_m \\ \min\left(a_{mi}, c_{12} h_i^2 + a_{ow}\right) & T_2 = T_m \end{cases} \tag{2.3}$$

$$a_s = \begin{cases} 0.75 & T_3 < T_m \\ 0.70 & T_3 = T_m \end{cases} \tag{2.4}$$

where T_m is the melting temperature at the ice or snow surface, T_0 is the temperature at the bottom of the ice, T_1 is the 'internal' ice temperature at its midpoint ($z = h_S + 0.5h_I$), T_2 is the temperature at the top of the ice, and T_3 is the temperature at the top of the snow.

Calculation of i_0 is based on Grenfell and Maykut [1977] values for first-year ice under cloudy and clear sky, as per the following equation:

$$i_0 = 0.40(1\text{-}c) + 0.6c \tag{2.5}$$

where c is the cloud fraction.

In the absence of melting, the net heat flux absorbed at the upper surface boundary (Q_{AI}) must balance the conductive flux at the surface (Q_s or Q_{I2}, depending on whether there is snow or not). The surface temperature (T_3 or T_2) is then determined by solving the following flux balance equation [Mellor and Kantha, 1989],

$$Q_{AI} = Q_s \text{ (or } Q_{I2}) \tag{2.6}$$

where

$$Q_{AI} = H + LE - \varepsilon LW - (1-\alpha)(1-i_0)SW + \varepsilon Bkrad \tag{2.7}$$

where H and LE are the turbulent fluxes of sensible and latent heat, ε is the longwave emissivity of ice or snow, LW is the incoming longwave radiation, SW is the global incoming shortwave radiation, and $Bkrad$ is the outgoing longwave radiation. Only the fraction of SW radiation absorbed in the first few centimeters of the snow or ice layer ($(1-i_0)SW$) contributes to the energy balance at the surface. The conductive fluxes at the surface are equal to

$$Qs = \frac{k_s}{h_s}(T_2 - T_3), \tag{2.8}$$

and

$$Q_{I2} = \frac{k_i}{h_i/2}(T_1 - T_2), \tag{2.9}$$

where k_s and k_i are the thermal conductivities of snow and sea ice, and h_s and h_i are the snow and ice thicknesses respectively.

The snow thickness is treated differently for the model development (in Resolute and in the Beaufort Sea) and for the climate change runs (Chapter 5). In the model development, a cubic spline function is fitted to the observations of snow thickness and given as input to the model. For the climate change analysis, the model is forced with a snow precipitation rate, and the snow is allowed to accumulate. When snow has melted and surface sea ice melt is occurring, the surface temperature is fixed at the melting point of

freshwater ice. The resulting imbalance between the net heat flux absorbed at the upper surface boundary (Q_{AI}) and the conductive flux at the surface (Q_{I2}) causes melting at the top of the ice according to

$$M_t = \frac{-Q_{AI} + Q_{I2}}{r_i L_i} \tag{2.10}$$

where L_i is the latent heat of fusion of sea ice and ρ_i is the density of sea ice. A similar equation applies to melting and accretion at the ice underside:

$$M_b = \frac{Q_{IO} - F_T}{r_i L_i} \tag{2.11}$$

for a total change in ice thickness of

$$\frac{\partial h_i}{\partial t} = M_t + M_b \,. \tag{2.12}$$

In eq. (2.11), Q_{IO} is the conductive flux at the bottom of the ice,

$$Q_{IO} = \frac{k_i}{h_i/2}(T_0 - T_1) \tag{2.13}$$

and F_T is the heat flux from the ocean mixed layer (see section 2.2.3.2).

2.1.2 Ice thermal properties

The initial thermodynamic model had uniform ice thermal properties but here I develop expressions for the thermal properties of sea ice for both layers of the model (Figure 2.1), from the mean temperature (T_{ice}) and salinity (S_{ice}) of each layer (ice depth 0-h*i*/2, and h*i*/2-h*i*). The bulk salinity of the ice is assumed constant at 5 psu. As the ice temperature

changes, internal melting or freezing within the brine pockets affect the brine volume of the ice. According to Maykut [1985], the amount of freshwater ice present in a unit mass of sea ice is (1-0.01v_b), so that the latent heat of fusion, L_i, can be calculated as follow:

$$L_i = (1\text{-}0.01v_b)L_{fw}, \tag{2.14}$$

where L_{fw} is the latent heat of fusion of freshwater ice and v_b is the volume fraction of brine in the ice, calculated after Frankenstein and Garner [1967]:

$$n_b = 0.01S_{ice}(0.0532 - \frac{4.919}{T_{ice}}), \quad -22.9 \le T_{ice} \le -0.5°C \tag{2.15}$$

Brine pockets also affect the transport of heat in sea ice. This effect is accounted for in the representation of the thermal conductivity (k_i) and volumetric heat capacity $(\rho c_p)_i$ of sea ice as functions of temperature and salinity. Both k_i and $(\rho c_p)_i$ are calculated as in Flato and Brown [1996]:

$$k_i = \max\left[k_0 + \frac{bS_{ice}}{T_{ice}}, \frac{k_0}{5}\right] \tag{2.16}$$

where k_o is the thermal conductivity of pure ice, and b is a constant equal to 0.1172 W m^{-1} ppt^{-1}, and

$$(rc_p)_i = \min\left[(rc_p)_0 + \frac{gS_{ice}}{T_{ice}^{\ 2}}, 100(rc_p)_0\right] \tag{2.17}$$

where $(rc_p)_0$ is the volumetric heat capacity of pure ice and g is a constant equal to 1.715x10^7 J K m^{-3} ppt^{-1}. The thermal conductivity of snow (k_s) is calculated as in Ebert and Curry [1993],

$$k_s = 2.845x10^{-6}\, r_s^2 + 2.7x10^{-4} \cdot 2^{(T_s-233)/5} \qquad (2.18)$$

2.1.3 Atmospheric bulk formulas

2.1.3.1 Shortwave radiation

The global solar radiation (wavelengths ≤ 4000 nm) is calculated after Parkinson and Washington [1989]:

$$SW = \frac{S\cos^2 q_z (1-0.6c^3)}{(\cos q_z + 2.7)\cdot e \cdot 10^{-5} + 1.085\cos q_z + 0.10} \qquad (2.19)$$

where S is the solar constant (1353 W m^{-2}), c is the cloud cover fraction (varying from 0 to 1), e is the atmospheric vapour pressure, and q_z is the solar zenith angle. The cosine of the zenith angle is given by

$$\cos q_z = \sin f \sin d + \cos f \cos d \cos y, \qquad (2.20)$$

where f is the latitude, d is the solar declination, and y the hour angle:

$$d = 23.44° \cos [360°(172\text{-day of year})/365] \qquad (2.21)$$

$$y = 15° (12 - \text{solar time}) \qquad (2.22)$$

2.1.3.2 Longwave radiation

The incoming longwave radiation (wavelengths > 4000 nm) is calculated after Maykut and Church [1973]

$$LW = s\, T_a^4\, (0.7855 + 0.2232c^{2.75}) \qquad (2.23)$$

where T_a is the air temperature and s is the Stefan-Boltzmann constant. The outgoing

longwave radiation is calculated according to the Stefan-Boltzmann law,

$$Bkrad = -s\ T_{sfc}^{4} \tag{2.24}$$

where T_{sfc} is the surface temperature.

2.1.3.3 Turbulent fluxes

The turbulent fluxes of sensible and latent heat are calculated after Andreas [1987], which takes into account the effect of the boundary layer stability in the calculation of the sensible and latent heat transfer coefficients (C_H and C_E). The sensible heat is equal to

$$H = r_a c_{pa} C_H V_{wg} (T_{sfc} - T_a) \tag{2.25}$$

where r_a is the air density, c_{pa} is the specific heat of air and V_{wg} is the wind speed at 10 m. The latent heat flux is equal to:

$$LE = r_a L_s C_E V_{wg} (q_{sfc} - q_{10m}) \tag{2.26}$$

where L_s is the latent heat of sublimation and q_{sfc} and $q_{10\mathrm{m}}$ are specific humidities at the surface and at 10 m:

$$q_{sfc} = \frac{e_a e_s}{p - (1 - e_a) e_s} \tag{2.27}$$

and

$$q_{10m} = RH/100 * q_{sfc} \tag{2.28}$$

where e_a (0.622) is the ratio of the molecular weight of water vapour to that of dry air, e_s is the saturation vapour pressure, derived from an empirical formula by Murray [1967]

$$e_s = 611x10^{a(T_{sfc} - 273.16)/(T_{sfc} - b)} \tag{2.29}$$

where (a, b)=(9.5, 7.66), and RH (in %) is the relative humidity.

2.1.4 PAR attenuation coefficients

As in Zeebe et al. [1996], it is assumed that the fraction of shortwave radiation (SW) that penetrates the ice-snow surface (i_0, eq. 2.5) belongs to the visible band (PAR) only. PAR at the surface (PAR_0) is thus equal to

$$PAR_0 = i_0(1-\alpha)SW^1 \quad (2.30)$$

The distribution of PAR within the ice or snow is assumed to follow Beer's law [Maykut, 1985],

$$PAR(z) = PAR_0 e^{-kz\,1} \quad (2.31)$$

where z is the depth below the snow or ice surface and κ is the snow or ice attenuation coefficient. Attenuation coefficients are lower for the visible band wavelengths than at other wavelengths of the solar spectrum [e.g., Grenfell and Maykut, 1977]. Based on previous studies [Grenfell and Maykut, 1977; Smith et al., 1988; Ebert et al. 1995] as well as on light measurements made in Resolute (see Chapter 3), we chose the following PAR attenuation coefficients (in m^{-1}): 1.2 for the ice, 14 for dry snow and 7.5 for melting snow. The snow PAR attenuation coefficients are within the range of values used by Ebert et al. [1995] for their 250-690 nm irradiance band (which can be reduced since their values include ultra-violet radiation) and those of Smith et al. [1988] for the 400-700 nm band (i.e. PAR).

---

[1] Equations 2.30 and 2.31 provide an adequate approximation of the downwelling PAR near the bottom of 'thick' ice where the ice algae are assumed to live in this model, but they would give a significant error if one is interested in the downwelling PAR near the surface of the ice. To be optically correct, equation 2.30 should be formulated in terms of the specular reflection at the surface $\Re_0$ according to the following equation adapted from Grenfell (1979): $a_l PAR_0 = \Re_0 PAR_0 + (1-\Re_0) PAR_0^{\uparrow}$.

The ice algae growing in the ice also attenuate PAR. The attenuation coefficient for ice algae (κ_{chl}) is defined as [e.g., Kirk, 1983]

$$\kappa_{chl} = a^*[chl\ a] \qquad (2.32)$$

where a^* is the mean chl *a*-specific attenuation coefficient (0.02 m^2 (mg-chl *a*)$^{-1}$) and [*chl a*] is the concentration of chl *a* (mg-chl *a* m^{-3}) at the bottom of the ice.

2.2 The ocean model

The ice algae model was first constrained with data collected in the Resolute area. As this region is very dynamic, the mixed layer cannot be modelled with a 1D model alone. Observations were used to calculate the ice-ocean fluxes. In the fully coupled model, implemented in the Beaufort Sea, the different oceanic properties are calculated with the 1D model.

2.2.1 Turbulent mixing coefficients

In Resolute, the mean (time-varying) eddy diffusion coefficient (K_H) varies with the neap-spring tidal cycle, the phase of which was determined from tidal predictions made by the Canadian Hydrographic Service. Average eddy diffusion coefficients for neap (5×10^{-4} $m^2\ s^{-1}$) and spring (1.5×10^{-3} $m^2\ s^{-1}$) tides were determined from an Acoustic Doppler Current Profiler deployed in the study area in May 2002 (R. Marsden, Royal Military College of Canada, unpublished data, 2002). These values are similar to those obtained by Shirasawa and Ingram [1997]. The eddy diffusion coefficient is assumed to be equal to the eddy viscosity coefficient (K_M) [see Crawford et al., 1999 and references therein].

In the fully-coupled model (Beaufort Sea), we represent the upper ocean with the turbulence closure (level 2.5 version) model of Mellor and Yamada [1974, 1982]. The model domain is 120 m deep, with 22 layers of variable thickness. The turbulent mixing coefficients (K_M and K_H) are calculated at all depths each time step. Tidal currents on the

Mackenzie shelf are generally weak and are neglected in the model equations since they do not represent a major source of mixing energy [Kulikov et al., 2004; Carmack and Macdonald, 2002]. Winds provide mixing energy during ice-free periods and the movement of the sea-ice cover on the ocean provides mixing energy in winter.

2.2.2 Temperature and salinity

For Resolute, the model was forced with surface temperature and salinity derived from observations. In the coupled model, the water temperature at depth *z* changes according to

$$\frac{\partial T}{\partial t} = \frac{\partial}{\partial z}\left[\left(K_H + b\right)\frac{\partial T}{\partial z}\right] + \frac{1}{\left(rc_p\right)_w}\frac{\partial PAR}{\partial z} \qquad (2.33)$$

where t is the time, z is the depth within the mixed layer, β is a background diffusion ($1\text{x}10^{-5}$ m^2 s^{-1}), $(\rho c_p)_w$ is the volumetric heat capacity of water and *PAR* is the visible radiation that penetrates the surface of the ocean (calculated as in eq. 2.31). The second term on the right hand side of eq. (2.33) accounts for warming resulting from the absorption of shortwave radiation in the ocean. When ice cover is present, *PAR* is a function of cloudiness, snow and ice type and thickness (see section 2.1); when the ocean is ice free, *PAR* immediately below the surface microlayer of the ocean is equal to $0.45(1-\alpha_w)SW$ (α_w is the water albedo and *SW* is the total short wave solar radiation). *PAR* is attenuated throughout the water column by the water itself and by both phytoplankton and detritus for a total attenuation coefficient (κ_t) of:

$$\kappa_t = \kappa_w + a_p Phy + a_d(Ds+Df+Dia) \qquad (2.34)$$

where κ_w is the attenuation coefficient of pure seawater (0.045 m^{-1}), a_p and a_d (both 0.03 m^2 $(mmol\text{-}N)^{-1}$) are the specific attenuation coefficient for phytoplankton and detritus respectively, *Phy* is the phytoplankton biomass, and D_s, D_f and D_{ia} are the concentration of slow-sinking, fast-sinking and ice algal detritus.

The salinity in the water column changes according to

$$\frac{\partial S}{\partial t} = \frac{\partial}{\partial z}\left[(K_H + b)\frac{\partial S}{\partial z} \right] \qquad (2.35)$$

The domain of the Beaufort Sea model extends well into the halocline at the bottom of the polar mixed layer (~50 m). A parameterization of this halocline and of the water mass below was therefore prescribed by relaxing the temperature and salinity over the bottom 70 m to the initial profile with a relaxation timescale of 3 days.

2.2.3 Ocean/sea ice interfacial fluxes

The ocean and sea ice are coupled through the exchange of heat and salinity through a thin control volume [see Mellor et al., 1986 and Figure 2.2]. The turbulent fluxes of heat and salt are assumed proportional to the gradients of temperature and salinity respectively.

2.2.3.1 Interfacial stress

In the coupled model (Beaufort Sea), the ice-ocean interfacial stress is a function of the velocity difference between the ice and the ocean (U_I-U, V_I-V) and the roughness length (z_0). The boundary condition for stress is

$$K_M\left(\frac{\partial U}{\partial z}, \frac{\partial V}{\partial z} \right) = \frac{\left(t_{IOx}, t_{IOy} \right)}{r_w} \qquad z \rightarrow 0 \qquad (2.36)$$

where (t_{IOx}, t_{IOy}) is the ice-ocean interfacial stress given by

$$\frac{\left(t_{IOx}, t_{IOy} \right)}{r_w} = \frac{k u_t}{\ln(z / z_0)} \left(U_I - U, V_I - V \right) \qquad z \rightarrow 0 \qquad (2.37)$$

where u_τ is the friction velocity. The ice velocity ($\sqrt{U_I^2 + V_I^2}$) is constant in the model (0.24 m s^{-1}).

2.2.3.2 Heat flux

The heat flux boundary condition at the ocean/sea ice interface is

$$\frac{F_T}{r_w c_{pw}} = -C_{HT} u_t \left(T_0 - T\right) \tag{2.38}$$

where F_T is the oceanic heat flux, ρ_w, c_{pw} and T are the mixed layer density, specific heat and temperature respectively, T_0 is the interfacial temperature and C_{HT} is the heat transfer coefficient [Mellor and Kantha, 1989]. The latter is equal to

$$C_{HT} = \frac{1}{P_{rt} k^{-1} \ln\left(-z/z_0\right) + B_T} \tag{2.39}$$

where P_{rt} is the turbulent Prandtl number (0.87), k is the von Karman's constant (0.4), z is the depth, within the mixed layer, from the ice ocean interface, z_0 is the roughness length and B_T is equal to

$$B_T = b\left(\frac{z_0 u_t}{n}\right)^{1/2}\left(\mathrm{Pr}^{2/3} - 0.2\right) + 2.3 \tag{2.40}$$

where v is the kinematic viscosity of seawater (1.85×10^{-6} m^2 s^{-1}), Pr is the molecular Prandtl number (14.2) and b is a constant equal to 1.2. The first and second terms in the denominator of eq. (2.39) represent the temperature changes across the turbulent and molecular portions of the interface layer respectively. We determine z_0 as $0.07h_i$ m, where h_i is the ice thickness.

2.2.3.3 Salt flux

The salt balance across the ocean interface is equal to

$$F_S = (W_O - W_{RO})(S_I - S_0) + S_0 R \tag{2.41}$$

where W_O represents the vertical speed of the ice/ocean interface due to accretion and ablation at the base of the ice (proportional to M_b, eq. 2.11), W_{RO} is the "percolation" speed of the surface melt water which migrates through the ice/ocean interface (equal to the melt rate at the snow/ice-atmosphere interface), S_I and S_0 are the ice and interface salinities. The last term in eq. (2.41) was added to account for the influence of freshwater inflow due to lateral advective processes, following Holland et al. [1997]. We calculated a variable value for R that follows the Mackenzie River's freshwater runoff curve for 1987 [e.g., see Carmack et al., 2004], but with a lag of one month to account for travel time between the hydrology observation site (Red River) and our modelling site [O'Brien et al., 2006], and with annual average and maximum values for R of 0.067 and 0.17 g m^{-2} s^{-1} respectively (Figure 2.3).

The salt flux boundary condition at the interface is

$$F_S = -C_S u_t \left(S_0 - S\right) \tag{2.42}$$

$$C_S = \frac{1}{P_{rt} k^{-1} \ln\left(-z/z_0\right) + B_S} \tag{2.43}$$

$$B_S = b\left(\frac{z_0 u_t}{n}\right)^{1/2}\left(Sc^{2/3} - 0.2\right) + 2.3 \tag{2.44}$$

where eq. (2.41) must equal eq (2.42). The above equations are identical to equations (2.39) and (2.40) for heat transfer except that the Prandtl number (Pr) in (2.40) is replaced by the Schmidt number (Sc = 2432) for salt diffusion.

2.2.4 Coupling between the atmosphere and the ocean

2.2.4.1 Interfacial stress

When the ocean is free of ice, mixing energy is provided to the mixed layer by the wind

stress ($\vec{t}$),

$$\vec{t} = C_D r_a \vec{V}_{wg} \left| V_{wg} \right| \qquad (2.45)$$

where ρ_a is the surface atmospheric density and C_D, the drag coefficient, varies with the wind speed (V_{wg}) according to Large and Pond [1981]

$$10^3 C_D = \begin{cases} 1.14 & V_{wg} < 10 \text{ m s}^{-1} \\ 0.49 + 0.065 V_{wg} & 10 \le V_{wg} \le 25 \text{ m s}^{-1} \\ 2.1 & V_{wg} > 25 \text{ m s}^{-1} \end{cases} \qquad (2.46)$$

2.2.4.2 Heat flux

The turbulent fluxes of sensible and latent heat for an ice-free ocean are similar to those in equations (2.25) and (2.26) except that C_E and C_H are constant (1.2×10^{-3} and 1.0×10^{-3} respectively, from Smith [1988]).

2.2.4.3 Surface salinity flux

The salt flux (F_S) into the ice-free ocean differs from Mellor and Kantha [1989]. As in Omstedt et al. [1994], we neglect the evaporation/precipitation term and, as for ice covered conditions, add the effect of freshwater inflow due to lateral advective processes (R). The salt flux is thus equal to

$$F_S = S_0 R \qquad (2.47).$$

2.3 The biological model

The biological model consists of nine compartments (state variables) shown schematically in Figure 3: dissolved inorganic nitrogen (*N*), silicate (*Si*), phosphate (*P*), ice algae (*Ia*), phytoplankton (*Phy*), zooplankton (*Z*), fast-sinking detritus (D_f), slow-sinking detritus (D_s) and ice algal detritus (D_{ia}). The basic unit in the model is mmol-N m^{-3}. Conversion to carbon (C), chlorophyll *a* (chl *a*), Si and P are needed for

comparison with observations. We assume fixed Redfield ratios [Redfield et al., 1963] for conversion between C, N and P (C:N:P = 106:16:1). For conversion of N to chl *a*, we use N:chl *a* (wt:wt) of 8.75:1 (calculated from the C:chl *a* given below) for phytoplankton and 5:1 for ice algae [Cota et al., 1987]. Ice algae grow at low light conditions and thus produce more chl *a* for light harvesting, explaining the lower N:chl *a* ratio for ice algae. The N:chl *a* ratios correspond to C:chl *a* (wt:wt) ratios of 50:1 for phytoplankton [e.g., Sakshaug and Slagstad, 1991; Wheeler et al., 1996] and 28:1 for ice algae. The Si:N (mol:mol), taken as 1.7 from measurements of N:Chl *a* ratio of 5 [Cota et al., 1987] and Si:Chl *a* ratio of 17 (see Chapter 3) in the Canadian Archipelago, is the same for ice algae and phytoplankton.

Physical and biogeochemical processes control the total rate of change of the concentration of the different constituents present in the mixed layer,

$$\frac{\partial A}{\partial t} = \left.\frac{\partial A}{\partial t}\right|_{phys} + \left.\frac{\partial A}{\partial t}\right|_{bio} \qquad (2.48)$$

where A represents any of the compartments, except for ice algae. A is mixed as for salinity in eq. (2.35), while the parameterization of the biological processes is presented below.

2.3.1 Ice algae

The ice algal growth model is described in detail in Chapter 3. Ice algae use nutrients from the upper mixed layer. Ice algae are assumed to be limited by silicic acid; the other macro-nutrients are taken up by the ice algae according to the Redfield ratio (N:Si:P 16:27.2:1), based on the ratios described above. When melting occurs at the bottom of the ice, ice algal cells are expelled from the ice into the mixed layer at a rate proportional to the ice melt rate. In the model, a fraction of these cells can contribute to phytoplankton seeding but for the control run, all the cells are converted into detritus (D_{ia}).

2.3.2 Phytoplankton

Phytoplankton in the water column are modelled as diatoms, which dominate the plankton community on the Beaufort Sea shelf [Parsons et al., 1988; Hsiao et al., 1977]. The rate of change in phytoplankton biomass is calculated as

$$\frac{\partial Phy}{\partial t} = Phy\left[m - M_{Phy} - S_{Phy}\right] + (1 - fad)Ia - G_{Phy}Z \qquad (2.49)$$

where μ is the specific phytoplankton growth rate, M_{Phy} is the specific mortality rate of phytoplankton, G_{Phy} is the specific loss rate of phytoplankton due to grazing, and S_{Phy} is a function representing loss of diatoms through sedimentation of resting spores and aggregates. This function, S_{Phy}, is related to nutrient depletion and is described in Wassmann and Slagstad [1993],

$$S_{Phy} = (d_{mn} + (d_{mx} - d_{mn}))e^{-\min(N_{coag}N, Si_{coag}Si)} \qquad (2.50)$$

where d_{mn}, d_{mx}, N_{coag}, $Si_{coag,}$ are parameters given in Table 2.2. The phytoplankton losses due to mortality and sedimentation are converted to slow- and fast-sinking detritus respectively [Slagstad et al., 1999]. The second term on the right-hand side of eq. (2.49) represents seeding of phytoplankton by ice algal cells sloughed into the water column where *fad* is the fraction of sloughed ice algal cells that is converted directly to detritus.

Phytoplankton growth depends on light, nutrients and temperature. Assuming that the phytoplankton growth is limited by one factor at a time, the specific phytoplankton growth rate is

$$m = m_{\max} \min\left[\frac{N_i}{Ks_i + N_i}, (1 - \exp\left(\frac{-a^B PAR}{P_m^B}\right)\exp\left(\frac{bPAR}{P_m^B}\right)\right] \qquad (2.51)$$

The first term in brackets accounts for nutrient limitation represented by the Michaelis-Menten (monod) function, while the second term accounts for limitation by light

represented by the exponential function of Platt et al. [1980]. $m_{\max}$ is the maximum temperature-dependent phytoplankton growth rate, N_i (i = 1, 2, or 3) is the concentration of the three nutrients: nitrogen, silicic acid and phosphate, Ks_i (i = 1, 2, or 3) is the half-saturation constant for each nutrient, a^B is the photosynthetic efficiency, P^B_m is the maximum (light-saturated) photosynthetic rate of diatoms, and β is a photoinhibition coefficient. All functions return a value between 0 and 1 and the most limiting factor (lowest value) is used to calculate the specific growth rate. Growth occurs only for *PAR* greater than the compensation intensity, fixed at 0.3 W m^{-2} after Subba Rao and Platt [1984]. The maximum (non-limited) specific phytoplankton growth rate $m_{\max}$ is predicted from the relationship of Eppley [1972]

$$m_{\max} = 0.69 m_0 \exp(r_u T) \qquad (2.52)$$

where m_0 is the specific growth rate at 0°C, r_u is a rate constant that determines the sensitivity of $m_{\max}$ to changes in temperature, and T is the water temperature.

2.3.3 Nutrient concentration

The rate of change of nutrient concentration in the mixed layer is equal to

$$\frac{\partial N_i}{\partial t} = g_{Ds} D_s + g_{Df} (D_f + D_{ia}) + E_{zn} Z - mPhy \qquad (2.53)$$

where γ is the remineralization rate of detritus to nitrogen and phosphate, or the dissolution rate in the case of Si (N_2), and E_{zn} is the excretion rate of zooplankton. The slow- and fast-sinking detritus remineralize to N and P at different rates, but dissolve to Si at the same rate (see section 2.3.5). The term $E_{zn}Z$ does not appear in the calculation of Si concentration. The last term on the right-hand side of eq. (2.53) represents the uptake rate of nutrient by phytoplankton. Nutrients are restored to their initial value in the halocline (at 60 m) and over the bottom 3 levels with a timescale of 3 days. The model results are

not sensitive to the restoring time scale since these layers are effectively decoupled from the surface mixed layer.

2.3.4 Zooplankton

Zooplankton are modelled as large copepods (>2 mm), which dominate the zooplankton community in the modelling site area [Parsons et al., 1988, 1989; Forbes et al., 1992]. The rate of change in zooplankton biomass is calculated as follows,

$$\frac{\partial Z}{\partial t} = Z\left[g_a G - E_{zn} - M_z\right] \tag{2.54}$$

where g_a is the assimilation efficiency, G is the specific grazing rate on phytoplankton and detritus, and M_z is the zooplankton mortality rate. Grazing is represented by a standard quadratic dependence on prey (Holling-type-III) [Denman and Peña, 1999]

$$G = r_m \frac{food^2}{K_p^{\,2} + food^2} = G_{Phy} + G_{Df} + G_{Dia} \tag{2.55}$$

where r_m is the maximum grazing rate, and K_p is the half-saturation constant for grazing. Grazing on phytoplankton, detritus and ice algae is partitioned as follows:

$$food = Phy + fd_1 D_f + fd_2 D_{ia} \tag{2.56}$$

where fd_i can be considered as either the fraction of detritus/ice algae used as food or the preference for detritus/ice algae relative to a preference of 1 for phytoplankton.

2.3.5 Detritus

Detritus is divided into three compartments: slow-sinking (D_s), fast-sinking (D_f) and ice algae (D_{ia}). The slow-sinking component is made up of dead phytoplankton cells while the fast-sinking component encompasses faecal pellets, dead zooplankton bodies and

sedimenting phytoplankton cells. The fraction of ice algal cells expelled from the ice during ice melt that is not used for phytoplankton seeding (*fad*) goes to ice algal detritus. The fast-sinking and ice algal particles have a sinking rate (w_f) of 50 m d^{-1} and a degradation rate (γ_{Df}) of 0.33 d^{-1}, while the slow-sinking component has a sinking rate (w_s) of 1 m d^{-1} and a degradation rate (γ_{Ds}) of 0.05 d^{-1}. These rates were taken from Slagstad et al., [1999]. The dissolution rate of detrital Si is the same for the three compartments (0.03 d^{-1}). The concentration of slow-sinking, fast-sinking and ice algal detritus changes according to equations (2.57) to (2.59) respectively:

$$\frac{\partial D_s}{\partial t} = M_{Phy} Phy - g_{Ds} D_s - w_s \frac{\partial D_s}{\partial z} \qquad (2.57)$$

The first term on the right hand side of eq. (2.57) is the supply of detritus due to mortality of phytoplankton, the second term is remineralization of detritus to nutrient, and the last term represents sinking of detritus.

$$\frac{\partial D_f}{\partial t} = S_{Phy} Phy + (1 - ga) GZ + M_Z Z - g_{Df} D_f - G_{Df} Z - w_f \frac{\partial D_f}{\partial z} \qquad (2.58)$$

The first term on the right-hand side of eq. (2.58) is the supply of detritus from sedimenting phytoplankton cells, the second term is fecal pellet production by copepods, the third term is mortality of copepods, the fourth term is remineralization of fast-sinking detritus to nutrient, the fifth term is grazing of fast-sinking detritus by copepods, and the last term represents sinking of detritus. The terms relating to zooplankton are removed from eq. (2.58) in the calculation of the Si detritus concentration and (1-*ga*)*GZ* is replaced with $G_{Phy}Z$ since fecal pellet production of silicate is equal to grazing on diatoms (silicate is passed directly from phytoplankton to the Si detritus pool through zooplankton [Chai et al., 2002]).

$$\frac{\partial D_{ia}}{\partial t} = fadIa - g_{Df} D_{ia} - G_{Dia} Z - w_f \frac{\partial D_{ia}}{\partial z} \qquad (2.59)$$

The first term on the right-hand side of eq. (2.59) is the supply of detritus from the ice algae, while the third term is grazing by copepods. The term relating to zooplankton is removed from the equation in the calculation of the Si detritus concentration.

Table 2.1. Values and units for variables and parameters used and calculated by the physical model. The observations given as input to the model are described in Chapters 3 to 5.

Variable	Definition	Estimated value	Unit
α	Bulk surface albedo	calculated	dimensionless
α_i	Ice albedo	calculated	dimensionless
α_{mi}	Melting ice albedo	0.55	dimensionless
α_{ow}	Open water albedo	0.15	dimensionless
α_s	Snow albedo	see eq. (2.4)	dimensionless
c	Cloud cover fraction	input	dimensionless
c_{10}	Parameter in eq. (2.2)	0.1	m
c_{11}	Parameter in eq. (2.3)	0.44	$m^{-0.28}$
c_{12}	Parameter in eq. (2.3)	0.16	m^{-2}
C_{HT}	Heat exchange coefficient, ice-ocean	calculated	dimensionless
c_{pi}	Specific heat of sea ice	calculated	J kg^{-1} K^{-1}
c_{p0}	Specific heat of pure ice	2093	J kg^{-1} K^{-1}
c_{pw}	Specific heat of water	3990	J kg^{-1} K^{-1}
ε_i	Emissivity of ice surface	0.97	dimensionless
ε_s	Emissivity of snow surface	0.99	dimensionless
F_T	Oceanic heat flux	calculated	W m^{-2}
h_i	Ice thickness	calculated	m
h_v	Molecular sublayer thickness	calculated	m
h_{min}	Minimum ice thickness below which open water is assumed	0.001	m
h_s	Snow thickness	input	m
H	Sensible heat	calculated	W m^{-2}
k_i	Thermal conductivity of sea ice	calculated	J m^{-1} s^{-1} K^{-1}
k_0	Thermal conductivity of pure ice	2.04	J m^{-1} s^{-1} K^{-1}
k_s	Thermal conductivity of snow	calculated	J m^{-1} s^{-1} K^{-1}
K	Turbulent mixing coefficient	estimated	m^2 s^{-1}
κ_i	Ice attenuation coefficient	1.3	m^{-1}
κ_s	Snow attenuation coefficient	8 or 14.5	m^{-1}
κ_{chl}	Ice algal attenuation coefficient	calculated	m^{-1}
L_{fw}	Latent heat of fusion of freshwater ice	3.335×10^5	J kg^{-1}
L_i	Latent heat of fusion of sea ice	calculated	J kg^{-1}
L_s	Latent heat of sublimation	2.834×10^6	J kg^{-1}
LE	Latent heat flux	calculated	W m^{-2}
LW	Incoming longwave radiation	calculated	W m^{-2}
v	Kinematic viscosity of seawater	1.85x10-6	m^2 s^{-1}
Q_{AI}	Heat flux at the ice-atmosphere interface	calculated	W m^{-2}
Q_{IO}	Conductive flux at the ice-ocean interface	calculated	W m^{-2}
Q_{I2}	Conductive flux at the ice-atmosphere interface, or snow-ice interface	calculated	W m^{-2}
Q_S	*Conductive* flux at the snow-atmosphere interface	calculated	W m^{-2}
ρ_i	Reference ice density	917	Kg m^{-3}
ρ_s	Reference snow density	330 or 450	Kg m^{-3}
ρ_w	Mixed layer density	input	Kg m^{-3}
S_{ml}	Mixed layer salinity	input	
SW	Shortwave radiation	calculated	W m^{-2}
T_a	Air temperature	input	°C
T_f	Freezing temperature of seawater	calculated	°C
T_{ml}	Mixed layer temperature	input	°C
u_τ	Friction velocity	estimated	m s^{-1}

Table 2.2. Values and units for variables and parameters used and calculated by the biological model.

Variable	Definition	Estimated value	Unit
a_d	Specific attenuation coefficient for detritus	0.03	m^2 (mmol-N)$^{-1}$
a_P	Specific attenuation coefficient for phytoplankton	0.03[1]	m^2 (mmol-N)$^{-1}$
α^B	Photosynthetic efficiency	0.08[2,3]	mg-C (mg-chl *a*)$^{-1}$ h^{-1} (W m^{-2})$^{-1}$
B	Photoinhibition	0.002[4]	mg-C (mg-chl *a*)$^{-1}$ h^{-1} (W m^{-2})$^{-1}$
d_{mn}	Parameter (eq. 2.50)	0.004[5]	h^{-1}
d_{mx}	Parameter (eq. 2.50)	0.02[5]	h^{-1}
E_{zn}	Zooplankton excretion rate	0.03	d^{-1}
g_a	Assimilation efficiency of zooplankton	0.7	dimensionless
G_D	Grazing rate on detritus	calculated	d^{-1}
G_{Phy}	Grazing rate on phytoplankton	calculated	d^{-1}
Fad	Fraction of sloughed ice algae that goes to detritus	0.9	dimensionless
fd_1	Fraction of fast-sinking detritus used as food	0.5	dimensionless
fd_2	Fraction of ice algal detritus used as food	0.8	dimensionless
γ_{Ds}	Remineralization rate of slow-sinking detritus	0.05[6]	d^{-1}
γ_{Df}	Remineralization rate of fast-sinking detritus	0.33[6]	d^{-1}
γ_{Si}	Remin rate for Si (detritus)	0.03[7]	d^{-1}
κ_w	Attenuation coefficient of pure sea water	0.05[6]	m^{-1}
κ_p	Attenuation coefficient of phytoplankton	calculated	m^{-1}
κ_d	Attenuation coefficient of detritus	calculated	m^{-1}
K_P	Half-saturation constant for grazing	1.0	mmol-N m^{-3}
Ks_1	Half-saturation constant for nitrate	1[8]	mmol m^{-3}
Ks_2	Half-saturation constant for silicate	4.0[8]	mmol m^{-3}
Ks_3	Half-saturation constant for phosphate	0.2[8]	mmol m^{-3}
L_{lim}	Light limitation	calculated	dimensionless
M_{Phy}	Specific mortality rate of phytoplankton	0.05[1,6]	d^{-1}
M_Z	Specific mortality rate of zooplankton	0.01	d^{-1}
N_{coag}	Parameter (eq. 2.50)	15[5]	(mmol-N m^{-3})$^{-1}$
N_i	Concentration of nutrients (i =1 to 3)	calculated	mmol m^{-3}
N_{lim}	Nutrient limitation	calculated	dimensionless
M	Specific phytoplankton growth rate	calculated	d^{-1}
μ_{max}	Maximum phytoplankton growth rate	calculated	d^{-1}
μ_0	Specific phytoplankton growth rate at 0°C	0.8511	d^{-1}
Phy	Phytoplankton biomass	Calculated, T dep	mmol-N m^{-3}
P_m^B	Maximum photosynthetic rate	1.8[2,3]	mg-C (mg-chl *a*)$^{-1}$ h^{-1}
r_m	Maximum zooplankton grazing rate	0.5	d^{-1}
r_u	Parameter eq. (2.52)	0.0633	(°C)$^{-1}$
Si_{coag}	Parametr (eq. 2.50)	30.4	(mmol Si m^{-3})$^{-1}$
w_f	Sinking rate for ice algae and fats-sinking detritus	50[6]	m d^{-1}
w_s	Sinking rate for slow-sinking detritus	1[6]	m d^{-1}

[1]Chai et al. [2002], [2]Harrison and Platt. [1986], [3]Sakshaug and Slagstad [1991], [4]Subba Rao and Platt [1984], [5]Wassmann and Slagstad [1993], [6]Slagstad et al. [1999], [7]Bidle and Azam. [1999], [8]Lancelot et al. [2000].

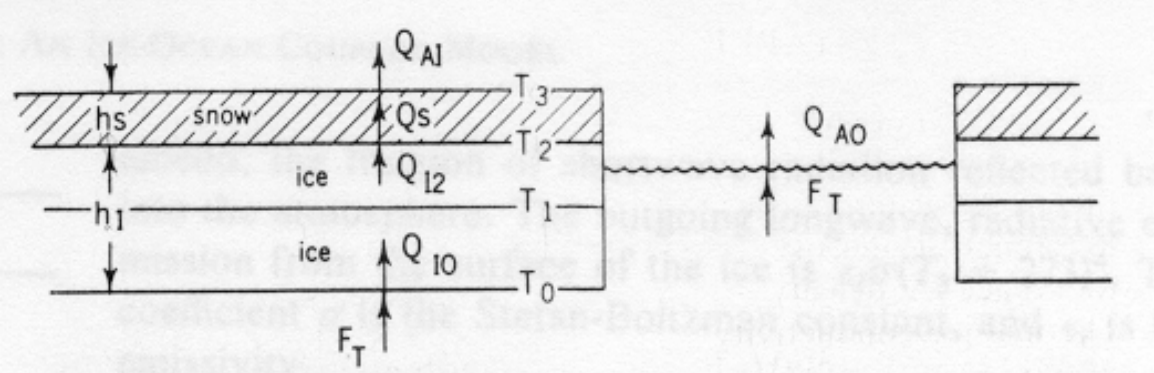

Figure 2.1. Schematic representation of the sea ice model (from Mellor and Kantha [1989]). T_i (i = 0,2,3) are interface temperatures and T_1 is the 'internal' ice temperature midway through the ice layer. Fluxes are positive upward.

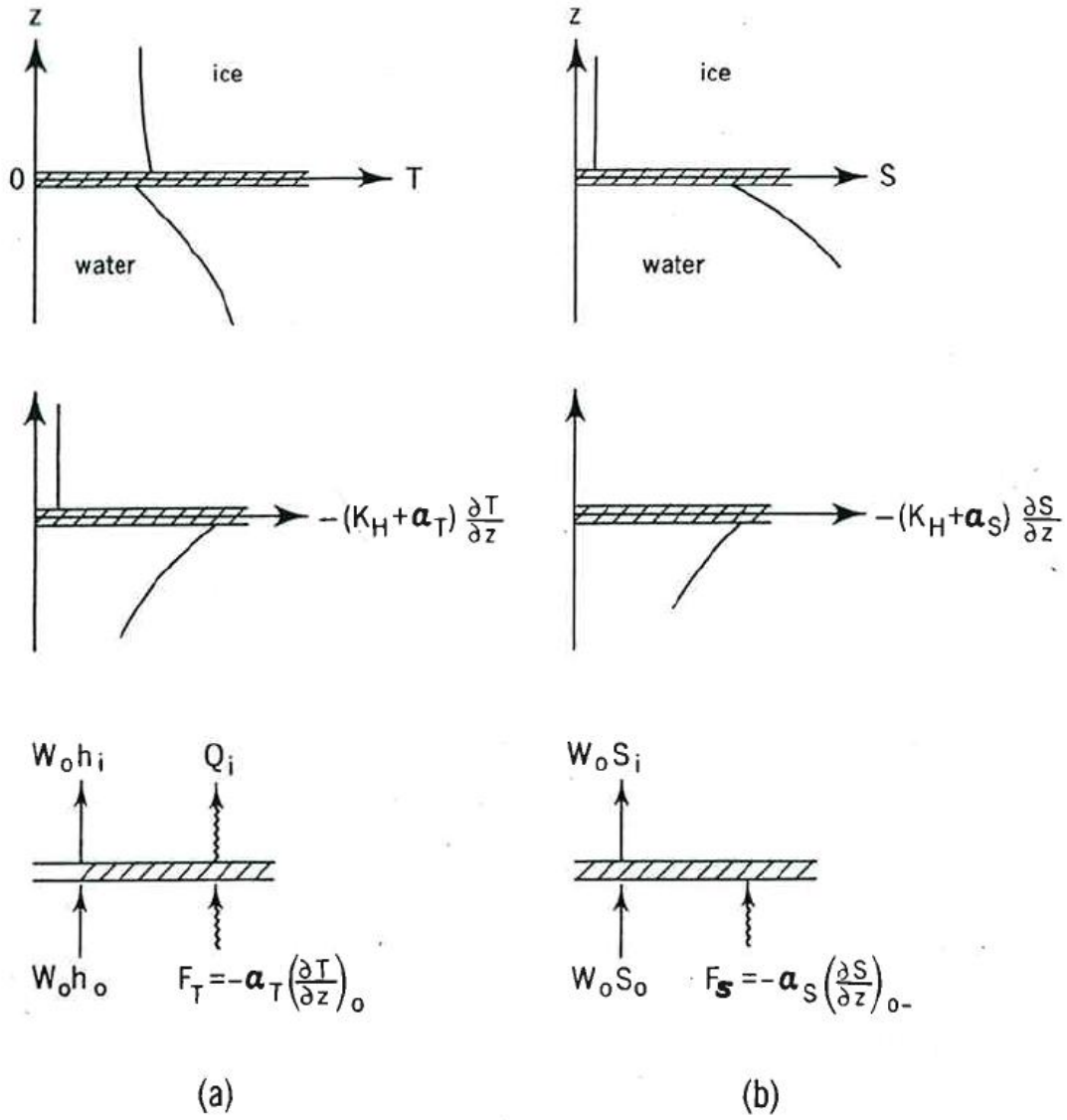

Figure 2.2 Schematic of the properties (upper panels), fluxes (middle panel) and interfacial advection and flux balance (lower panel) for (a) temperature and (b) salinity. The subscript *I* denotes values on the ice side at z = 0+ whereas the subscript 0 denotes values on the water side at z = 0-. The shaded portion represents an indefinitely thin control volume surrounding the seawater, sea-ice interface. From Mellor et al. [1986].

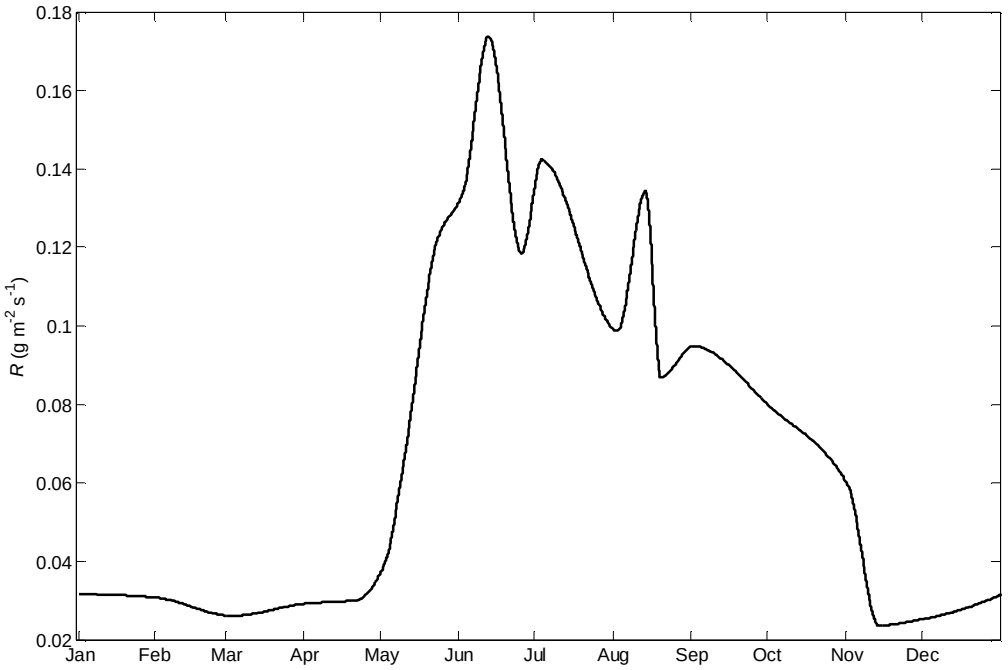

Figure 2.3. Flux of fresh water into the top of the mixed layer to represent lateral advection of the Mackenzie river runoff in 1987.

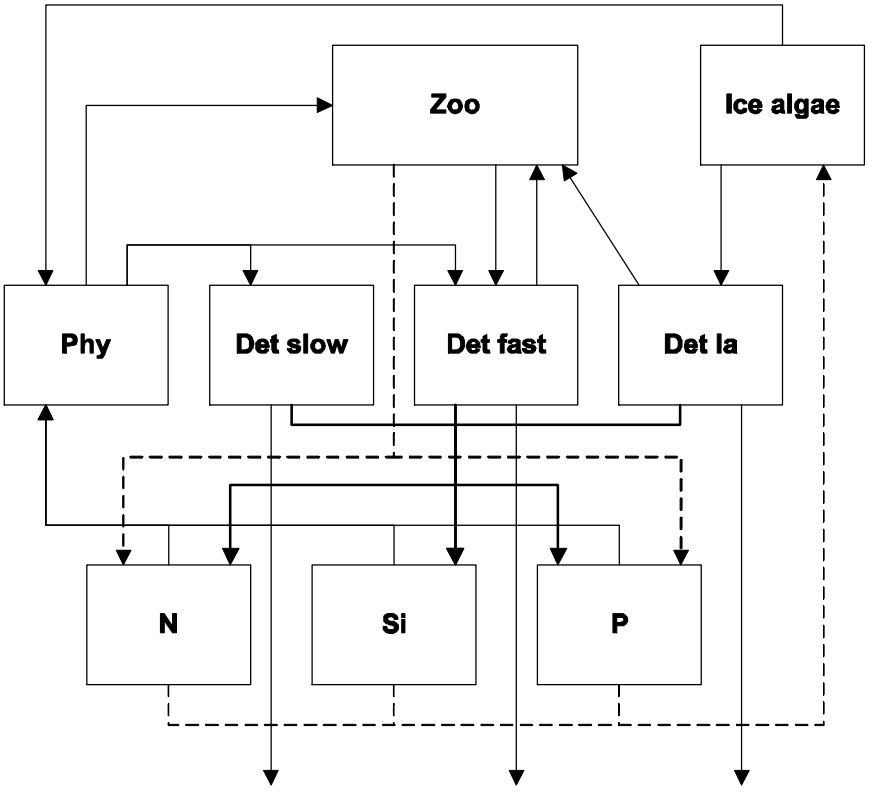

Figure 2.4. Schematic diagram for the biological model.

3. Modelling ice algal growth and decline in a seasonally ice-covered region of the Arctic (Resolute Passage, Canadian Archipelago)

3.1. Introduction

The Arctic is the region of the globe where climate warming is most pronounced [Anisimov et al., 2001], due in great part to the ice-albedo feedback [Curry et al., 1995]. Although changes resulting from this warming differ regionally, the ocean surface in the Arctic is generally becoming fresher [SEARCH SSC, 2001] while the sea ice extent [Johannessen et al., 1999, 2004; Parkinson et al., 1999; Vinnikov et al., 1999] and thickness [Rothrock et al., 1999] are decreasing, although trends in ice thickness are more difficult to assess [Holloway and Sou, 2002; Johannessen et al., 2004]. An increase in winter precipitation, resulting from warmer conditions, is also expected [Serreze et al., 2000], and a tendency toward earlier snowmelt onset has been observed across much of the western Arctic in the last two decades [Anderson and Drobot, 2001]. All these changes may significantly affect the functioning of the marine ecosystem [SEARCH SSC, 2001]. For example, changes in ice and snow cover may have a strong impact on the microalgae growing at the base of the ice. Although the latter represent a relatively small percentage of total primary production in the Arctic Ocean (less than 25%) [Legendre et al., 1992], they play an important role in sustaining secondary production, both pelagic and benthic [e.g., Tynan and DeMaster, 1997; Conover et al., 1986; Michel et al., 1996, 1997]. It is also believed that ice algae (composed mainly of pennate diatoms, see Horner [1985]) can influence the structure of the pelagic food web by seeding the ice edge phytoplankton bloom, and thus determine whether it is diatom or microbially-based [see Leventer, 2003]. The production of exopolymeric substances by ice algae also represents a previously unrecognized form of organic matter that can contribute significantly in carbon export to deep regions of the Arctic Ocean [Krembs et al., 2002]. Ice algae thus play an important role in the polar ecosystem and can also contribute to CO_2 drawdown in the Arctic. To forecast how ice algae will be affected by changes in their environment, we

must first understand what factors control the magnitude and variability of ice algal primary production and biomass accumulation.

Ice algal growth is regulated by light [e.g., Michel et al., 1988; Welch and Bergmann, 1989; Gosselin et al., 1990], nutrients [e.g., Gosselin et al., 1990; Cota et al., 1987, 1990] and substrate [e.g., Welch and Bergmann, 1989; Gosselin et al., 1986; Legendre et al., 1991]. These are in turn controlled by various factors that are often interdependent, making it difficult to identify the most important processes. Snow thickness, through its control on irradiance, is the major factor regulating the onset of ice algal blooms [e.g., Cota and Smith, 1991; Welch and Bergman, 1989]. After an exponential growth phase, biomass levels can plateau or oscillate before the final decline [Cota and Smith, 1991]. Exactly what controls biomass fluctuations and bloom decline is still unclear, although the latter usually coincides with snow and bottom ice melt [Cota and Smith, 1991; Fortier et al., 2002]. An earlier snowmelt onset, as mentioned above, could thus imply a shorter ice algal bloom duration. Fortier et al. [2002] also suggested that the speed of snow melting could influence the sinking rate of the algae, with rapid melting leading to accelerated release of the algae from the ice and rapid sinking. They hypothesize that abrupt release of ice algae in areas covered by seasonal ice will be more frequent with the increase of early rain and warm periods.

Nutrients are supplied to the ice algae through brine drainage, in situ regeneration of biogenic materials, and exchanges with the mixed layer [Meguro et al., 1967]. In Arctic first-year ice, most of the biomass is found in the bottom 2-cm of the ice (~95% [e.g., Perovich et al., 1993]), which consists of thin platelets of ice forming a layer called the skeletal layer (SKL) [Maykut, 1985]. Nutrient supply from the water column appears to be most important in this layer and would ultimately be limited by diffusion across the molecular sublayer immediately adjacent to the ice [Cota et al., 1987]. Evidence for this process is the observed coupling between ice algal biomass and fortnightly tides in the Canadian Archipelago (Resolute Passage area). Although direct measurements of nutrient concentration in the ice matrix and SKL are difficult to make [Cota and Horne, 1989], nutrient limitation of ice algae can be inferred from changes in biomass, nutrient ratios

and distributions, photosynthetic performance, patterns of photosynthate allocation and biochemical composition [Cota et al., 1991, and references therein]. These factors point to nutrient limitation of ice algae during neap tide, even when the nutrient concentration in the upper mixed layer is not limiting [Cota et al., 1987; Cota and Horne, 1989; Conover et al., 1990]. Changes in friction velocity over the fortnightly tidal cycle induce changes in the thickness of the molecular sublayer (thicker during neap tide), and thus in nutrient fluxes to the SKL, and likely explain the observed variations in ice algal biomass associated with the tidal cycle. This mechanism has yet to be clearly demonstrated: one of the goals of this paper is to examine the importance of the molecular sublayer thickness in regulating nutrient limitation.

Although light and nutrients are generally considered the main factors controlling the accumulation of ice algal biomass in the bottom ice layer, Legendre et al. [1991] found that ice growth rate was the most important factor controlling ice algal distribution and biomass along a transect in Hudson Bay. Higher biomass was found in areas with low ice growth rate. Other studies showed that factors linked to ice growth rate, such as ice structure [e.g., Gosselin et al., 1986; Eicken, 1992] or vertical brine stability [Krembs et al., 2001], were also controlling factors. Lizotte [2003] mentions the loss of microhabitat caused by melting at the ice-water interface as a cause for termination of the bloom. Ice growth rate also affects the supply of nutrient to the bottom layer. During positive ice growth, convection in the SKL enhances the nutrient fluxes [e.g., Reeburgh, 1984; Cota et al., 1991]. During negative growth (melt) the supply of freshwater increases the stratification just below the ice and reduces the flux of nutrient to the ice-ocean interface [e.g., Gosselin et al., 1985]. Ice properties and growth rate are usually not measured during biological sampling. The measurements and model presented in this paper allow us to investigate the importance of ice growth rate in controlling ice algal accumulation.

Modelling of ice algal growth and biomass has been limited to a few sea ice habitats in the Antarctic [e.g., Arrigo et al., 1993]. In this paper we develop a coupled snow-ice-ice algae model to investigate the importance of different limiting factors (light, nutrients, ice growth rate) on ice algal growth and decline and on biomass accumulation. More

specifically we investigate the importance of the molecular sublayer thickness in regulating nutrient fluxes to the SKL, the relative importance of light (as controlled by the snow cover) and nutrients on ice algal growth, and finally the importance of the ice melt rate on biomass accumulation and bloom decline. Our ice algae model is roughly based on that of Arrigo et al. [1993] who developed a 1D landfast ice ecosystem model for ice algal growth in McMurdo Sound (Antarctica). In their model, the physiological response of ice algae is a function of the ambient temperature, spectral irradiance, nutrient concentration and salinity. The structure of Antarctic sea ice differs from Arctic sea ice and its colonization by ice algae is more extensive vertically [see Ackley and Sullivan, 1994]: Antarctic ice algae are found at the snow-ice interface, within the congelation ice (~ lower 20 cm) and in the platelet ice layer (which is more common in the Antarctic than in the Arctic). The model of Arrigo et al. [1993] thus includes a complex treatment of the brine temperature and salinity which is not required for ice algae growing in the SKL. Also, the visible light (400-700 nm) is treated as one spectral band in our model. Our model is thus simpler but considers more physical processes: the oceanic heat flux in our model is variable and the ice model is coupled to the mixed layer through the molecular sublayer, whose thickness is variable and controls the heat, salt and nutrient fluxes to the bottom of the ice. We have also added an important ice algal loss term resulting from bottom ice melting.

We evaluate the model results with data from the Canadian Archipelago (Barrow Strait). This region supports high ice-algal production [e.g., Smith et al., 1988; Welch and Bergmann, 1989], but the maximum biomass varies interannually (from about 20 to 350 mg-chl *a* m^{-2} under low snow cover [Cota and Smith, 1991; Smith et al., 1990; Fortier et al., 2002]), even when snow-ice thicknesses are similar. We also use our model results to (i) infer a possible explanation for this considerable interannual variability, and (ii) examine the potential effect of climate change on ice algal production in the Arctic.

3.2. Study area and field observations

Field observations were carried out in 2002 at a landfast ice station in Resolute Passage (74°42.5'N, 95°49.5'W), adjacent to Barrow Strait, in the Canadian Arctic Archipelago (Figure 3.1). Water depth at the sampling station was 120 m. Waters flowing through the Archipelago consist mainly of nutrient-rich Pacific origin Arctic Ocean surface and near-surface water, due to the presence of sills in the various channels [Prinsenberg and Bennett, 1987; Jones et al., 2003]. The stratification near the sampling site is weak: the water is often nearly homogeneous down to the bottom, although stratification varies due to tidal modulation of mixing and continuous horizontal advection of water masses with different salinities [Prinsenberg and Bennett, 1987]. The tidal flow is dominated by the K_1 and M_2 constituents with speeds reaching 60 cm s^{-1} [Cota et al., 1987]. The maximum tidal range in the Resolute Bay area is about 2 m [Conover et al., 1990]. At the latitude of the study site, the polar night extends from the second week of November to the first week of February. Although interannual variability occurs, on average, first-year landfast ice forms in the Resolute area at the end of September and disappears at the beginning of August [Brown and Cote, 1992]. At the end of May, the ice reaches an average maximum thickness of ~2 m, while the snow cover reaches an average maximum thickness of ~ 22 cm.

From May 8 to July 3, 2002, continuous measurements (15 min. sampling interval) of under-ice photosynthetically available radiation (PAR, 400-700 nm) were made with a LiCOR quantum sensor (LI-192SA) installed horizontally at 0.5 m below the undersurface of the ice, and connected to a LiCOR 1400 data logger. Snow depth was measured daily at the same site (referred to as the PAR site), with care taken to not disturb the area near the sensor. Meteorological data, including downwelling PAR, wind, air temperature and relative humidity were recorded at the sampling station, from May 9 to June 26. Upwelling PAR was also recorded on some occasions to estimate the surface albedo. Atmospheric PAR data were collected with a LiCOR LI-190SA quantum sensor. Cloud cover fraction and opacity were obtained from Environment Canada, in Resolute Bay, about 30 km southeast of the sampling site. Some gaps in the on-site meteorological data were filled with data from the Environment Canada station. From May 2 to July 4,

continuous under-ice temperature and conductivity measurements were obtained with a Sea-Bird SBE37 probe that was moored at 1 m underneath the ice. Salinity and density were calculated using standard UNESCO formulas. Biological ice sampling and water column sampling took place at 3-4 day intervals. From May 2 to July 2, water column samples were collected at four depths (2.5, 5, 10 and 25 m), using Niskin bottles. Nutrient subsamples were immediately collected from the Niskin bottles, and frozen in liquid nitrogen until concentrations of PO_4^{3-}, NO_3^-, and $Si(OH)_4$ were determined with a Technicon autoanalyzer. From May 2 to June 29, ice algae were sampled at two sites of different snow thickness (~10 cm and ~20 cm) with a MARK II coring system (9 cm inner diameter; Kovacs Enterprise, Lebanon, New Hampshire). The bottom 2-4 cm of each core, where most of the algal biomass was observed, was immediately cut off and put in a dark isothermal container. The cores were melted in surface seawater collected at the time of sampling and filtered through 0.22 μm membrane filters to minimize osmotic stress during melting [Garrison and Buck, 1986]. Snow and ice thicknesses were measured at both coring sites, which will be referred to as the low snow cover (LSC) and high snow cover (HSC) sites. Chlorophyll *a* (chl *a*) was determined fluorometrically, on a Turner Designs 10AU fluorometer calibrated against pure chl *a* extract (Sigma Chemicals), on duplicate subsamples filtered onto Whatman GF/F filters after extraction in acetone 90% during 24h at 4°C in the dark [Parsons et al., 1984].

3.3. Model description

This section describes the sea ice and ice algae models. Variables and parameters for models are defined in Table 3.1. PAR attenuation coefficients for all media (snow, ice, ice algae and water) are presented in a subsection (3.3.1.2) of the sea ice model.

3.3.1 Sea ice model

The one-dimensional thermodynamic sea ice model is based on the model of Mellor and Kantha [1989], which is similar to the lowest-resolution ice model of Semtner [1976], which in turn is a simplified version of the Maykut and Untersteiner [1971] model. The model consists of one layer of snow and two layers of ice. We first constrained the

thermodynamic model with observations obtained at a multi-year ice site in the Beaufort Sea from the SHEBA project (http://sheba.apl.washington.edu). Some changes have been made to the ice model of Mellor and Kantha [1989] and are described in the Appendix.

3.3.1.1 Snow and ice thickness

We do not model the snow thickness in this study since there is usually a mismatch between snowpack development and snowfall measured at Resolute due to redistribution of snow by wind action [see Brown and Cote, 1992]. Rather, a cubic spline function was fitted to the observations of snow thickness and given as input to the model. When no snow remains and surface melt is occurring, the surface temperature is fixed at the melting point of freshwater ice and the resulting imbalance between the net heat flux absorbed at the upper surface boundary (Q_{AI}) and the conductive flux at the surface (Q_{I2}) causes melting at the top of the ice according to

$$M_t = \frac{-Q_{AI} + Q_{I2}}{r_i L_i} \tag{3.1}$$

where L_i is the latent heat of fusion of sea ice and ρ_i is the density of sea ice. Fluxes are positive upward. A similar equation applies to melting and accretion at the ice underside:

$$M_b = \frac{Q_{IO} - F_T}{r_i L_i} \tag{3.2}$$

for a total change in ice thickness of

$$\frac{\partial h_i}{\partial t} = M_t + M_b . \tag{3.3}$$

In eq. (3.2), Q_{IO} is the conductive flux at the bottom of the ice and F_T is the heat flux from the ocean mixed layer, calculated after McPhee [1992]. The mixed layer properties for the calculation of F_T are taken from the under-ice CTD observations (see section 3.2).

3.3.1.2 PAR attenuation coefficients

As in the work of Zeebe et al. [1996], it is assumed that the fraction (i_0) of incoming shortwave solar radiation (*SW*, wavelengths ≤ 4000 nm) that penetrates the ice-snow surface consists of the visible band (PAR) only. The remaining radiation ((1-i_0)*SW*) is absorbed in the first few centimeters of the snow or ice layer and contributes to the energy balance at the surface. Calculation of i_0 is based on Grenfell and Maykut [1977] values for first-year ice under cloudy and clear sky. PAR at the surface (PAR_0) is thus equal to

$$PAR_0 = i_0(1-\alpha)SW \qquad (3.4)$$

where α is the surface albedo (which depends on snow and ice thicknesses and temperature, see Appendix) and *SW* is calculated after Parkinson and Washington [1989]. The distribution of PAR within the ice or snow is assumed to follow Beer's law [Maykut 1985],

$$PAR(z) = PAR_0 e^{-kz} \qquad (3.5)$$

where *z* is the depth below the snow or ice surface and κ is the snow or ice attenuation coefficient. Attenuation coefficients are lower for the visible band wavelengths than at other wavelengths of the solar spectrum [e.g., Grenfell and Maykut, 1977]. Based on previous studies [Grenfell and Maykut, 1977; Smith et al., 1988; Ebert et al., 1995] as well as on the light measurements made at the study site, we chose the following PAR attenuation coefficients: 1.2 m^{-1} for the ice, 14.0 m^{-1} for dry snow and 7.5 m^{-1} for melting snow.

The attenuation coefficient for ice algae (κ_{chl}) is defined as [e.g., Kirk, 1983]

$$\kappa_{chl} = a^*[chl\ a] \qquad (3.6)$$

where a^* is the mean chl *a*-specific attenuation coefficient (0.02 m^2 (mg-chl *a*)$^{-1}$), and [*chl a*] is the concentration of chl *a* (mg-chl *a* m^{-3}) at the bottom of the ice. Our value for

a^* is larger than the range of values 0.01-0.016 m^2 (mg-chl *a*)$^{-1}$ reported by Perovich et al. [1993] and Suzuki et al. [1997] but within the range of the values reported by Smith et al. [1988], i.e., 0.0116 and 0.035 m^2 (mg-chl *a*)$^{-1}$ (all measured in the same area). The attenuation coefficient for water below the ice was estimated to be 0.2 m^{-1} after Smith and Baker [1978] (assuming an average upper water chl *a* concentration slightly less than 1 mg m^{-3}) and Pegau [2002].

3.3.2 Ice algae model

3.3.2.1 Nutrient limitation

In Resolute Passage, pennate diatoms, mainly *Nitzshia* species, can contribute up to 95% of total cell numbers in the bottom ice community [Michel et al., 1996]. Thus, in addition to nitrogen and phosphate, silicon is required for ice algal growth. Although some studies indicate that nitrogen [e.g., Smith et al., 1997] is the potential limiting nutrient for ice algae in fully marine waters, most studies point to silicon [e.g., Cota and Horne, 1989; Cota et al., 1990; Gosselin et al., 1990; Smith et al., 1990]. Effective regeneration of N and P can take place in the ice while dissolution of biogenic silica occurs too slowly to provide significant recycling of silicic acid [Harrison and Cota, 1991; Lizotte, 2003]. Thus, we concentrate on silicon regulation and supply in our model.

From Michaelis-Menten kinetics, the nutrient limitation is formulated as

$$N_{\lim} = \frac{Nskel}{K_s + Nskel} \tag{3.7}$$

where *Nskel* is the concentration of $Si(OH)_4$ in the SKL (see Figure 3.2) and K_s is the half-saturation constant for $Si(OH)_4$ uptake (4.0 mmol m^{-3} [e.g., Sarthou et al., 2005]).

3.3.2.2 Light limitation

The light limitation factor is calculated with the hyperbolic tangent function of Jassby and Platt [1976]

$$L_{\lim} = \tanh\left(\frac{\alpha^B PAR(z_a)}{P_m^B}\right) \qquad (3.8)$$

where z_a is the depth, within the ice, of the top of the ice algal layer, α^B is the photosynthetic efficiency and $P^B{}_m$ is the maximum (light-saturated) photosynthetic rate of ice algae. The photosynthetic parameters are different for each of the three sites (Table 3.2) due to differences in shade adaptation. Ice algal growth occurs only at light levels greater than the compensation intensity, which was fixed at 0.4 μEinst m^{-2} s^{-1} [Conover et al., 1990; Cota and Smith, 1991]. In eq. (3.8), $PAR(z_a)$ is converted from W m^{-2} into Einst m^{-2} s^{-1} with a ratio of 4.56×10^{-6}, obtained by dividing the average ratio of total quanta to total energy (2.77×10^{18} quanta s^{-1} W^{-1} in Morel and Smith [1974]) by the Avogadro number (6.022×10^{23} mol^{-1}).

3.3.2.3 Ice growth rate limitation

Ice algae have the ability to maintain their position at the bottom of the ice [Welch and Bergmann, 1989; Reeburgh, 1984]. However, we hypothesize that the algae cannot maintain their position when the ice growth rate exceeds a certain level, being either trapped in the ice matrix and advected up as the ice grows (positive growth) or expelled to the water column when the ice melts (negative growth). For the positive growth, the critical ice growth rate appears to be between 1.7 - 2.9 cm d^{-1} [Krembs et al., 2001; Legendre et al., 1991], while for the negative growth (melting), it appears to be around -1.5 cm d^{-1}. This critical melt rate was determined from comparison of the observed chl *a* concentration in the bottom of the ice with the calculated ice melt rate. We formulate here a new limiting term to account for the inability of the ice algae to accumulate in the skeletal layer at certain ice growth rates. As the ice was melting for most of the study period, we fitted a linear function between zero and the critical ice melt rate,

$$IGR_{\lim} = \begin{cases} 0 & \text{when } |M_b| \geq 1.5 \text{ cm d}^{-1} \\ 1 - \dfrac{|M_b|}{1.5} & \text{when } 0 < |M_b| < 1.5 \text{ cm d}^{-1} \end{cases} \qquad (3.9)$$

where M_b is the ice growth rate.

3.3.2.4 Ice algal growth rate

Assuming that the ice algal growth is limited by only one factor at any time, the specific ice algal growth rate is

$$m = m_{\max} \min(N_{\lim}, L_{\lim}, IGR_{\lim}) \qquad (3.10)$$

where $\mu_{\max}$ is the maximum (non-limited) specific ice algal growth rate ($\log_e$) predicted from the relationship of Eppley [1972]. The expression min($N_{\lim}$, $L_{\lim}$, $IGR_{\lim}$) takes the value of the most limiting factor (between 0 and 1). Although the maximum growth rate is temperature-dependent, the temperature in the bottom 2 cm of the ice varies little (~ -1.8°C) and thus $\mu_{\max}$ remains close to 0.53 d^{-1}.

3.3.2.5 Ice algal loss rates

Ice algae can potentially be grazed in the ice matrix by large protozoa (e.g. flagellates and ciliates) [Vézina et al., 1997], metazoa (e.g. nematodes), and amphipods, although the presence of the latter is more important in shallow water areas [e.g., Welch and Bergmann, 1989]. Copepods also feed on the ice algae but it appears that they feed on cells that are sloughed off the ice [Conover et al., 1986; Hattori and Saito, 1997]. As many uncertainties remain, we set the grazing rate (G) as a constant fraction (gr=0.10) of the net ice algal growth rate (m).

Ice algal cells are frequently lost to the water column in spring [e.g., Conover et al., 1990]. We believe these losses result from warming and melting of the bottom-ice. Warming of the bottom of the ice results from heat exchange with the underlying water column, from radiation absorption by the ice, but also from the heat released by the ice algae, which absorb more PAR than that required for photosynthesis. The higher amount of PAR reaching the base of the ice under low snow cover would explain why ice algal losses are higher under these areas, as suggested by Smith et al. [1988]. The energy that is released as heat by the algae is equal to

$$F_{ia} = PAR(z_a) \cdot fr \cdot (1 - e^{-k_{chl} h_a}) \quad (3.11)$$

where h_a is the thickness of the ice algal layer and fr is the fraction of the energy absorbed by the ice algal layer that is released as heat [Zeebe et al., 1996]. Assuming all the heat goes to melting ice in the bottom 2 cm of the ice, the "biological" rate of ice melting is equal to

$$M_a = \frac{F_{ia}}{r_i L_i} \quad (3.12)$$

The change in thickness due to the "physical" ice melt at the bottom is described in eq. (3.2). To differentiate these two processes in the discussion, we will refer to the loss of ice algae associated with melting resulting from ice algal heat release as "biological melt loss", while the loss associated with external heating will be referred to as "physical melt loss".

3.3.2.6 Ice algal biomass

The rate of change in ice algal biomass is calculated as follows

$$\frac{\partial B}{\partial t} = B\left[m - G - \frac{Q_{IO} - F_T + F_{ia}}{r_i L_i h_a} \right] \quad (3.13)$$

where B is the biomass and the last term represents the thickness of ice melted by the "physical" and "biological" heat sources (sum of eqs (3.2) and (3.12)), over the thickness of ice where the ice algae are growing (h_a), to give the fraction of the ice algal biomass that is lost through ice melting at each time step.

3.3.2.7 Nutrient concentration

The mixed layer is the main supplier of nutrient to the SKL [Cota et al., 1987] and thus only the flux from the mixed layer is considered in the model. The different layers are shown schematically in Figure 3.2. The concentration of nutrient at the top of the mixed

layer is governed by the difference between the supply from deeper in the mixed layer and the loss through diffusion across the molecular sublayer. The physical supply of nutrient to the top of the mixed layer is equal to

$$F_N = \frac{\partial N}{\partial z} K \,, \tag{3.14}$$

where $\partial N/\partial z$ is the vertical gradient (mmol m^{-4}) of $Si(OH)_4$ between the concentration calculated below the molecular sublayer (below the ice) and the concentration measured at 2.5 m, and K is the mean (time-varying) eddy diffusion coefficient over the same depth range. The supply of nutrient to the SKL is equal to

$$F_{Nskel} = \frac{dNskel}{h_n} D \tag{3.15}$$

where $\delta Nskel/h_v$ is the nutrient gradient across the molecular sublayer of thickness h_v, and D is the molecular diffusion coefficient for $Si(OH)_4$.

Both K and h_v vary with the tidal cycle (Figure 3.3). The timing of the neap-spring tidal cycle was determined from tidal predictions made by the Hydrographic Service of Canada. Average eddy diffusion coefficients for neap ($5x10^{-4}$ m^2 s^{-1}) and spring ($1.5x10^{-3}$ m^2 s^{-1}) tides were provided by R. Marsden and determined from an acoustic Doppler current profiler (ADCP) deployed in the study area in May 2002 (unpublished data, 2002). These values are similar to values found by Shirasawa and Ingram [1997]. The eddy diffusion coefficient is assumed to be equal to the eddy viscosity coefficient [see Crawford et al., 1999, and references therein]. Roughness lengths (z_0) calculated by different authors in or near the study area were small (0.0017-0.2 cm), suggesting that the ice-water interface was hydro-dynamically smooth [e.g., McPhee, 1990; Crawford et al., 1999]. The exchanges of heat, salt and nutrients would thus be dominated by molecular exchange across the molecular sublayer, of thickness h_v, which is estimated as [Tennekes and Lumley, 1972],

$$h_n = \frac{n}{u_t} \tag{3.16}$$

where ν is the kinematic viscosity of seawater and u_τ is the friction velocity. The latter also varies with the tidal cycle and is treated in the same way as K with average values of 8×10^{-3} and 4×10^{-3} m s^{-1} for spring and neap tides (based on R. Marsden's ADCP data and Shirasawa and Ingram [1997]). We use a molecular diffusion coefficient D equal to 1×10^{-9} m^2 s^{-1} for $Si(OH)_4$. This value was obtained after reducing the value measured by Applin [1987] for freshwater (2.2×10^{-9} m^2 s^{-1}) by 8% to obtain the seawater value at 25°C and a salinity of 36.1 [Li and Gregory, 1974], and dividing by two to obtain a value of D at a temperature of 0°C.

The uptake of nutrient for an algal concentration B in the SKL is equal to

$$Nup = m \cdot B \frac{N}{Chla} \tag{3.17}$$

where μ is given by eq. (3.10) and $N/Chla$ is the ratio (weight:weight) of nutrient required (silicate in this case) to chl a produced. An average ratio of biogenic Si to chl a of 17 is used, based on measurements over the study period. The time evolution of nutrient concentration in the SKL is then given by

$$\frac{\partial Nskel}{\partial t} = \frac{F_{Nskel} - Nup}{h_a}. \tag{3.18}$$

3.4. Results

3.4.1 Light field at the PAR site

We first use data from the PAR site (see section 3.2) to constrain the light attenuation coefficients of snow, ice and ice algae, and the PAR values calculated for the different

interfaces of the model (e.g. surface of snow or ice, top of the ice algal layer). Estimating the correct amount of PAR at each interface is required for simulating accurate ice thickness and temperature, as well as ice algal biomass. Figure 3.4 shows the time series of observed and simulated PAR at the surface (Panel a) as well as below the ice (top of mixed layer) and the simulated PAR immediately above the ice algal layer (Panels b and c), for the sampling period, starting May 10 (day 130) and ending July 2 (day 182). Upwelling PAR was measured only once during the day and was used to estimate the surface albedo. We use this albedo value as a daily mean to obtain the "observed" PAR at the surface. This may be a source of error since the surface and atmospheric conditions change over the day, leading to changes in the albedo. However, the resulting "observed" PAR at the surface compares well with the simulated PAR_0 (Figure 3.4a). Discrepancies between the two curves occur at times where the simulated surface temperature reaches 0ºC and when the snow disappears, which both lead to changes in the simulated albedo.

The amount of PAR that reaches the top of the ice algal layer (Figure 3.4c) is strongly dependent on the temperature and thickness of the snow layer (Figure 3.4d and e). The thickness and properties of the ice become increasingly important as the snow melts. The concentration of ice algae at the bottom of the ice (Figure 3.4f) determines what fraction of the PAR transmitted through the ice will reach the mixed layer (Figure 3.4b and c). Since ice algal biomass and ice thickness were not measured at the PAR site (to avoid disturbance to the site), we compare the model results with the data collected at the nearby coring sites (Figure3. 4e and f). The thickness of snow cover observed at the PAR site was closer to that at the HSC site, although it varied between snow thicknesses measured at the LSC and HSC sites (compare with Figure 3.5). The resulting biomass simulated at the PAR site thus varies between the biomass concentrations measured at the two coring sites, as depicted in Figure 3.5f. Overall, the underwater PAR estimated from the model compares well with the observations. Some discrepancies occur - to be discussed in a later section.

3.4.2 Ice algal growth and decline

We now apply the light attenuation coefficients obtained using the data collected at the PAR site to simulate the ice algal growth and decline at the high snow and low snow coring sites (HSC and LSC). Overall, the modelled ice thickness compares well with the observations (Figure 3.5a). The ice was melting (at the bottom) over most of the study period (with the exception of a short period at the beginning). The modelled ice also melts from the top at the HSC site, after the disappearance of the snow cover on day 173 (Figure 3.5a). Figure 3.5b shows that, for most of May (until day 151), ice algal growth was essentially limited by light at the HSC site (L_{lim} being the minimum of the three limitation functions), while limitation oscillated between light (L_{lim}) and nutrient (N_{lim}) at the LSC site. Although more light reaches the top of the ice algal layer at the LSC site (I_0, Figure 3.5c), the difference in the photosynthetic parameters (see Table 3.2) leads to values of L_{lim} (eq. 3.8) that are of similar magnitude at both sites (Figure 3.5b). On the other hand, the higher ice algal biomass at the LSC site (Figure 3.5c) leads to a greater nutrient uptake (eq. 3.17) and to a reduction of nutrient in the SKL (Figure 3.6), which cannot always be replenished when the molecular sublayer thickness h_v increases during neap tide (Figure 3.3 and eq. 3.15). After day 151 (May 31), the snow thickness decreases at both sites (Figure 3.5a), leading to an increase in light penetrating the ice and reaching the top of the ice algal layer (Figure 3.5c). In the simulation, this decrease in light limitation (L_{lim} increases, Figure 3.5b) initially leads to an increase in the ice algal net growth rate (Figure 3.5d) quickly followed (within a day) by nutrient limitation. The increase in irradiance within the ice and ice algal layer after day 151 also leads to a rapid increase in internal ice temperature (Figure 3.7) and to an increase in cell loss due to "biological" melt (Figure 3.5d). The combined "biological" and "physical" melt losses are nearly equal to the net ice algal growth rate at the LSC site while at the HSC site, the net ice algal growth rate is greater than the losses, and the simulated biomass increases (Figure 3.5c and d). However, a significant decrease in biomass was observed at both sites, between days 153 and 156 at the HSC site, and between days 151 and 153 at the LSC site. The causes for this discrepancy between the model and observations are explored in the discussion.

The simulated ice algal biomass starts to decline at both sites on day 160, when the "physical" melt loss becomes greater than the ice algal net growth rate (Figure 3.5c and d). This transition coincides with a decrease in observed snow thickness (Figure 3.5a). Limitation of ice algal growth by the ice growth rate term (IGR_{lim}, Figure 3.5b) starts on day 172 (June 21), when the ice melt rate reaches a value of 0.8 cm d^{-1} (not shown). The simulated biomass completely disappears from the bottom of the ice within a week of limitation by the ice growth rate. The ice melt rate has then reached a peak value of 2 cm d^{-1}. The rapid decline in ice algal growth rate after day 172 is accompanied by an increase in the simulated concentration of silicic acid in the SKL, although the observed concentration of silicic acid at the LSC site remained low (Figure 3.6). The model results show that the silicic acid concentration in the skeletal layer follows a diel cycle when light is the limiting factor, the higher light limitation at night allowing for nutrient replenishment (compare Figure 3.5b and hourly mean in Figure 3.6). The ice algal mean specific growth rates calculated by the model between days 130 and 170 are respectively 0.15 d^{-1} and 0.18 d^{-1} at the LSC and HSC sites. These values are in agreement with those estimated from observations by other authors in the same region [see Cota and Smith, 1991].

3.5. Discussion

3.5.1 Model versus observations

3.5.1.1 Under-ice PAR

Bulk snow attenuation coefficients for PAR are high and vary over a large range: from 4.3 m^{-1} in dense snow to 40.1 m^{-1} in fresh snow [see Grenfell and Maykut, 1977]. The thickness and properties of the snow cover thus control in large part the amount of light that reaches the mixed layer. Most of the discrepancies between simulated and observed under-ice PAR in Figure 3.4c result because we use only two fixed values for the snow attenuation coefficient rather than a continuously varying value. Between days 130 and 132, snow fell while the winds were relatively calm, most likely resulting in increased attenuation of light by the snow cover leading to an overestimate in simulated under-ice PAR. The discrepancy on days 147, 151-153, and 156 (Figure 3.4c) occurred when the

simulated snow surface temperature reached a value of 0°C (Figure 3.4d), leading the model to use the wet snow attenuation coefficient (7.5 versus 14.0 m^{-1}, see section 3.3.2.3), which resulted in an increase in the light reaching the base of the ice. This discrepancy is amplified by the overestimation of PAR_0 on days 151, 152 and 156 (Figure 3.4a). Forcing the model to use the dry snow attenuation coefficient during this period leads to better agreement with observations (Figure 3.8). The progressive underestimation of simulated under-ice PAR starting on day 153 in Figure 3.8 most likely results from an actual gradual decrease of the snow attenuation coefficient due to surface warming (rather than a delayed step decrease to the wet snow coefficient as used in the model for Figure 3.4). In contrast, it appears that the underestimation in the simulated under-ice PAR after day 163 (Figure 3.4b and c) results from snow and ice attenuation coefficients that are both too high for this period of warming. The snow started to melt and most likely had an increasingly high water content, strongly reducing the attenuation coefficient. The ice also started to melt at its upper surface when the snow disappeared, generating melt ponds. The ice temperature also increased during this period (see ice temperature at HSC and LSC sites, Figure 3.7), leading to an increase of the brine volume and to a potential decrease in the number of inclusions [Perovich, 1998]. All these factors contribute to a reduction in the light attenuation coefficient of ice. However, this underestimate of PAR at the top of the ice algal layer in the model does not affect our biological results as light was not the limiting factor for ice algal growth after day 163 (Figure 3.6b).

3.5.1.2 Ice algal biomass

Snow and ice thicknesses, and ice algal biomass are all observed to vary spatially [e.g., Shirasawa and Ingram, 1997; Cota et al., 1991]; hence, care must be taken when comparing the model results with the observations, since the former are assumed to be at a fixed point in space while the ice core position varied (coring positions were chosen where snow thickness was close to 10 and 20 cm). These changes in core site position occasionally led to marked differences between cores sampled on the same or adjacent days, as between days 141-144 at the HSC site and on day 135 at the LSC site (Figure 3.5c). Snow was blowing at these times, and a site selected on a given day for its snow thickness of 10 or 20 cm could have had a very different snow thickness in the previous

few days, leading to variability in the observed ice thickness and ice algal biomass. Discrepancy between the simulated and observed ice algal biomass may also arise because the ice algae data were collected from the lower 2-4 cm of the ice core while the model considers the algae to grow in the bottom 2 cm only. As the ice warms, the brine channels get larger and eventually become interconnected allowing ice algae to grow upward into the ice. Indeed, chl *a* concentration in the ice in the Resolute area has been observed to be essentially restricted to the SKL in early spring, with a subsequent increase in vertical extent (until the beginning of bloom decline) [Smith et al., 1990; Cota et al., 1991]. Enlargement and interconnection of the brine channels would thus allow for a greater biomass accumulation at the bottom of the ice, although it could also lead to an increase in the loss terms, as discussed in the next section. Within the uncertainty created by these factors, the model reproduces well the general pattern of observed ice algal biomass. Biomass accumulates earlier in low snow cover areas due to higher irradiance levels [e.g., Smith et al., 1988], which would explain the higher observed biomass at the LSC site at the beginning of the sampling period (Figure 3.5c). However, a higher biomass eventually leads to earlier nutrient limitation, explaining the lower average simulated ice algal growth rate at the LSC site during the sampling period (see section 3.4.2). Short term variability in the simulated biomass results from the interplay between the different limiting factors (Figure 3.5b), which determine the evolution of the ice algal growth curve (Figure 3.5d), and the loss terms resulting from biological and physical ice melt (Figure 3.5d). These are complex interactions as both the nutrient limitation and the physical melt loss are affected in the same way by the thickness of the molecular sublayer (h_v). As h_v decreases, the fluxes of heat and nutrient to the bottom of the ice both increase. If ice algal growth was previously nutrient limited, it would increase, leading to an addition of biomass, while the increase in the heat flux would lead to increased physical melt loss. The difference between the two factors determines if there is a net gain or loss of biomass. In the same way, an increase in the amount of light reaching the ice algal layer can lead to an increase in biomass if the ice algae were light limited, but it also increases biological melt loss (mainly when the biomass is high). The importance of these competing factors on ice algal biomass accumulation is explored further in the following sections.

3.5.1.3 Effect of ice temperature and ice melt on ice algal decline

In this section, we will consider (i) the rapid decreases in the observed ice algal biomass that occurred at the beginning of June (between days 153 and 156 at the HSC site, and between days 151 and 153 at the LSC site, see Figure 3.5c), and (ii) the final ice algal decline. From the model results (section 3.4.2), we can see that the biomass decrease observed at the beginning of June is not due to an increase in bottom ice melt rate (the latter even decreased at the HSC site) or to a significant increase in biological melt loss. Nutrient limitation occurs in the simulation but not enough to suppress growth, which initially increased due to the increase in PAR. Moreover, the measured silicic acid concentration in the SKL reached maximal values on the first day of the decline at both sites. So what could explain the observed decline? The most likely mechanism, explaining both the decrease in observed biomass and the increase in SKL nutrient, is a rapid increase in ice temperature, especially at the LSC site (Figure 3.7), following the increase in air temperature (Figure 3.4d) and the decrease in snow cover thickness (Figure 3.5a). Ice warming leads to melting of brine channel walls, brine channel enlargement and brine channel interconnection (interconnection occurs at temperatures greater than -5°C [Golden, 2001]). Brine channel enlargement and interconnection favors the flushing of brine due to the development of a hydrostatic head produced by surface melting [Weeks and Ackley, 1986]. The decrease in snow thickness at the beginning of June most likely resulted from snow melt and could have led to brine flushing. Melting on the internal ice surfaces (e.g. brine channel walls), in conjunction with brine flushing, would limit the ability of the algae to attach to the ice and would lead to a greater loss of cells in the water column [Krembs et al., 2001]. Gradinger et al. [1991] explained the observed decrease of ice algal biomass in their study, as well as in other studies, with this same process. Brine flushing also favors the inflow of nutrient-rich seawater in the brine channels and could explain the high values of silicic acid in the SKL at the beginning of June [e.g., Hudier and Ingram, 1994]. High measured values of silicic acid in the SKL could result from the overnight recovery in SKL silicic acid concentration, as suggested by the model results (Figure 6), since the measurements were generally made in the morning, when PAR and ice algal growth values are halfway between their daily min and max. However, observed

values remained low for the first part of the sampling period, suggesting another cause for the high values observed later.

To investigate the effect of internal ice melt on ice algal loss, as depicted above, we added a new loss term to the model, proportional to the ice warming rate, that is effective only when the internal ice temperature is greater than -4°C and when the ice warming rate is greater than 0.17°C d^{-1}. The simulated ice algal biomass obtained when adding this new loss term does capture the observed drop in biomass between day 151 and 153 at the LSC site and (except for the high value observed on day 153) gives better agreement with observed algal concentrations at the HSC site after day 147 (Figure 3.9).

The final ice algal decline (starting on day 160 in the simulations) is clearly the result of the increase in ice melt (Figure 3.5d). Around day 160, the air temperature rises above 0°C and remains above 0°C for the rest of the sampling period except for a few nocturnal dips below 0°C (Figure 3.4d). This sustained warm period triggers snow melt (Figure 3.5a), ice warming (Figure 3.7), an increase in (i) in-ice (Figure 3.5c) and underwater PAR (Figure 3.4b and c), (ii) mixed layer temperature (not shown), (iii) ice melt (inferred from Figure 3.5d), (iv) ice algal physical and biological melt losses (Figure 3.5d), and (v) ice algal growth rate (Figure 3.5d). The difference between the increase in ice algal growth and physical plus biological melt loss determines the timing of the decline. This process was also suggested by Gosselin et al. [1985] as the reason for the ice algal bloom decline in Hudson Bay. The simulated decline in biomass is slower than the observed decline. This could result from the choice of the threshold ice melt rate in the calculation of IGR_{lim} (1.5 cm d^{-1}, eq. 3.9). The curve obtained using a lower threshold (0.85 cm d^{-1}) was plotted in Figure 3.9 for comparison, and gives better results. The more rapid decline could also result from increased internal ice melt and flushing, or a higher bottom ice melt rate than that obtained with the model. But it seems more likely that the decline is delayed by the weak nutrient limitation simulated at the end of the bloom (Figure 3.5b and Figure 3.6). Ice melting produces a freshwater lens of a few cm below the ice (e.g. lens thickness ~0.25-0.50 m in Gosselin et al. [1990]) which reduces the supply of nutrient through two mechanisms. First, the increase in density stratification just below the ice reduces the

upward mixing of nutrient, and second, the reduction in friction velocity at the ice-water interface leads to an increase in h_v that further reduces the diffusion of nutrient to the SKL. This explains why the observed nutrient concentration in the SKL remains low after the bloom decline (Figure 3.6, LSC site) while the simulated nutrient concentration increases to the mixed layer concentration level after day 170, as the effect of the melt lens is not accounted for in the model. This increase in the simulated nutrient concentration results in a high ice algal growth rate (Figure 3.5d) and is the cause for the "bump" in the simulated biomass between days 169 and 175. Osmotic shock due to the low salinity experienced in the boundary layer is also possible [e.g., Grant and Horner, 1976] but not likely as ice melt started to increase significantly on day 170, when most algal biomass had already disappeared (Figure 3.5 c and d). Measured bulk salinity in the lower part of the ice (not shown) also remained above 5 until day 170. The sensitivity of the model to different loss and limitation terms is explored in the next section.

3.5.2 Sensitivity analyses

The model results obtained in the sensitivity analyses will be plotted against the initial model results displayed in Figure 3.6, which will now be referred to as the "control run".

3.5.2.1 Molecular sublayer thickness

We first consider the effect of h_v on the ice algal biomass. We initially specified a constant h_v (0.3 mm), equal to the mean h_v simulated over the study period, to investigate the importance of tidal modulation on h_v and thus on the ice algal biomass. Although the tide does modulate ice algal growth and bottom ice melt, the differences in biomass over the study period obtained with a constant h_v are not significant (Figure 3.10). However, differences in the mean h_v significantly affects the ice algal biomass. Changing the friction velocity in eq. (3.16) to obtain a larger h_v (mean of 0.54 mm) results in a simulated biomass that is greater than in the control run (Figure 3.10), even though such a change reduces the nutrient supply from the mixed layer. This increase in biomass occurs because an increase in h_v also leads to a reduction in bottom ice melt [Steele et al., 1989], and thus to a lower ice algal melt loss. Because the reduction in physical melt loss is

greater than the reduction in ice algal growth rate, the simulated biomass increases. The opposite is true for a higher friction velocity (giving a smaller mean h_v), which leads to a reduction in biomass. However, a small h_v, combined with a lower oceanic heat flux (F_T), could lead to an increase in biomass. This sensitivity study suggests that interannual differences in oceanic heat fluxes in the Resolute area could explain the important variability in observed biomass.

3.5.2.2 Ice algal biological melt loss

Figure 3.11 shows that the biological melt loss term is not important when the in-ice irradiance is low. Removing the biological melt from the loss terms leads to significant changes in the simulated biomass at the LSC site, where the in-ice irradiance is higher (see Figure 3.5 c), while it causes only small changes to the biomass simulated at the HSC site (Figure 3.11). We also tested the sensitivity of the model to the fraction of radiation that is released as heat by the algae (*fr*). This fraction depends on the photosynthetic efficiency of the ice algae, with efficient algae releasing less heat than inefficient algae. We here use extreme values for *fr*, 0.85 and 0.99 [e.g., Zeebe et al., 1996]. The simulated biomasses are not sensitive to *fr* (Figure 3.11). However, the results are more sensitive when a much higher ice algal biomass and high in-ice irradiance are used. Simulated depth-integrated biomasses at the LSC site (using *fr* values of 0.85 and 0.99) varied by up to 10 mg-chl *a* m^{-2} away from the control run, when the biomass of the latter was raised to 160 mg-chl *a* m^{-2} by lowering the physical melt loss term (not shown).

3.5.2.3 Grazing on ice algae

In the model, the grazing rate is taken to be a constant fraction (*gr*=0.1) of the net ice algal growth rate (see section 3.3.2.5). However, Vézina et al. [1997] estimated that grazing by microheterotrophs (ciliates or nanoflagellates) could be as high as 15-20% of the net production in the late phase of the ice algal bloom. Grazing by larger animals might also increase in the later part of the bloom, due to enlargement of the brine channels that allows them to graze on ice algae that are still in the ice matrix [Krembs et al., 2000]. Results of the sensitivity of the model to *gr* (Figure 3.12) suggest that it could

have been the case here, as using a smaller grazing fraction in the first half of the bloom and a higher fraction in the later part of the bloom would improve the comparison with the observed biomass.

3.6. Conclusion

Using a coupled 1D model, we investigated the importance of different limiting factors and loss terms on ice algal biomass accumulation. The model results show that the snow cover, which controls the amount of light reaching the ice algae, is the principal factor controlling the duration of the ice algal bloom. The amount of PAR penetrating the snow cover determines both the initiation of the bloom as well as its decline, through a direct effect on the ice algal growth rate as well as through its effect on ice temperature and bottom ice melt rate. The ice algae are essentially light limited at the beginning of the bloom, proceed through a period where limitation fluctuates between light and nutrient, and end up being nutrient limited towards the end of the bloom when a melt water lens forms below the ice. Although these limitation factors control the ice algal growth rate, it appears that the level of biomass attained during the growth season depends heavily on losses resulting from physical melt loss, although biological melt loss can also be important at times when both in-ice PAR and ice algal biomass are high. The modulation of h_v by the fortnightly tides does induce fluctuations in nutrient supply and ice algal growth rate but its most important effect is on the heat transfer coefficient from the mixed layer to the bottom of the ice, and thus on the physical melt loss term. Tides do modulate the algal biomass but cause a second order variability superimposed on the seasonal cycle (Figure 3.10). The most notable fluctuation was caused by a rapid ice warming at the beginning of June. The model results support the hypothesis [e.g., Gradinger et al., 1991] that such events are caused by melting of the brine channel walls in conjunction with brine flushing, which results in ice algal loss to the water column and nutrient replenishment in the skeletal layer. They also give more weight to the hypothesis of Fortier et al. [2002] that early rain events and warm periods result in rapid loss of ice algae to the water column. The model showed that the ice algal decline is triggered by the initiation of snowmelt and thus by an increase in the bottom ice melt rate. However, the

speed of the decline can be affected by different factors. The most important are (i) the bottom ice melt rate, (ii) the ice warming rate, which determines the melt rate of the brine channel walls, and (iii) nutrient limitation resulting from the formation of a meltwater lens. The ice growth rate limitation factor determines the time of the year when ice algae completely disappear from the bottom of the ice. Combined measurements of bottom ice melt rate and ice algal biomass are required to determine the threshold ice melt rate.

From our results, it appears that interannual variations in bottom ice melt rate, resulting from changes in the thickness of the boundary layer at the ice-water interface, could account for the observed interannual differences in ice algal biomass in the Resolute area, when all other factors are of similar magnitude (see section 3.1). Also, the model results suggest that the warming and earlier snowmelt predicted by climate models would lead to a shorter annual ice algal bloom, and potentially to a decrease in the maximum ice algal biomass attainable due to an increase in ice algal melt loss.

3.7. Appendix: Changes made to the initial ice model

The changes made to the initial ice model of Mellor and Kantha [1989] are as follows:

- penetration and absorption of solar radiation by the ice have been incorporated and influence the ice temperature;
- the parameterization of the albedo was changed to that of Flato and Brown [1996], except for the melting snow albedo which was fixed at 0.70 and the C_{12} value in equation (12) of Flato and Brown [1996] which was modified to 0.16 m^{-2},
- the turbulent fluxes of sensible and latent heat are calculated after Andreas [1987];
- the incoming longwave radiation is calculated after Maykut and Church [1973];
- the thermal properties of sea ice are calculated separately for both layers of the model (properties are uniform in the initial model);
- the effect of brine volume on the transport of heat in sea ice is accounted for in the representation of the thermal conductivity and volumetric heat capacity of sea ice, which are calculated as in Flato and Brown [1996];
- the thermal conductivity of snow is calculated as in Ebert and Curry [1993];

- and the volume fraction of brine in the ice is calculated after Frankenstein and Garner [1967].

Variable	Definition	Estimated value	Unit
Sea ice model and mixed layer			
F_T	Oceanic heat flux	calculated	W m^{-2}
h_i	Ice thickness	calculated	m
h_v	Molecular sublayer thickness	calculated	m
K	Turbulent mixing coefficient	estimated	m^2 s^{-1}
κ_i	Ice attenuation coefficient	1.2	m^{-1}
κ_s	Snow attenuation coefficient	7.5 or 14.0	m^{-1}
L_i	Latent heat of fusion of sea ice	calculated	J kg^{-1}
M_t	Ice melt rate at the upper surface	calculated	m s^{-1}
M_b	Ice melt/accretion rate at the lower surface	calculated	m s^{-1}
ν	Kinematic viscosity of seawater	1.85×10^{-6}	$m^2 \cdot s^{-1}$
Q_{AI}	Heat flux at the ice-atmosphere interface	calculated	W m^{-2}
Q_{IO}	Conductive flux at the ice-ocean interface	calculated	W m^{-2}
Q_{I2}	Conductive flux at the ice-atmosphere interface	calculated	W m^{-2}
ρ_i	Reference ice density	917	Kg m^{-3}
SW	Shortwave radiation	calculated	W m^{-2}
T_a	Air temperature	input	°C
u_τ	Friction velocity	estimated	m s^{-1}
Ice algae model			
a^*	Mean chl *a*-specific attenuation coefficient	0.02	m^2 (mg-chl *a*)$^{-1}$
α^B	Photosynthetic efficiency	see Table 3.2	mg-C (mg-chl *a*)$^{-1}$ h^{-1} (μEinst m^{-2} s^{-1})$^{-1}$
B	Ice algal biomass	calculated	mg-chl *a* m^{-2}
D	Molecular diffusion coefficient of silicate	1×10^{-9}	m^2 s^{-1}
fr	Fraction of absorbed energy released as heat by algae	0.9	Dimensionless
F_{ia}	Energy released as heat by ice algae	calculated	W m^{-2}
F_N	Flux of nutrient to the top of the mixed layer	calculated	mmol m^{-2} s^{-1}
F_{Nskel}	Flux of nutrient to the skeletal layer	calculated	mmol m^{-2} s^{-1}
G	Grazing rate	calculated	d^{-1}
h_a	Ice algal layer thickness	0.02	M
K_s	Half-saturation constant for silicate uptake	4.0	mmol m^{-3}
κ_{chl}	Ice algal attenuation coefficient	calculated	m^{-1}
L_{lim}	Light limitation	calculated	Dimensionless
N	Concentration of nutrient in the surface water	input	mmol m^{-3}
$Nskel$	Concentration of nutrient in the ice algal layer	calculated	mmol m^{-3}
N_{lim}	Nutrient limitation	calculated	Dimensionless
μ	Ice algal specific growth rate	calculated	d^{-1}
μ_{max}	Maximum ice algal specific growth rate	calculated	d^{-1}
P_m^B	Maximum photosynthetic rate	see Table 3.2	mg-C (mg-chl *a*)$^{-1}$ h^{-1}

Table 3.1. Values and units for variables and parameters used and calculated by the model. The observations given as input to the model are described in section 3.2.

Site	α^B	P^B_m	I_k
LSC	0.03	0.3	10
PAR	0.055	0.285	5.2
HSC	0.12	0.27	2.3

Table 3.2. Ice algal photosynthetic parameters used in the ice algal growth model, for the three observation sites described in section 3.2. The parameters were chosen from in situ measurements and after Cota and Horne [1989] and Smith et al. [1988] for the same area. See Table 3.1 for units.

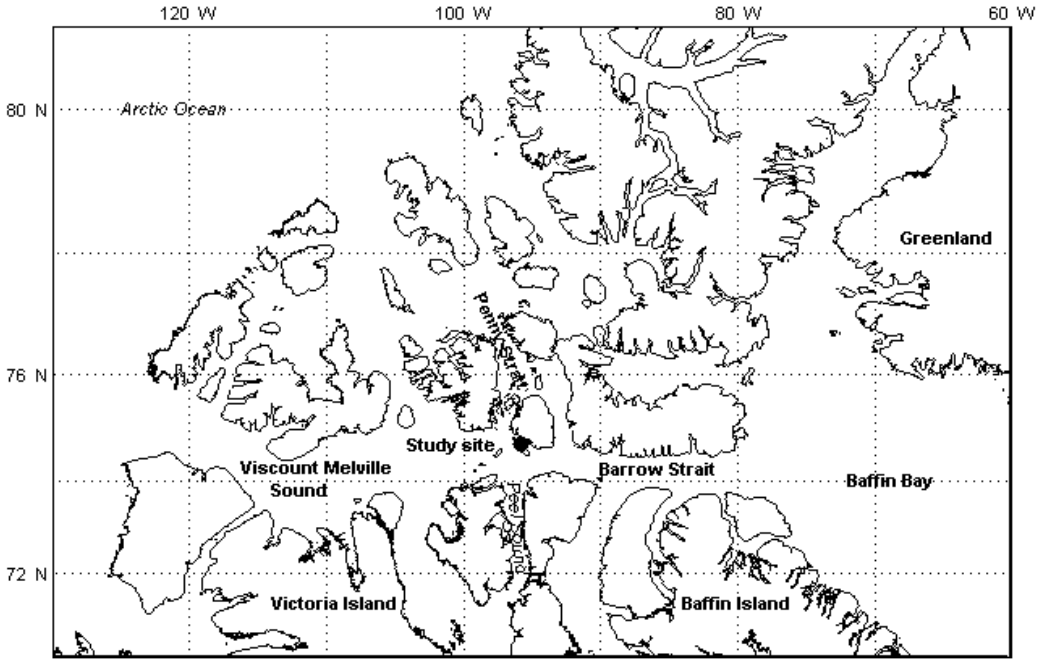

Figure 3.1. Location of study site (•), offshore Resolute in Barrow Strait.

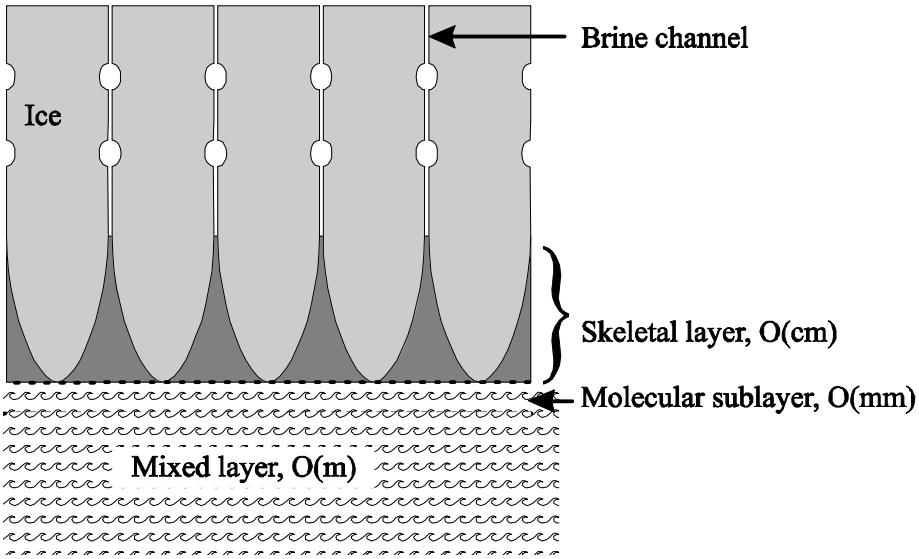

Figure 3.2. Schematic of the different layers at the base of the ice (light gray). Ice algae (dark gray) are found in the skeletal layer.

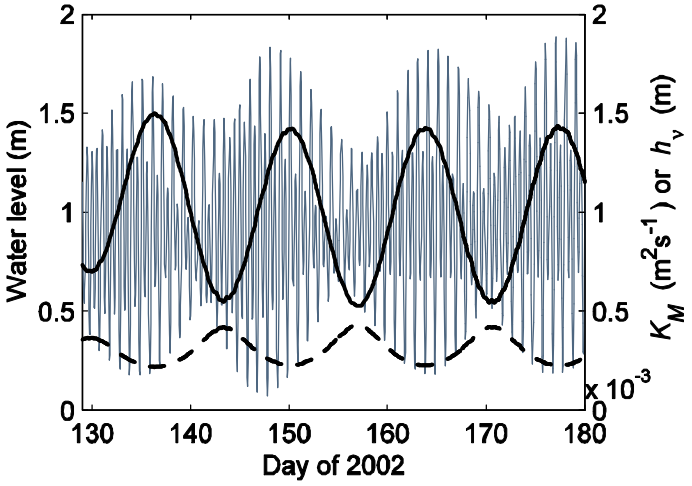

Figure 3.3. Predicted water level at Resolute (light gray, left scale), eddy diffusion coefficient (solid black line) and molecular sublayer thickness (dotted line) estimated over the study period.

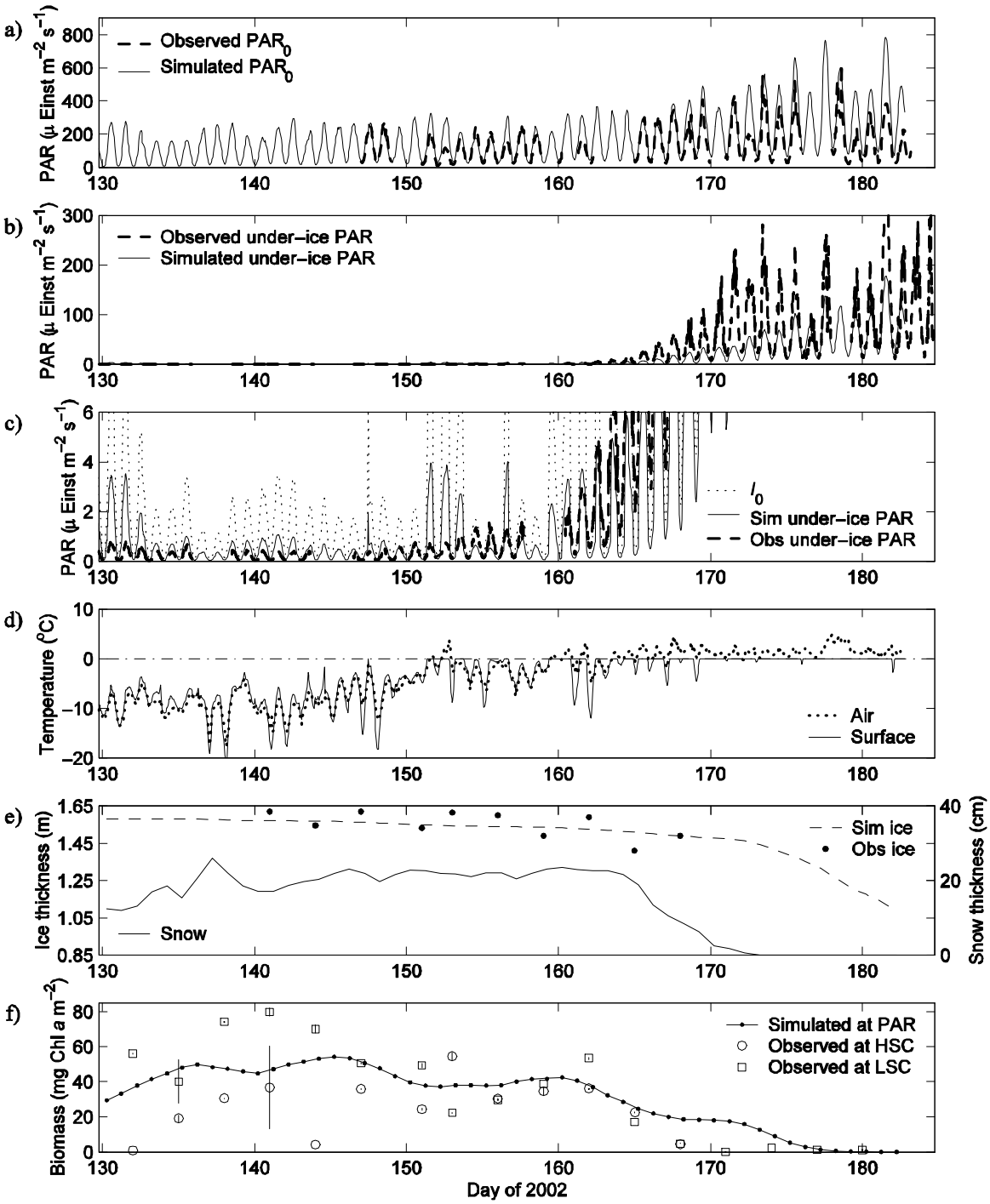

Figure 3.4. Time series of: (a) hourly-averaged observed and simulated PAR at the surface (after reflection), (b) observed and simulated under-ice PAR, (c) enlargement of (b) with PAR available on top of the ice algal layer (I_0), (d) hourly-averaged observed air temperature and simulated surface temperature, (e) observed snow thickness (–) and simulated ice thickness (--) at the PAR site and ice thickness observed at the HSC site (·), and (f) simulated chl *a* biomass at the PAR site and observed biomass at the LSC and HSC sites (the vertical bars represent standard deviation over three ice cores).

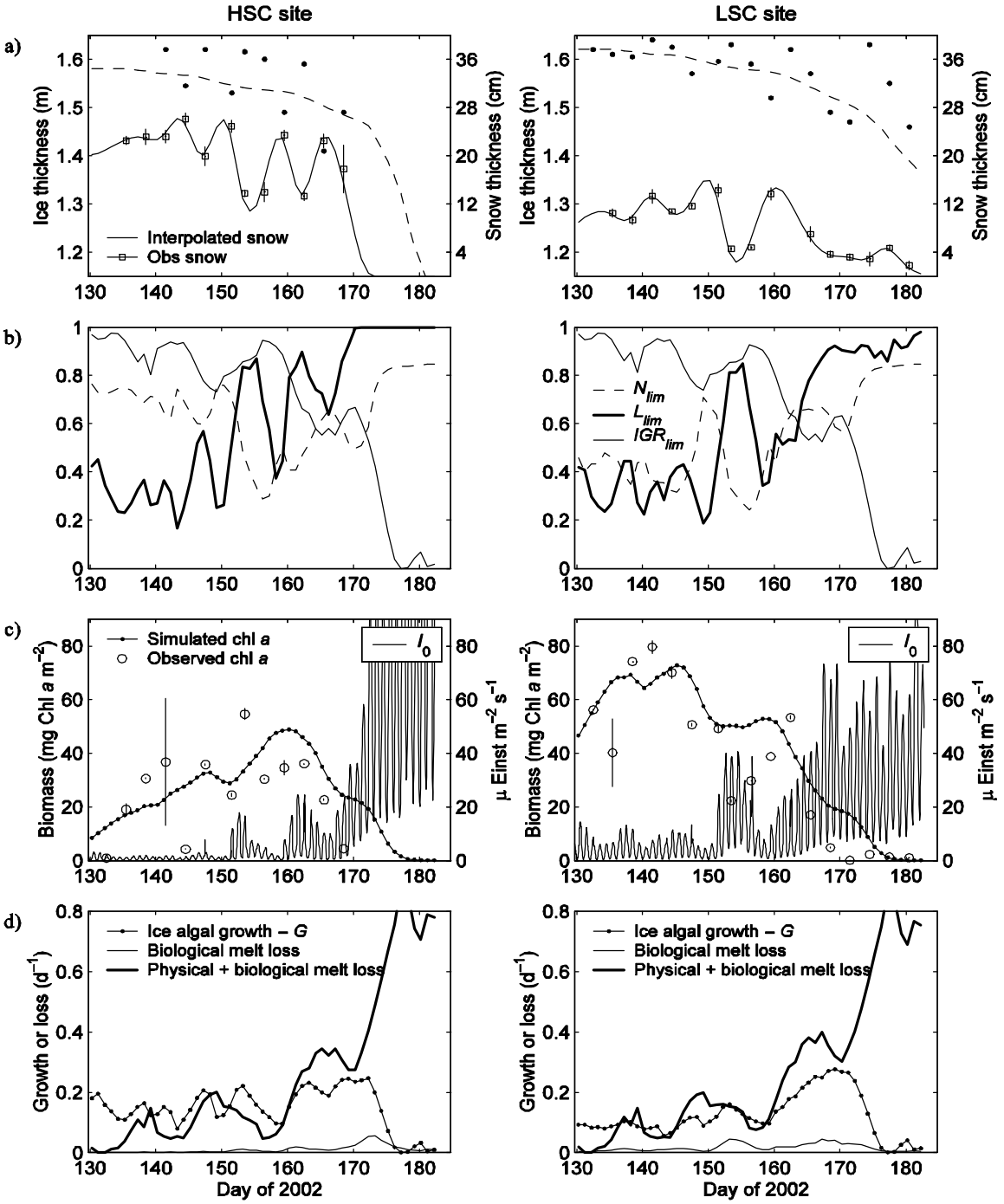

Figure 3.5. Model results versus observations for the two sampling sites: (a) Observed snow and observed (·) and simulated (--) ice thicknesses; (b) daily mean of nutrient (-- N_{lim}), light (— L_{lim}) and ice growth rate (− IGR_{lim}) limitation functions; (c) observed (○) and simulated daily mean bottom ice chl *a* biomasses, and modelled PAR at the top of the ice algal layer (I_0); and (d) daily mean of gain (growth minus grazing) and loss (physical and biological melt loss) of biomass. The vertical bars on snow thickness and ice algal biomass observations represent the standard deviation over three ice cores.

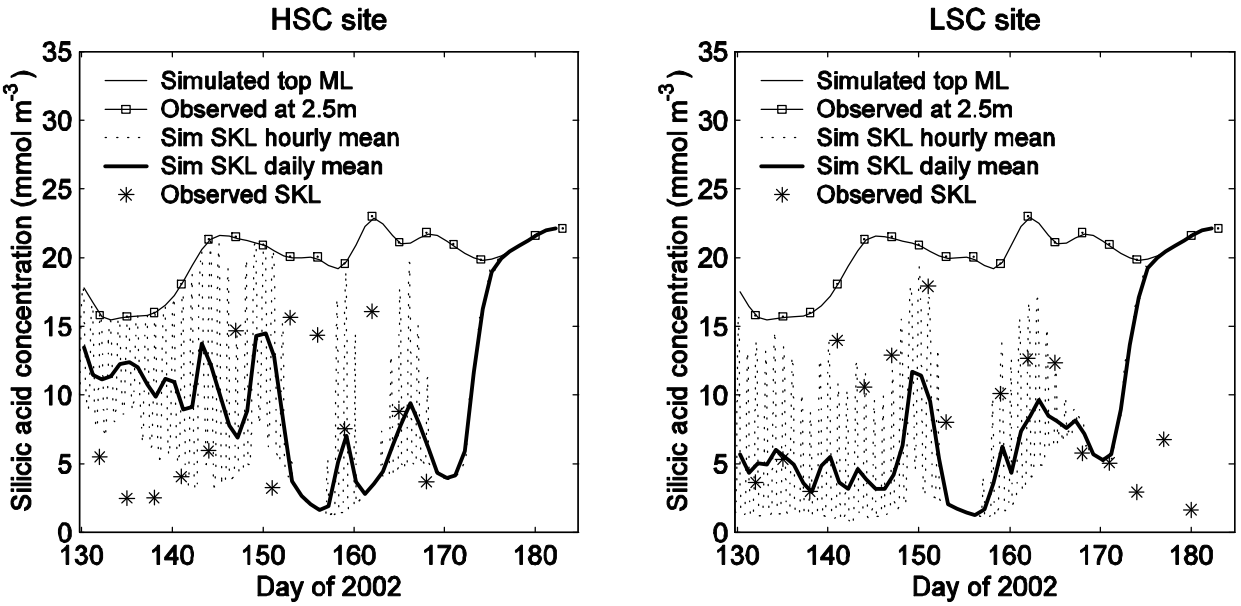

Figure 3.6. Observed and simulated silicic acid concentrations at the top of the oceanic mixed layer (simulated at 0.5 m and observed at 2.5 m), and in the skeletal layer (SKL) at the two sites.

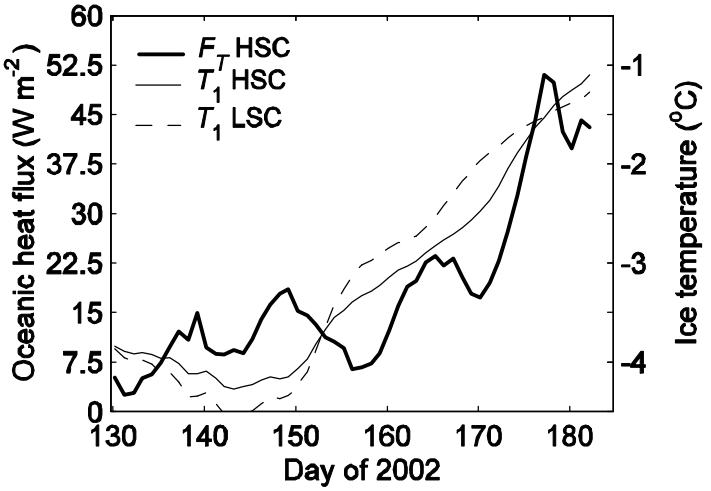

Figure 3.7. Daily mean of oceanic heat flux to the underside of the ice (F_T), and simulated internal ice temperature (T_1) at the two sites.

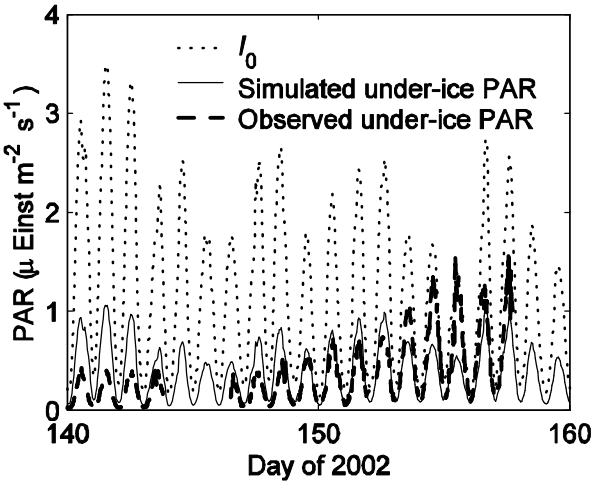

Figure 3.8. Time series of observed and simulated under-ice PAR, and PAR available at the top of the ice algal layer (I_0), for a constant snow attenuation coefficient of 14.0 m^{-1}.

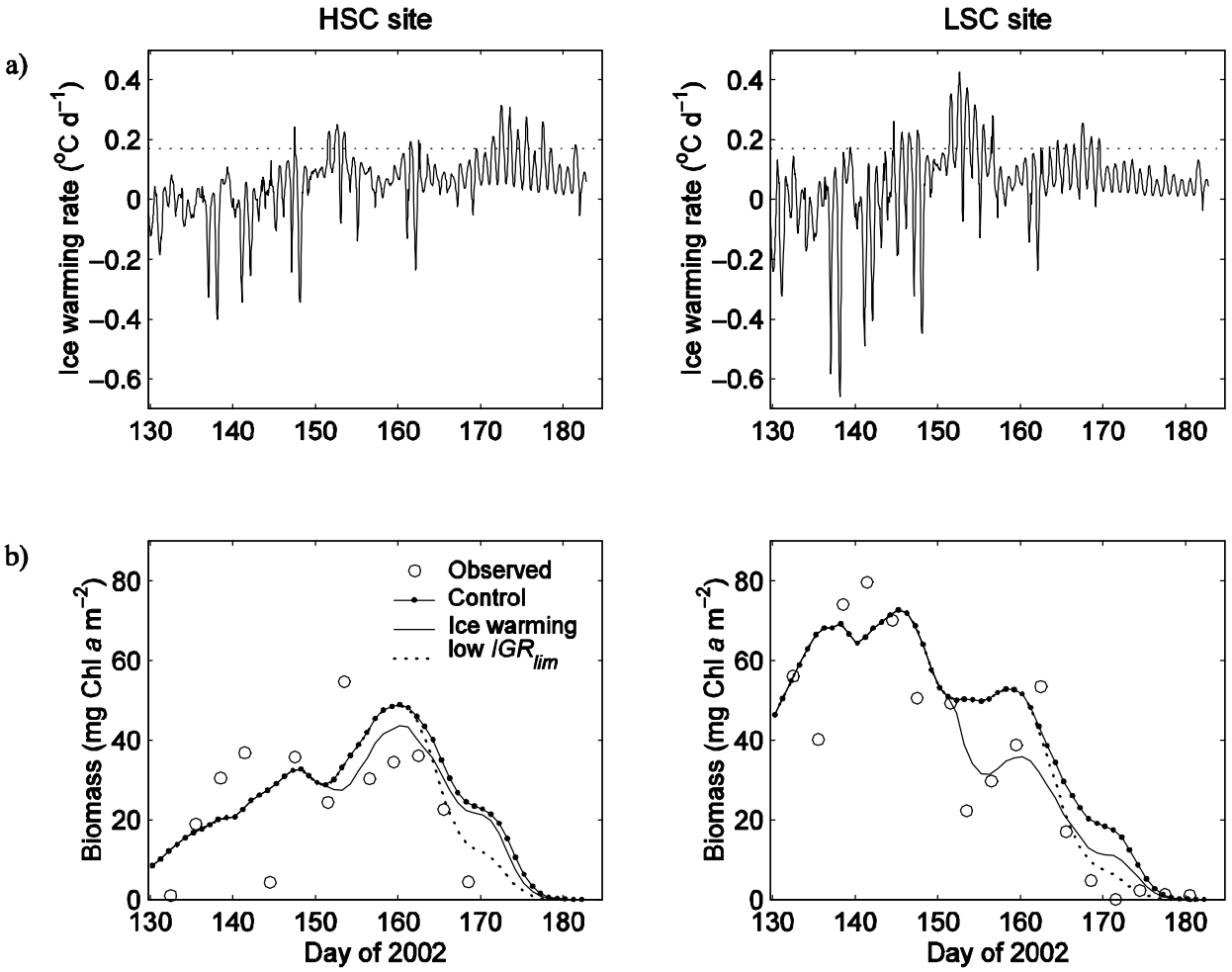

Figure 3.9. (a) Rate of change in internal ice temperature (the dashed line indicates the temperature above which the loss term is effective), and (b) observed (○) and simulated daily mean chl *a* biomasses at the two sites: the control simulation (same as in Figure 3.5) is compared with the biomasses obtained when including the ice warming rate dependent loss term (–), and when using a lower IGR_{lim} (more limiting), calculated with a threshold ice melt rate of 0.85 cm d^{-1} (…).

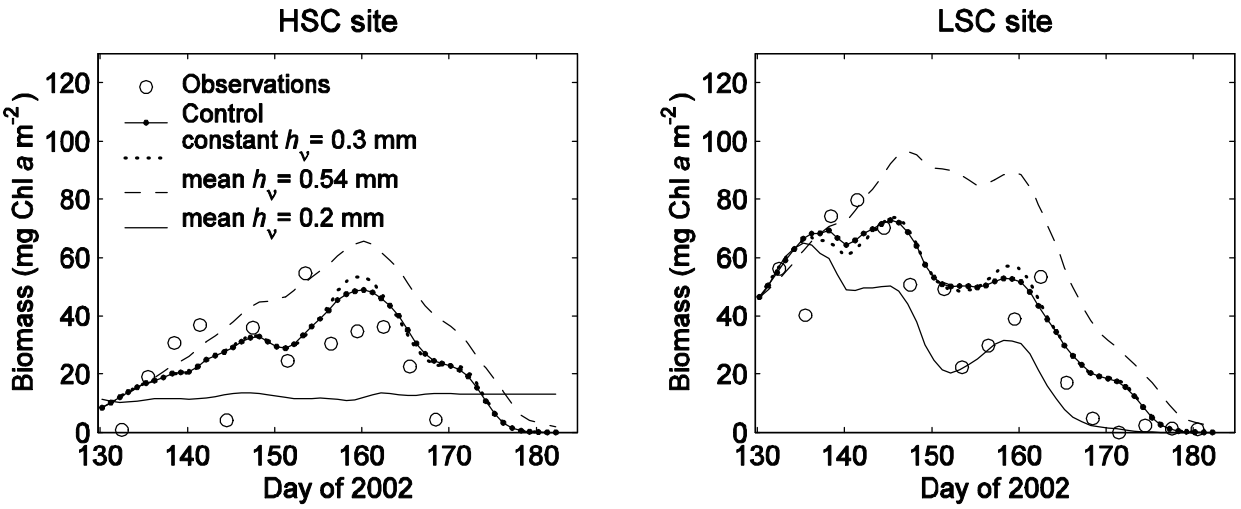

Figure 3.10. Observed (○) and simulated daily mean chl *a* biomasses at the two sites. The control simulation (same as in Figure 3.5) is compared with simulations obtained using a constant (no tidal fluctuations) h_v of 0.3 mm (…), and using lower and higher friction velocities with corresponding mean h_v of 0.54 mm (--) and 0.2 mm (–).

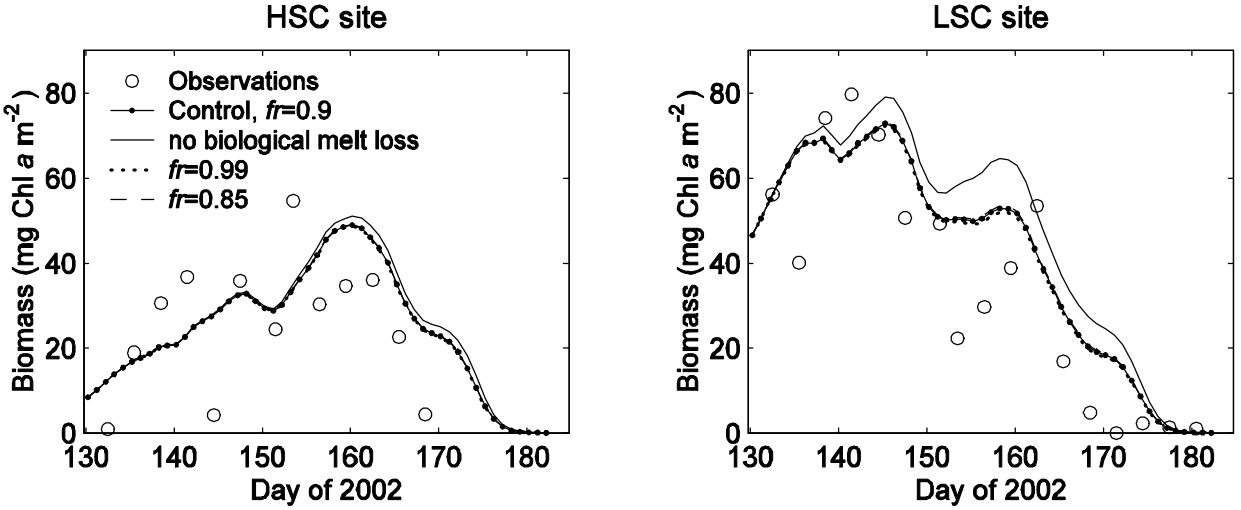

Figure 3.11. Observed (○) and simulated daily mean chl *a* biomasses at the two sites. The control simulation (same as in Figure 3.5, *fr*=0.90) is compared with the biomasses obtained when removing the biological melt loss term from eq. (3.24) (–), and using different fraction of heat release by the ice algae (*fr*): 0.99 (…) and 0.85 (--).

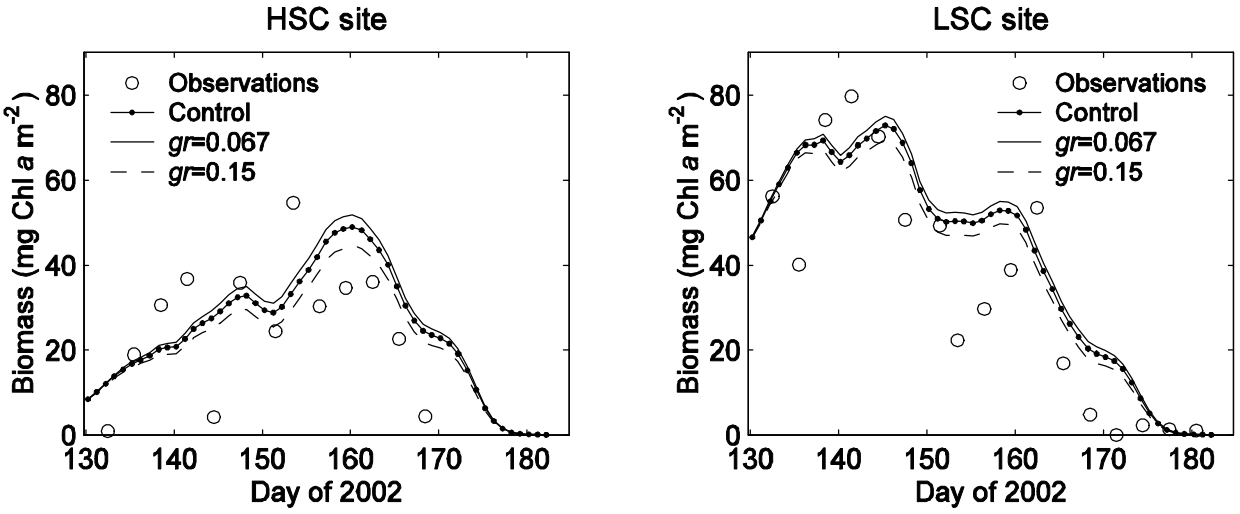

Figure 3.12. Observed (○) and simulated daily mean chl *a* biomasses at the two sites. The control simulation (*gr*=0.1) is compared with the biomasses obtained using different grazing fraction *gr* (see section 3.3.2.5): 0.067 (–) and 0.15 (--).

4. Primary productivity and export fluxes on the Canadian shelf of the Beaufort Sea: a modelling study

4.1. Introduction

Sea ice exerts an important control for primary production on Arctic shelves: by providing a substrate for algal growth at the bottom of the ice, by limiting the availability of solar irradiance to primary producers, by limiting the development of thermal or freshwater stratification in the freezing season (while enhancing it during the thawing season), and by alternatively promoting or suppressing diapycnal mixing and shelf-break upwelling [Carmack et al., 2004; Williams et al., 2006]. The distribution of sea ice cover varies strongly on interannual [e.g., Macdonald et al., 1987; O'Brien et al., 2006], decadal and multi-decadal [Polyakov and Johnson, 2000; Polyakov et al., 2002] scales. An appreciable reduction in perennial ice cover has recently been observed [Comiso and Parkinson, 2004; Stroeve et al., 2007] and even greater changes are predicted as a consequence of global warming [Anisimov et al., 2001; Johannessen et al., 2004; ACIA, 2005]. The decline in sea ice extent and thickness is expected to promote increased primary production [e.g., Gradinger, 1995; Loeng et al., 2005]. This increase in primary production would result not so much from an increase in light availability but rather from an increased nutrient supply through wind mixing and shelf-break upwelling [Carmack et al., 2004; Loeng et al., 2005]. As primary production supports the entire food chain, it is crucial to understand how changes in Arctic shelf ice climate will affect that primary production. Data appropriate to determining ice – primary production interactions in the Arctic are practically non-existent because of logistical constraints imposed by harsh environmental conditions especially during the time period preceding and extending through sea ice break-up. Traditionally, fieldwork has been conducted in spring, prior to break-up, or in summer, when ships are capable of access, resulting in large spatial and temporal gaps. These constraints limit our understanding of the processes and their relative importance in controlling primary productivity. Numerical models provide a means to fill in the temporal and spatial sampling gaps and to evaluate the importance of specific processes.

A few coupled physical-biological models have been applied in Arctic waters, for example in the Bering and Chukchi Seas [Shuert and Walsh, 1993; Walsh and Dieterle, 1994; Walsh et al., 2004] and in the Greenland and Barents Seas [Wassmann and Slagstad, 1993; Slagstad et al., 1999]. However, these models were not coupled to a sea ice model, and they either spanned only the ice-free period or the ice thickness was entered as a forcing of light availability. Finally, none of these models simulates ice algal production. Here, we present a coupled 1D model (snow, ice, ocean, ice algae, phytoplankton, zooplankton, and detritus) to estimate the annual cycle and total annual primary production on the Canadian Beaufort Sea shelf in 1987, a year when there was intensive sampling. Our overall objective is to examine the relative importance of various physical processes (i.e. snow and sea ice thickness, sea ice melt, freshwater runoff, and water column stratification and mixing) in controlling the timing and magnitude of primary production and biogenic particle export. Despite the limitations of 1D models, it is prudent to first determine in a 1D context the major sensitivities in coupling physical and biogeochemical processes in a dynamic model of a seasonally ice-covered region of the ocean before proceeding to a 3D implementation.

4.2. Study area

The Mackenzie Shelf in the Beaufort Sea, defined by the 200-m isobath, has a width of about 100-150 km [Figure 4.1; e.g., Macdonald et al., 1987]. It is the most estuarine of the Arctic shelves, with the Mackenzie River having an annual discharge of 3.3×10^{11} m^3 yr^{-1} [Macdonald et al., 2000]. Freeze-up usually starts in mid-October while break-up commences in early June. During winter, ice cover is organized outwards from the shore in a landfast zone extending to about the 20m isobath, which is comprised of level seasonal ice interspersed with zones of rubbled ice (called stamukhi), a flaw lead zone (intermittently open water), and finally by drifting pack ice composed of first- and multi-year ice (see Figure 4.2) [Carmack and Macdonald, 2002; Carmack et al., 2004]. Stamukhi act as a partial barrier to outflow from the Mackenzie River leading to the formation of a large pool of fresh or brackish water shoreward of the stamukhi zone at the

end of winter. The flaw lead separates the inner shelf from the outer shelf (Figures 4.1 and 4.2). After ice break-up, the freshwater discharge either flows eastward alongshore towards Amundsen Gulf [Macdonald et al., 1987], or extends off shelf and into the interior of the ocean [Macdonald et al., 1999, 2002; O'Brien et al., 2006]. The partitioning of the shelf into a zone strongly influenced by Mackenzie River inflow and a zone dominated by marine waters exerts a fundamental control on plankton communities [Parsons et al., 1988, 1989].

To avoid the physical and geochemical heterogeneity of the nearshore zone (stamukhi, river influence, heterotrophic food chain), we have chosen to implement the model in the outer shelf region, just offshore of station #9 (see Figures 4.1 and 4.2). The convection in winter over the outer shelf, which produces a mixed layer of ~30-50m, is generally not deep enough to penetrate into and entrain nutrient-rich mode water of Pacific origin (~75-250m) [Macdonald et al., 1989], with the consequence that surface nutrient concentrations remain relatively low throughout the year [e.g., Carmack et al., 2004].

The circulation over the shelf is highly variable with mean current speeds generally small relative to the fluctuating field [Melling, 1993]. However, there is a general eastward movement of water on the shelf, a surface westward movement off shelf (Beaufort Gyre), and a subsurface eastward current at the shelf break that opposes surface flow [Aagaard, 1984]. See Carmack and Macdonald [2002] for more detail on the oceanography of the region.

4.3. Model description

We developed and coupled a pelagic submodel to the sea ice – ice algae model developed in Chapter 3. Below, we describe the biological model as well as the changes that were made to the mixed layer model and to its coupling with the sea ice model. Variables and parameters for the biological model are given in Table 4.1.

4.3.1 The ocean model

We represent the upper ocean with the turbulence closure (level 2.5 version) model of Mellor and Yamada [1974, 1982]. The model domain is 120 m deep, with 22 layers of variable thickness (two layers of 1 m near the top and bottom boundaries, followed by one layer of 2 m and 4 m, with 13 layers of 8 meters in between). The turbulent mixing coefficients (K_M and K_H) are calculated at all depths each time step. Tidal currents on the Mackenzie shelf are generally weak and are neglected in the model equations since they do not represent a major source of mixing energy [Kulikov et al., 2004; Carmack and Macdonald, 2002]. Winds provide mixing energy during ice-free periods and the movement of the sea-ice cover on the ocean and brine-driven convection provide mixing energy in winter.

We added an additional term to the water temperature equation (last term of eq. 4.1) to account for the warming resulting from the absorption of shortwave radiation in the ocean. The water temperature (T) at depth z changes according to

$$\frac{\partial T}{\partial t} = \frac{\partial}{\partial z}\left[\left(K_H + b\right)\frac{\partial T}{\partial z}\right] + \frac{1}{\left(rc_p\right)_w}\frac{\partial PAR}{\partial z} \qquad (4.1)$$

where t is the time, z is the depth within the mixed layer, β is a background diffusion ($1\text{x}10^{-5}$ m^2 s^{-1}), $(\rho c_p)_w$ is the volumetric heat capacity of water and PAR is the visible radiation that penetrates the surface of the ocean. When ice cover is present, PAR immediately below the surface microlayer of the ocean ($PAR(0)$) is a function of cloudiness, snow and ice type and thickness, and ice algal concentration (see section 2.1, page 16); when the ocean is ice free, $PAR(0)$ is equal to $0.45(1-\alpha_w)SW$ (α_w is the water albedo and SW is the total solar radiation). PAR is attenuated throughout the water column by the water itself and by both phytoplankton and detritus for a total attenuation coefficient (κ_t) of:

$$\kappa_t = \kappa_w + a_p Phy + a_d(D_s + D_f + D_{ia}) \qquad (4.2)$$

where κ_w is the attenuation coefficient of pure seawater, a_p and a_d are the specific attenuation coefficients for phytoplankton and detritus respectively, *Phy* is the phytoplankton biomass, and D_s, D_f and D_{ia} are the concentrations of slow-sinking, fast-sinking and ice algal detritus.

The domain of the present model extends well below the halocline at the bottom of the polar mixed layer (~50 m). A parameterization of this halocline and of the water mass below, which vary little over time [e.g., Macdonald et al., 1988a; Carmack et al., 1989], was therefore prescribed by relaxing the temperature and salinity over the bottom 70 m to the initial profile with a relaxation timescale of 3 days.

4.3.2 Ocean/sea ice interfacial fluxes

The ocean and sea ice are coupled through the exchange of heat and salt through a thin control volume [Mellor et al., 1986]. The turbulent fluxes of heat and salt are assumed proportional to the gradients of temperature and salinity respectively. The interfacial stress and heat flux are calculated as in Mellor and Kantha [1989], except for the roughness length (z_0) which is smaller. We determine z_0 as $0.07h_i$, where h_i is the ice thickness. We also modified the salt flux (F_S) across the ocean interface

$$F_S = (W_O - W_{RO})(S_I - S_0) + S_0R \qquad (4.3)$$

where W_O represents the vertical speed of the ice/ocean interface resulting from accretion and ablation at the base of the ice, W_{RO} is the "percolation" speed of the surface melt water which migrates through the ice/ocean interface (equal to the melt rate at the snow/ice-atmosphere interface), S_I and S_0 are the ice and interface salinities. The ice salinity is calculated in a way similar to Ebert and Curry (1993) to account for the higher salinity of newly formed ice but with a minimum salinity of 4.5. The last term in eq. (4.3) was added to account for the influence of freshwater inflow from lateral advective processes, following Holland et al. [1997]. We calculated a variable value for R that

follows the Mackenzie River's freshwater runoff curve for 1987 [e.g., see Carmack et al., 2004], but with a lag of one month [O'Brien et al., 2006] to account for travel time between the hydrology observation site (Red River) and our modelling site, and with annual average and maximum values for R of 0.067 and 0.17 g m^{-2} s^{-1} respectively.

4.3.3 Coupling between the atmosphere and the ocean

When the ocean is free of ice, mixing energy is provided to the mixed layer through the wind stress ($\vec{t}$),

$$\vec{t} = C_D r_a \vec{V}_{wg} \left| V_{wg} \right| \qquad (4.4)$$

where ρ_a is the surface atmospheric density and C_D, the drag coefficient, varies with the wind speed (V_{wg}) according to Large and Pond [1981]. The dimensionless heat transfer coefficients for the calculation of the turbulent fluxes of sensible and latent heat (C_E and C_H) are constant in the ice-free case (1.2×10^{-3} and 1.0×10^{-3} respectively, from Smith [1988]).

The salt flux (F_S) into the ice-free ocean differs from Mellor and Kantha [1989]. As in Omstedt et al. [1994], we neglect the evaporation/precipitation term and, as for ice covered conditions, added the effect of freshwater inflow from lateral advection (R). The salt flux is thus equal to

$$F_S = S_0 R \qquad (4.5).$$

4.3.4 The biological model

The biological model consists of nine compartments (state variables) shown schematically in Figure 4.3: dissolved inorganic nitrogen (N), silicate (Si), phosphate (P), ice algae (Ia), phytoplankton (Phy), zooplankton (Z), fast-sinking detritus (D_f), slow-sinking detritus (D_s) and ice algal detritus (D_{ia}). The basic unit in the model is

mmol-N m^{-3}. Conversion to carbon (C), chlorophyll *a* (chl *a*), Si and P is needed for comparison with observations. We use fixed Redfield ratios [Redfield et al., 1963] for conversion between C, N and P (C:N:P = 106:16:1). For conversion of N to chl *a*, we use N:chl *a* (wt:wt) of 8.75:1 (calculated from the C:chl *a* given below) for phytoplankton and 5:1 for ice algae [Cota et al., 1987]. Ice algae grow at low light conditions and thus produce more chl *a* for light harvesting, explaining the lower N:chl *a* ratio for ice algae. The N:chl *a* ratios correspond to C:chl *a* (wt:wt) ratios of 50:1 for phytoplankton [e.g., Sakshaug and Slagstad, 1991; Wheeler et al., 1996] and 28:1 for ice algae. The Si:N (mol:mol), taken as 1.7 from measurements of N:Chl *a* ratio of 5 [Cota et al., 1987] and Si:Chl *a* ratio of 17 (see Chapter 3) in the Canadian Archipelago, is the same for ice algae and phytoplankton. We have not included dissolved organic matter (DOM) in the model explicitly because of the scarcity of data from the study area, especially on the lability (i.e. turnover time) of different fractions of DOM. The flows from zooplankton to *N* and *P* (Figure 4.3) can be considered to represent implicitly the excretion and transformation to dissolved inorganic matter of the most labile fraction of DOM.

4.3.4.1 Ice algae

The ice algal growth model is described in detail in section 3.3.2 (page 49). Ice algae use nutrients from the upper mixed layer. Ice algae are assumed to be limited by silicic acid; the other macro-nutrients are taken up by the ice algae according to the following ratio N:Si:P 16:27.2:1, based on the ratios described in the previous section. When melting occurs at the bottom of the ice, ice algal cells are expelled from the ice into the mixed layer at a rate proportional to the ice melt rate. A fraction of these cells can contribute to phytoplankton seeding but for the control run, all the cells are converted into detritus (D_{ia}).

4.3.4.2 Phytoplankton

Phytoplankton in the water column are modelled as diatoms, which dominate the plankton community at the modelling site [Parsons et al., 1988; Hsiao et al., 1977]. The rate of change in phytoplankton biomass is calculated as

$$\frac{\partial Phy}{\partial t} = Phy\left[m - M_{Phy} - S_{Phy}\right] + (1 - fad)Ia - G_{Phy}Z \qquad (4.6)$$

where μ is the specific phytoplankton growth rate, M_{Phy} is the specific mortality rate of phytoplankton, G_{Phy} is the specific loss rate of phytoplankton by grazing, and S_{Phy}, calculated after Wassmann and Slagstad [1993], represents loss of diatoms through sedimentation of resting spores and aggregates. The phytoplankton losses from mortality and sedimentation are converted to slow- and fast-sinking detritus respectively [Slagstad et al., 1999]. The second term on the right-hand side of eq. (4.6) represents seeding of phytoplankton by ice algal cells sloughed into the water column where *fad* is the fraction of sloughed ice algal cells that is converted directly to detritus.

Phytoplankton growth depends on light, nutrients and temperature. Assuming that the phytoplankton growth is limited by one factor at a time, the specific phytoplankton growth rate is

$$m = m_{\max} \min\left[\frac{N_i}{Ks_i + N_i}, (1 - \exp\left(\frac{-a^B PAR}{P_m^B}\right)\exp\left(\frac{bPAR}{P_m^B}\right)\right] \qquad (4.7)$$

The first term in brackets accounts for nutrient limitation represented by the Michaelis-Menten (monod) function, while the second term accounts for limitation by light represented by the exponential function of Platt et al. [1980]. $m_{\max}$ is the maximum temperature-dependent phytoplankton growth rate (predicted from the relationship of Eppley [1972]: $0.8511e^{(0.064T)}$ converted to $\log_e$), N_i (i = 1, 2, or 3) is the concentration of the three nutrients: nitrogen, silicic acid and phosphate, Ks_i (i = 1, 2, or 3) is the half-saturation constant for each nutrient, a^B is the photosynthetic efficiency, $P^B{}_m$ is the maximum (light-saturated) photosynthetic rate of diatoms, and β is a photoinhibition coefficient. All functions return a value between 0 and 1, and the most limiting factor (lowest value) is used to calculate the specific growth rate. Growth occurs only for *PAR* greater than the compensation intensity, fixed at 0.3 W m^{-2} after Subba Rao and Platt [1984].

4.3.4.3 Nutrient concentration

The rate of change of nutrient concentration in the mixed layer is equal to

$$\frac{\partial N_i}{\partial t} = g_{Ds} D_s + g_{Df} (D_f + D_{ia}) + E_{zn} Z - mPhy \qquad (4.8)$$

where γ is the remineralization rate of detritus to nitrogen and phosphate, or the dissolution rate in the case of Si (N_2) and E_{zn} is the excretion rate of zooplankton. The slow- and fast-sinking detritus remineralize to N and P at different rates, but dissolve to Si at the same rate (see section 4.3.4.5). The term $E_{zn}Z$ does not appear in the calculation of Si concentration. The last term on the right-hand side of eq. (4.8) represents the uptake rate of nutrient by phytoplankton. Nutrients are restored to their initial value in the halocline (at 60 m) and over the bottom 3 levels with a timescale of 3 days.

4.3.4.4 Zooplankton

Zooplankton are modelled as large copepods (>2 mm), which dominate the biomass of the mesozooplankton community in the modelling site area [Parsons et al., 1988, 1989; Forbes et al., 1992]. The rate of change in zooplankton biomass is calculated as follows,

$$\frac{\partial Z}{\partial t} = Z[g_a G - E_{zn} - M_z] \qquad (4.9)$$

where g_a is the assimilation efficiency, G is the specific grazing rate on phytoplankton and detritus, and M_z is the zooplankton rate of mortality. Grazing is represented by a standard quadratic dependence on prey (Holling-type-III) [Denman and Peña, 1999]

$$G = r_m \frac{food^2}{K_p^2 + food^2} = G_{Phy} + G_{Df} + G_{Dia} \qquad (4.10)$$

where r_m is the maximum grazing rate, and K_p is the half-saturation constant for grazing. Grazing on phytoplankton, detritus and ice algae is partitioned as follows:

$$food = Phy + fd_1 D_f + fd_2 D_{ia} \quad (4.11)$$

where fd_i can be considered as either the fraction of detritus/ice algae used as food or the preference for detritus/ice algae relative to a preference of 1 for phytoplankton. Loss terms for phytoplankton and zooplankton are set to zero when their biomasses drop to their initial January conditions 0.02 and 0.03 mmol-N m^{-3} (respectively), to maintain nonzero populations during dark periods.

4.3.4.5 Detritus

Detritus is divided into three compartments: slow-sinking (D_s), fast-sinking (D_f) and ice algae (D_{ia}). The slow-sinking component is made up of dead phytoplankton cells while the fast-sinking component encompasses faecal pellets, dead zooplankton bodies and sedimenting phytoplankton cells. The fraction of ice algal cells expelled from the ice during ice melt that is not used for phytoplankton seeding (*fad*) goes to ice algal detritus. The fast-sinking and ice algal particles have a sinking rate (w_f) of 50 m d^{-1} and a degradation rate (γ_{Df}) of 0.33 d^{-1}, while the slow-sinking component has a sinking rate (w_s) of 1 m d^{-1} and a degradation rate (γ_{Ds}) of 0.05 d^{-1}. These rates were taken from Slagstad et al. [1999]. The dissolution rate of detrital Si is the same for the three compartments (0.03 d^{-1}). The concentration of slow-sinking, fast-sinking and ice algal detritus changes according to equations (4.12) to (4.14) respectively.

$$\frac{\partial D_s}{\partial t} = M_{Phy} Phy - g_{Ds} D_s - w_s \frac{\partial D_s}{\partial z} \quad (4.12)$$

The first term on the right hand side of eq. (4.12) is the detritus supplied by phytoplankton mortality, the second term is remineralization of detritus to nutrient, and the last term represents sinking of detritus.

$$\frac{\partial D_f}{\partial t} = S_{Phy} Phy + (1 - ga)GZ + M_Z Z - g_{Df} D_f - G_{Df} Z - w_f \frac{\partial D_f}{\partial z} \quad (4.13)$$

The first term on the right-hand side of eq. (4.13) is the supply of detritus from sedimenting phytoplankton cells, the second term is fecal pellet production by copepods, the third term is mortality of copepods, the fourth term is remineralization of fast-sinking detritus to nutrient, the fifth term is grazing of fast-sinking detritus by copepods, and the last term represents sinking of detritus. The terms relating to zooplankton are removed from eq. (4.13) in the calculation of the Si detritus concentration and (1-*ga*)*GZ* is replaced with $G_{Phy}Z$ since fecal pellet production of silicate is equal to grazing on diatoms (silicate is passed directly from phytoplankton to the Si detritus pool through zooplankton [Chai et al., 2002]).

$$\frac{\partial D_{ia}}{\partial t} = fad\ Ia - g_{Df} D_{ia} - G_{Dia} Z - w_f \frac{\partial D_{ia}}{\partial z} \quad (4.14)$$

The first term on the right-hand side of eq. (4.14) is the supply of detritus from the ice algae, while the third term is grazing by copepods. The term relating to zooplankton is removed from the equation in the calculation of the Si detritus concentration.

4.3.5 Forcing and initial conditions

Forcing data for the model (wind speed (Figure 4.4a), air temperature (Figure 4.4b), cloud fraction, relative humidity, and snow thickness for 1987 at Tuktoyaktuk Airport) were obtained from Environment Canada (see Figure 4.1). The modelling site is located between stations 9 and 10, closer to station 9. We thus chose an initial ice thickness (0.75 m) that led to a simulated ice thickness close to that observed at station 9. Initial profiles of water column temperature and salinity were constructed from CTD data collected at stations 9 and 10 (Figure 4.1) on April 1 and 3, 1987 [Macdonald et al., 1988a]. The model was first run for one year using the April *T* and *S* profiles as initial conditions in January, and the simulated salinity profile obtained at the end of December was then used to adjust the initial *S* profile (the mixed layer salinity was reduced by about 0.5). The

freezing temperature (-0.055*S*) was calculated using this new salinity, and the departure from freezing temperature calculated with the initial *T* and *S* profiles was added to the calculated temperature. Similarly, initial nutrient profiles were constructed with Go-Flo bottle data collected in the same area and on the same dates [Macdonald et al., 1988b], and adjusted to obtain good agreement between the simulated and observed concentration at the beginning of April. The other biological scalars have initial concentrations that are homogeneous over the water column: 0.02 mmol-N m^{-3} for phytoplankton, 0.03 mmol-N m^{-3} for zooplankton and 0 mmol-N m^{-3} for detritus. The initial concentration of nutrients in the skeletal layer (at the bottom of the ice) is equal to the nutrient concentration at the top of the mixed layer and the initial concentration for ice algae is equal to 0.5 mg-chl *a* m^{-2}.

4.4. Results

In this section, we present model results and compare them with observations made in 1987 [Macdonald et al., 1988a, b, c; Carmack et al., 1989; Carmack et al., 2004; O'Brien et al., 2006]. The model was run for three years to ensure that there was no drift in the mixed layer temperature, salinity and nutrient concentrations.

4.4.1 Temporal evolution of the physical system

Simulated surface temperature is close to the observed (at ~2 m) air temperature (Figure 4.4b) except during June, when the solar energy reaching the surface (Figure 4.4c) is taken up as latent heat (melting ice) rather than sensible heat (warming), and during the autumn, when convection prevents rapid cooling of surface waters. The simulated ice starts to melt at the beginning of June when the snow cover disappears (Figure 4.4d), and has completely melted by the first week of July.

Warming of the surface mixed layer (Figure 4.5a) commences immediately following the rapid freshening of the surface of the mixed layer by melting ice (Figure 4.5b). The warming progresses rapidly once the ice cover disappears (Figures 4.4b and 4.5a). The simulated warming and freshening of the surface layer deepen progressively, until strong

winds towards the end of August erode the stratification and mix the water column down to a depth of about 50 m (Figures 4.4a and 4.5a, b). By the end of September, solar radiation is low (Figure 4.4c) and the air temperature has dipped below 0ºC (Figure 4.4b). The surface of the mixed layer cools progressively (Figure 4.5a), until its temperature reaches the freezing point around mid-October, leading to ice formation (Figure 4.4d). Significant cooling occurs only in the top few meters of the ocean. The subsurface is still warm, and brine rejection occurring during ice formation leads to convection down to about 32 m, which brings warm water up to the ice underside (not shown). This warm water and the rapid thickening of the snow cover, which insulates the ice from the cold air, lead to melting of the newly-grown ice in early November (Figure 4.4d). Within a few weeks, enough heat has been extracted from the mixed layer for ice to form again (Figures 4.5a and 4.4d).

Panels c to h of Figure 4.5 compare simulated and observed profiles of temperature (panels c, d, e) and salinity (panels f, g, h). The simulated profiles compare well with observed temperature and salinity profiles until the beginning of August (Figure 4.5d and g). The simulated salinity profile continues to compare well with observations on September 1 (Figure 4.5h), but the model produces a mixed layer temperature that is ~ 2°C too high (Figure 4.5e). In the model, the excessive heat content of the mixed layer in late summer contributes to the melting of the ice following convection in November (Figure 4.4d). On the other hand, significant changes in the observed T and S profiles between September 1 and 2 (Figure 4.5e and h) indicate a change in water mass (e.g., passage of a front – see section 4.5.1.2), something that cannot be captured by the coupled 1-D model.

4.4.2 Response of the planktonic ecosystem

The seasonal evolution of the simulated nutrient and chl *a* concentrations, biomass concentrations of ice algae, phytoplankton, and zooplankton, as well as the corresponding detrital fluxes are shown in Figures 4.6 and 4.7. Although the model simulates nitrogen (nitrate+ammonium+urea), silicic acid, and phosphate concentrations in the water

column, we display only the seasonal cycle of nitrogen (Figure 4.6a) because it is the limiting nutrient at all times in the simulations. Nitrogen limitation has been observed on the Mackenzie shelf [Carmack et al., 2004] and is suggested for the nearby Chukchi Sea and Canadian Basin [Gosselin et al., 1997; Codispoti et al., 2005]. The model results indicate that even though winter convection raises the concentration of nutrients in the mixed layer, nitrogen remains < 3 mmol m^{-3} year-round (Figure 4.6a).

In the simulation, ice algae start to accumulate at the bottom of the ice in mid-March (Figure 4.7a) when the irradiance increases (Figure 4.4c). The simulated ice algal biomass peaks at the beginning of June (Figure 4.7a). The subsequent biomass decrease coincides with the thinning of the snow cover (Figure 4.4d) that allows an increase in radiation absorption in the ice, which in turn leads to ice warming and bottom-ice melting (not shown). Melting at the bottom of the ice creates a thin freshwater lens above the mixed layer, which limits nutrient supply to the bottom of the ice and leads to the decrease in ice algal production (Figure 4.7d). Loss of ice algal biomass to the water column follows shortly as melting of the ice increases and the algal cells are expelled into the water column. The decrease in snow and ice algal biomass leads to an increase in PAR at the top of the mixed layer, which is sufficient to initiate phytoplankton production (Figure 4.7b and d). A near-surface phytoplankton bloom develops as soon as the ice cover disappears (Figures 4.6b, 4.7b and d). The zooplankton biomass starts to increase as the phytoplankton bloom develops, but so slowly that only a small portion of the surface phytoplankton or ice algal production is grazed (Figure 4.7d).

The phytoplankton bloom that develops as the ice cover disappears rapidly depletes surface nitrogen (Figure 4.6a). A progressive deepening of the bloom accompanies the decrease in surface nitrogen concentration, because of the interplay between light and nutrient limitation (Figures 4.6a and b, 4.7b). The simulated deepening of the surface bloom to form a deep (~30m) chlorophyll maximum late in the growing season matches observations [e.g., see Carmack et al., 2004; Hill and Cota, 2005; Forest et al., 2007]. In August, the maximum simulated concentration of chl *a* occurs at the base of the winter mixed layer (Figure 4.6b), where light and nutrients are still sufficient to support primary

production. However, when comparing observed and simulated nutrient profiles on August 4 (Figure 4.6c and d) we note that nutrient depletion (or reduction) reached greater depths in the observations than in the simulation (Figure 4.6c and d). This greater availability of nutrient in the model leads to the development of a chl *a* peak at a depth of about 28 m on August 4, not present in the observations (Figure 4.6e). Such peaks do occur though, as observed on September 1 (Figure 4.6e). The chl *a* profile simulated at the end of August is similar to the observations on September 1, even if the peak does not reach the observed magnitude (Figure 4.6e), but it is "damped" a few days later by the important simulated wind mixing event. The maximum zooplankton biomass is associated with the sub-surface phytoplankton bloom (Figure 4.7c).

The total annual simulated primary production (ice algae and phytoplankton) equals 23.3 g-C m^{-2} yr^{-1}, while the simulated secondary production equals 4.4 g-C m^{-2} yr^{-1} (Table 4.2, "Control"). Ice algal production contributed only 4.1% to the total primary production but 11% to the detrital flux at 118 m. The total detrital fluxes at the 50 m (export production) and 118 m horizons amount to 9.9 and 5.1 g-C m^{-2} yr^{-1}. At depths where there is only remineralization and sinking of detritus, eq. (4.14) can be solved for the steady state [Denman and Peña, 1999], giving an exponential decrease for detritus and hence detrital flux, for constant remineralization rate and sinking speed. Extrapolation of the modelled detrital fluxes at depths of 50 and 118 m with an assumed exponential depth dependence gives an estimate for the sinking flux of detritus at 150 m of ~4 g-C m^{-2} yr^{-1}, which may be compared with the marine biogenic fraction of the carbon flux of 2-4 g-C m^{-2} yr^{-1} observed at ~150 m water depth near the Beaufort Shelf edge in 1987-88 [O'Brien et al., 2006]. Assuming that the new production is equal to the export production, we obtain an *f*-ratio of 0.43. These estimates are in the range of values estimated by other authors and give confidence in the model results. However, both the primary production measured at station 9 by Carmack et al. [2004] (Figure 4.7d) and the detrital fluxes measured by O'Brien et al. [2006] at station SS3 (Figure 4.7e) indicate that the simulated phytoplankton production is delayed by about a month. Assuming that the observed detrital flux in May results from ice algal sedimentation [see O'Brien et al., 2006], the simulated ice algal detrital flux would also be delayed by a month (Figure 4.7e).

Simulated values of phytoplankton primary production and detrital flux are higher than those estimated from observations, but in both cases, there were no observations during the two month period when the simulated rates are highest.

4.5. Evaluation of model results

4.5.1 Sensitivity analyses

The planktonic ecosystem of the Mackenzie shelf is influenced by several physical factors that exhibit high seasonal modulation including a large river run-off, large-scale oceanic currents, a mobile ice pack and winds that can generate upwelling at the shelf break [e.g., Macdonald et al., 1987; Carmack and Chapman, 2003; O'Brien et al., 2006]. To initiate biological simulations for this shelf, we have deliberately chosen the central outer shelf because: 1) it is removed from the major influence of the Mackenzie River, 2) it is located in a region where currents [McCullough et al., 1988; Kulikov et al., 1998; Carmack and Kulikov, 1998] and ice edge are aligned along the shelf edge, and mixed layer temperature and nutrient concentrations [e.g., Grainger, 1975; O'Brien et al., 2006; Fissel and Melling, 1990] tend to exhibit gradients across the shelf, 3) previous studies provide a relatively good set of data to initiate and validate bio-physical models [e.g., Carmack et al., 2004; O'Brien et al., 2006; Macdonald et al., 1987], and 4) the Arctic shelf edge has been suggested to be critically sensitive to change in ice climate [Carmack and Chapman, 2003]. We infer from previous studies that the biological and physical properties of the water column along the shelf break are sufficiently uniform that cross-shelf (rather than alongshore) advection likely explains most of the discrepancies between the simulated and observed properties that cannot be accounted for by examination of one-dimensional processes. Given these assumptions, we may apply our 1D model to the questions of how variations in ice cover and freshwater runoff might affect primary and export production.

4.5.1.1 Bloom timing

Observations of primary production and detrital flux suggest that the surface phytoplankton bloom occurred earlier than that simulated by the model (see section 4.2). The relatively high primary production estimated by Carmack et al. [2004] at the end of

May (Figure 4.7d) was measured when ice was still present (Figure 4.4d). The presence of chl *a* in the mixed layer at this time can be explained in three ways: presence of sloughed ice algal cells, increased light availability, and horizontal advection from nearby leads. In the model, the bottom of the ice starts to melt and ice algal cells start to fall into the water column at the end of May. However, the sediment trap data suggest that release of ice algal cells into the water column could have occurred a month earlier than this (Figure 4.7e). Some of the sampled chl *a* could thus have originated from ice algae. The ice break-up on the Mackenzie shelf in 1987 reportedly occurred in May [O'Brien et al., 2006] or at the beginning of June [Carmack et al., 2004]. Although ice remained in the modelled area (observations in Figure 4.4d), the ice cover was discontinuous with 10 to 30% open water in leads [see Figure 2c,d in O'Brien et al., 2006], thereby enabling variable and increasing amounts of solar radiation to penetrate the mixed layer. Similar conditions were observed in the same area in 2004, with a peak ice algal flux to the bottom occurring in late May and early June [Forest et al., 2007].

To investigate how increased occurrence and size of open-water leads might affect phytoplankton growth, we performed a simulation in which ice concentration was reduced from complete coverage to 80% cover starting on May 5 ("cracked ice-cover run", CI, Figure 4.8). This was accomplished by calculating a new PAR at the ocean surface equal to 0.8 times PAR calculated at the base of the ice plus 0.2 times PAR that would be available at the ocean surface if there was no ice. In 1987, the ice pack retreated rapidly [Figure 4.6a, Carmack et al., 2004] such that the Mackenzie shelf was almost entirely free of pack ice by June 23, 1987 (Plate 1a in Kulikov et al. [1998]). Accordingly, we made an additional simulation (using the CI run) in which the ice cover was forced to disappear around mid-June, to account for the early advection of the ice pack off the shelf ("wind pushed ice-cover run", CI+WPI, Figure 4.8). The increase in radiation reaching the mixed layer produces an earlier phytoplankton bloom and peak detrital flux (by about 20 days).). In both cases, the simulated phytoplankton primary production curve follows more closely the observations, especially in May. In the CI case, flattening of the primary production curve results from a more gradual increase in available light compared with the control run. In the CI+WPI case, advection of the ice cover away from the modelling

site occurs before peak freshwater flux which, combined with the loss of melt water, results in a deeper mixed layer, increased nutrient availability, and a peak primary production similar to the control run. In both cases, total primary production is higher than in the control run (see Table 4.2 for a comparison of the production values).

4.5.1.2 Mixed layer characteristics

Convective mixing, freshening of the surface layer by ice melt and freshwater run-off, warming of the surface layer by solar radiation, and wind mixing events are well reproduced by the model. There are, however, some discrepancies, the greatest being a simulated mixed layer containing more heat than was observed (Figure 4.5e), especially during the CI+WPI run where the ice cover disappears earlier. Part of this discrepancy likely results from the use of land-based temperature measurements from Tuktoyaktuk Airport, located about 150 km SSE of the modelling site, to force the model. In summer when the snow and ice have melted, the air is generally warmer over land than over the ocean: hence we have performed additional simulations with reduced (relative to that observed at Tuktoyaktuk) summer air temperature at the modelling site (i.e. maximum air temperatures were limited to 8ºC and 4ºC), both with the initial forcing and for the CI+WPI case, to investigate sensitivity to this problem. The mixed-layer temperature obtained when the ice is allowed to melt *in situ* (as in the control run) is reduced and closer to the observed temperature on September 1 (Figure 4.9). The mixed-layer temperature reduction (in the case where maximum air temperature is set to 4ºC) prevents complete melting of the ice cover in November (Figure 4.9b).

In early September the simulation shows a strong mixing event breaking down near-surface stratification, whereas observations show intensification and shoaling of stratification in one day (Figure 4.5). The temperature and salinity measurements (upward movement of the thermocline and halocline (Figure 4.5e and h)) suggest advection or upwelling of colder, saltier water onto the shelf coupled with advection of a shallow fresher, warmer, surface layer between September 1 and 2. Although the strong winds at the end of August (28 to 31) were blowing from the west and northwest, a direction that does not lead to upwelling, the post-storm readjustment of the water masses to the storm-

generated coastal set up could explain the observations [see Héquette and Hill, 1993]. The direction of the current at the lower meter of station SS3 (130 m deep, Fig 2c of Carmack and Kulikov [1998]) suggests that some water could have been advected onto the shelf near the modelling site. The record from the upper current meter at station SS3 (35 m deep) also suggests surface water advection from the southwest, a region more likely to contain runoff from the Mackenzie River, which would explain the observed increases in temperature and silicate concentration and decrease in salinity. The increased shear between the upper and lower layers (which were previously flowing in approximately the same direction (Figure 2c of Carmack and Kulikov [1998]) most likely led to increased mixing at the pycnocline and to the high chl *a* value observed on September 2.

4.5.1.3 Primary and export production

The total phytoplankton primary production values obtained for 1987 with the sensitivity runs range between 22.7 and 27.7 g-C m^{-2} yr^{-1} (see Table 4.2). These total primary production values are in the range of values reported for the Beaufort Sea shelf and other Arctic shelves (25 to 50 g-C m^{-2} yr^{-1} [Subba Rao and Platt, 1984; Legendre et al., 1992; Macdonald et al., 1987; Sakshaug, 2004]). Our maximum sub-surface Chl *a* peak (~2.5 mg m^3) is also of the same order of magnitude as that observed by Grainger [1975] (2.2 mg m^3) in the same region, and Carmack et al. [2004] (~4.5 mg m^3, Figure 4.6e). However, our total annual primary production values are higher than the estimate of Carmack et al. [2004] at station 9 (15 g-C m^{-2} yr^{-1}), almost twice as high in the CI+WPI run, even though the simulated primary production curve compares well with their point estimates at this station. As discussed by Carmack et al. [2004], who estimated total annual primary production by interpolating between sparse sampling dates, a bloom or blooms could easily have been missed leading to a low estimate for total primary production. The higher primary production simulated by the model in June and July (Figures 4.7, 4.8 and 4.10, when there were no biological observations for over two months) also suggests that the observations missed a bloom, which would explain the large difference between the two estimates.

Our simulated detrital flux at 118 m (4.9-6.1 g-C m^{-2} yr^{-1}, Table 4.2) is comparable with the mean annual particulate organic carbon flux estimated from sequential sediment traps deployed along the shelf break by O'Brien et al. [2006] and Forest et al. [2007] after correction for depth (2.6-5.1 g-C m^{-2} yr^{-1}). In both studies, a relationship between terrigenous carbon and aluminium was used to discriminate the biogenic from the terrigenous contribution to the total carbon present in the traps, allowing the comparison with the model results that represent the marine production fraction only. Our simulated detrital fluxes are higher than the detrital flux measured close to the modelling site [~1.5 g-C m^{-2} yr^{-1}, station SS-3 of O'Brien et al., 2006; Forest et al., 2007]. A few factors can explain this discrepancy, including inherent inaccuracies of measuring flux with particle interception devices [e.g., Michaels et al., 1994], and strong currents at station SS3, which may have led to under–collection of sinking particles, as suggested by O'Brien et al. [2006]. Another factor might be the export to the interior ocean of some of the shelf's new production as dissolved organic carbon (DOC). From measurements made across the Chukchi shelf and in the Canada Basin, Davis and Berner [2005] suggested that the observed seasonal increase in amino acid and sugar concentration (a component of DOC they attributed to phytoplankton) in surface water of the Arctic basin derived from the shelf. Vernet et al. [1998] also proposed that polar phytoplankton could produce more DOC than previously thought, especially during the ice-edge bloom.

Our modelled *f*-ratios (export/total PP in Table 4.2) fall within the range usually observed in polar regions (0.4 to 0.65 [Harrison et al., 1982; Smith et al., 1997; Sambrotto et al., 1984]), and are similar to the estimate of Macdonald et al. [1998] for the Mackenzie shelf (0.4). Moran and Smith [2000] also estimated the POC export flux from the upper 50 m at the Mackenzie Shelf edge (using ^{234}Th tracers) in the August-September 1995 period to be between 48-84 mg-C m^{-2} d^{-1}. These values compare well with our simulated estimate of export production for the same period in 1987 (15-80 mg-C m^{-2} d^{-1}).

4.5.1.4 Ice algae

Simulated ice algal production averaged 6.3 mg-C m^{-2} d^{-1} over a 150-day period with a peak value of ~12 mg-C m^{-2} d^{-1} (Figure 4.7d). These estimates are lower than those

measured by Horner and Schrader [1982] in the nearshore Beaufort Sea (average ice algal production of 36 mg-C m^{-2} d^{-1} with peak of 62 mg-C m^{-2} d^{-1} in May) and by Gosselin et al. [1997] in the Chukchi Sea (particulate production of 28±28 mg-C m^{-2} d^{-1}). The ice algal contribution to total primary production (4%) is also lower than what is generally reported for shelf areas [5 to 10%, e.g., Gosselin et al., 1997; Horner and Schrader, 1982]. However, the maximum simulated biomass (27 mg-chl *a* m^{-2}) is of the same order of magnitude as that observed by different authors in the region (e.g. 22.3 mg-chl *a* m^{-2} [Juul-Pedersen et al., 2008], 26 mg-chl *a* m^{-2} [Horner and Schrader, 1982], 30-40 mg-chl *a* m^{-2} under 6 to 13 cm of snow [Hopky et al., 1994]) and observed during the same period (end of May, beginning of June). The differences in production most likely result from nutrient limitation. In the control simulation, nutrients are more limiting than light at the bottom of the ice starting end of March (not shown). As shown in Figure 4.6, the concentration of nutrients remains low year-round at the modelling site, while Horner and Schrader [1982] measured under ice nitrate concentrations of ~10 mmol-N m^{-3} and the Chukchi Sea is known for elevated concentrations of nutrient supplied through Pacific inflow.

Ice algae sometimes act as seed population for the open water phytoplankton bloom [see Leventer 2003 and references therein], depending on whether algae shed from ice remain suspended in the water column or not. Whether ice algae sink or remain suspended depends on their physiological condition [Riebesell et al., 1991], as well as on the speed of release from the ice [Fortier et al., 2002], the latter potentially affecting the former. Although we do not know if seeding occurs in the Beaufort Sea, we tested the possible importance of this process in the model by varying the fraction of sloughed ice algae that is transferred to the phytoplankton pool (the term (1-fad) in eq. (4.6), Figure 4.10). Increased seeding leads to an earlier phytoplankton bloom (Figure 4.10a). However, the bloom reaches nutrient depletion faster and deepens more slowly than when no seeding occurs since the top of the seasonal layer is more stratified (ice still present). The peak in vertically integrated production is thus lower when seeding occurs, and the total annual production remains unchanged (Table 4.2).

The contribution of ice algae to the total detrital flux is greater than its contribution to the total primary production (Table 4.2). One reason for this difference is that phytoplankton contribute both to slow- and fast-sinking detritus, whereas the ice algal detritus only have a fast-sinking component. Another reason for the higher ice algal contribution to the deep detrital pool is that when the ice starts to melt, releasing ice algal cells into the water column, zooplankton biomass is still too low to have a significant grazing impact, as observed by Forest et al. [2007]. In addition, ice algae are usually more "sticky" than phytoplankton, which favours formation of aggregates that can sink rapidly to deeper water. Riebesell et al. [1991] observed ice algal cells sinking at speed of 200 to 600 m d^{-1}, much greater than the 50 m d^{-1} used in the model.

4.5.1.5 Zooplankton

In the model, zooplankton start to grow as food becomes available. There is thus a delay between the phytoplankton spring bloom and the maximum zooplankton biomass, the latter being associated with the sub-surface phytoplankton maximum (Figure 4.7). Forest et al. [2007] also observed the presence of large calanoïds to coincide with the deep chl *a* maximum. In the cases where phytoplankton production starts earlier and spreads over a longer time period, the primary and secondary production "mismatch" is reduced and zooplankton productivity increases (see Figure 4.8b and c, and Table 4.2). The maximum change in secondary to primary production ratios between the different simulations is of about 13% (see Table 4.2).

Some of the main zooplankton species observed on the Beaufort and Chukchi Seas are *Pseudocalanus* spp., *Calanus glacialis* and *Calanus hyperboreus* [Forbes et al., 1992; Ashjian et al., 2003; Forest et al., 2007]. *Pseudocalanus* spp. would be present in the spring and feed on the sloughed ice algae. However, they are small-bodied animals, would follow the retreating ice-edge, and probably do not affect the fate of primary production as much as the large-bodied species *C. glacialis* and *C. hyperboreus* [Ashjian et al., 2003]. These two deep-water species would reproduce in the Arctic Basin, be advected onto the outer shelf in the summer and return to deep water for diapause in fall [Ashjian et al., 2003]. A life history model would improve the representation of the

biomass evolution of these species, even though their advection on the shelf is partly dependent on circulation, but too little information is currently available to constrain such a model.

4.5.2 Nutrient availability

Primary production is hypothesized to increase with climate change as ice cover decreases. Although the shelf was clear of ice by the end of June in 1987 [Kulikov et al., 1998], the total export production simulated for 1987 (10-12 g-C m^{-2} yr^{-1} in Table 4.2) is below the new production estimated for 1974 (16 g-C m^{-2} yr^{-1}, [Macdonald et al., 1987]), when ice remained close to the shore. These two years represent extremes over 25 years of data: 1974 having the heaviest summer ice conditions, and 1987 having unusually high temperatures and salinities [Fissel and Melling, 1990]. Nutrient availability could explain the difference: our results show that the timing of the bloom has an effect on the amplitude of the spring bloom but not much impact on the total primary production when mixing remains about the same (Figures 4.8 and 4.10, Table 4.2). The increase in total primary production (18% between control and CI+WPI) results in part from a longer period of wind mixing, a higher surface salinity due to the loss of melt water, and a deeper heating by solar radiation, which lead to a slightly deeper mixed layer (and thus increased nutrient supply). The amount of nutrients available at the end of the winter thus appears to be an important factor determining the magnitude of the spring bloom and thus, total primary production. Pre-conditioning of salinity over the shelf in the fall (removal of freshwater) has been observed to be an important factor in the formation of water dense enough to ventilate the halocline [Melling and Moore, 1995]. Similarly, wind mixing in the fall would both increase the concentration of nutrient in the mixed layer and favour deeper convective mixing in the winter, thereby increasing the amount of nutrients available the following spring to support primary production.

4.6. Conclusions

We have presented a coupled sea ice-ocean-biological 1D model, including ice algae production, that simulates a complete seasonal cycle of primary and export production in

the Arctic Ocean. We used the model, implemented on the Beaufort Sea shelf for the year 1987, to investigate the relative importance of various physical processes in controlling the timing and quantity of primary production and biogenic particle export. The model is particularly useful to study what happens during ice break-up when sampling is difficult. The model results show that the increase in light in the mixed layer resulting from the opening or disappearance of the ice cover controls the timing of the phytoplankton bloom. Ice cover also controls in part the magnitude of the bloom: a gradual opening of the ice cover early in the season, when solar radiation has not reached its maximum intensity, leads to a longer bloom of lower magnitude; but a more rapid melting of the ice later in the season when solar radiation is at maximum intensity leads to a shorter but more intense bloom. The simulations showed that the spring bloom, occurring during and/or just after ice break-up, represents a significant fraction of the total annual primary production. Hence, calculations of total annual primary production requiring interpolation of observations taken before ice break-up and after the ice is completely gone would tend towards underestimation.

Total annual primary production is more sensitive to nutrient availability than to the more dramatic changes in the timing/strength of the spring bloom. Although an earlier break-up of the ice cover in our sensitivity study showed a 11-18% increase in primary production, much of the increase resulted from wind mixing sustained over a longer period entraining additional nutrients into the mixed layer. The supply of nutrients to support summer primary production is determined in part by preconditioning during the previous year: freshwater input and removal influence the impact of fall storms, which increase nutrient input to the mixed layer through both wind mixing and increased winter convection.

Our sensitivity studies indicate that export production is closely tied to primary production: the ratio of (annual) export production to primary production ranged only from 0.42 to 0.44 across all seven of our simulations. Hence changes in total primary production resulting from climate change, either in magnitude or in areal extent of open water, should also be reflected in changes in export production, although the ratio of export production to primary production may change in the future if the temperature

sensitivity of the recycling components of the foodweb is different from the temperature sensitivity of primary production [e.g., Denman and Peña, 2002]. As the area of the permanent pack ice in the Arctic shrinks [Stroeve et al., 2007], leaving more open water in the marginal seas in late summer, primary production will increase. This increase should more than compensate for the reduction in ice algal production resulting from earlier ice melting, because of the small fraction of primary production contributed by ice algae.

Table 4.1. Values and units for variables and parameters used in and calculated by the biological model.

Variable	Definition	Estimated value	Unit
a_d	Specific attenuation coefficient for detritus	0.03	m^2 (mmol-N)$^{-1}$
a_P	Specific attenuation coefficient for phytoplankton	0.03[1]	m^2 (mmol-N)$^{-1}$
α^B	Photosynthetic efficiency	0.08[2,3]	mg-C (mg-chl *a*)$^{-1}$ h^{-1} (W m^{-2})$^{-1}$
β	Photoinhibition	0.002[4]	mg-C (mg-chl *a*)$^{-1}$ h^{-1} (W m^{-2})$^{-1}$
E_{zn}	Zooplankton excretion rate	0.03	d^{-1}
g_a	Assimilation efficiency of zooplankton	0.7	dimensionless
G_D	Grazing rate on detritus	calculated	d^{-1}
G_{Phy}	Grazing rate on phytoplankton	calculated	d^{-1}
fad	Fraction of sloughed ice algae that goes to detritus	0.9	dimensionless
fd_1	Fraction of fast-sinking detritus used as food	0.5	dimensionless
fd_2	Fraction of ice algal detritus used as food	0.8	dimensionless
γ_{Ds}	Remineralization rate of slow-sinking detritus	0.05[5]	d^{-1}
γ_{Df}	Remineralization rate of fast-sinking detritus	0.33[5]	d^{-1}
γ_{Si}	Dissolution rate for Si (detritus)	0.03[6]	d^{-1}
κ_w	Attenuation coefficient of pure sea water	0.05[5]	m^{-1}
κ_p	Attenuation coefficient of phytoplankton	calculated	m^{-1}
κ_d	Attenuation coefficient of detritus	calculated	m^{-1}
K_P	Half-saturation constant for grazing	1.0	mmol-N m^{-3}
Ks_1	Half-saturation constant for nitrate	1[7]	mmol m^{-3}
Ks_2	Half-saturation constant for silicate	4.0[7]	mmol m^{-3}
Ks_3	Half-saturation constant for phosphate	0.2[7]	mmol m^{-3}
L_{lim}	Light limitation	calculated	dimensionless
M_{Phy}	Specific mortality rate of phytoplankton	0.05[1,5]	d^{-1}
M_Z	Specific mortality rate of zooplankton	0.01	d^{-1}
N_i	Concentration of nutrients (i =1 to 3)	calculated	mmol m^{-3}
N_{lim}	Nutrient limitation	calculated	dimensionless
μ	Specific phytoplankton growth rate	calculated	d^{-1}
μ_{max}	Maximum phytoplankton growth rate	calculated	d^{-1}
Phy	Phytoplankton biomass	calculated	mmol-N m^{-3}
P_m^B	Maximum photosynthetic rate	1.8[2,3]	mg-C (mg-chl *a*)$^{-1}$ h^{-1}
r_m	Maximum zooplankton grazing rate	0.5	d^{-1}
w_f	Sinking rate for ice algae and fats-sinking detritus	50[5]	m d^{-1}
w_s	Sinking rate for slow-sinking detritus	1[5]	m d^{-1}

[1]Chai et al. [2002], [2]Harrison and Platt [1986], [3]Sakshaug and Slagstad [1991], [4]Subba Rao and Platt [1984], [5]Slagstad et al. [1999], [6]Bidle and Azam. [1999], [7]Lancelot et al. [2000]

Table 4.2. Results of sensitivity simulations. Total primary production (PP, g-C m^{-2}), ice algal contribution to PP, secondary production (SP, g-C m^{-2}), total detrital flux through the 50 and 118 m horizons (g-C m^{-2}), ice algal contribution to detritus at 118 m, and ratio of export at 50 m to total PP.

	Control	CI	CI+ WPI	CI+WPI T ≤ 4ºC	T ≤ 4ºC	T ≤ 8ºC	10% seed	50% seed
Total PP	23.3	26.3	27.6	27.7	22.7	23.8	23.3	23.3
IA to PP	4.1%	3.4%	3.2%	3.2%	4.3%	4.0%	4.1%	4.0%
Total SP	4.4	5.4	5.9	6.0	4.4	4.7	4.5	4.7
Det. at 50 m	9.9	11.5	11.9	11.9	9.6	9.9	9.9	9.8
Det. at 118 m	5.1	5.9	6.1	6.1	4.9	5.1	5.1	5.0
IA to Det	11%	8.6%	7.8%	7.8%	11.4%	11%	9.8%	5.4%
Export/Tot PP	0.43	0.44	0.43	0.43	0.42	0.42	0.43	0.42

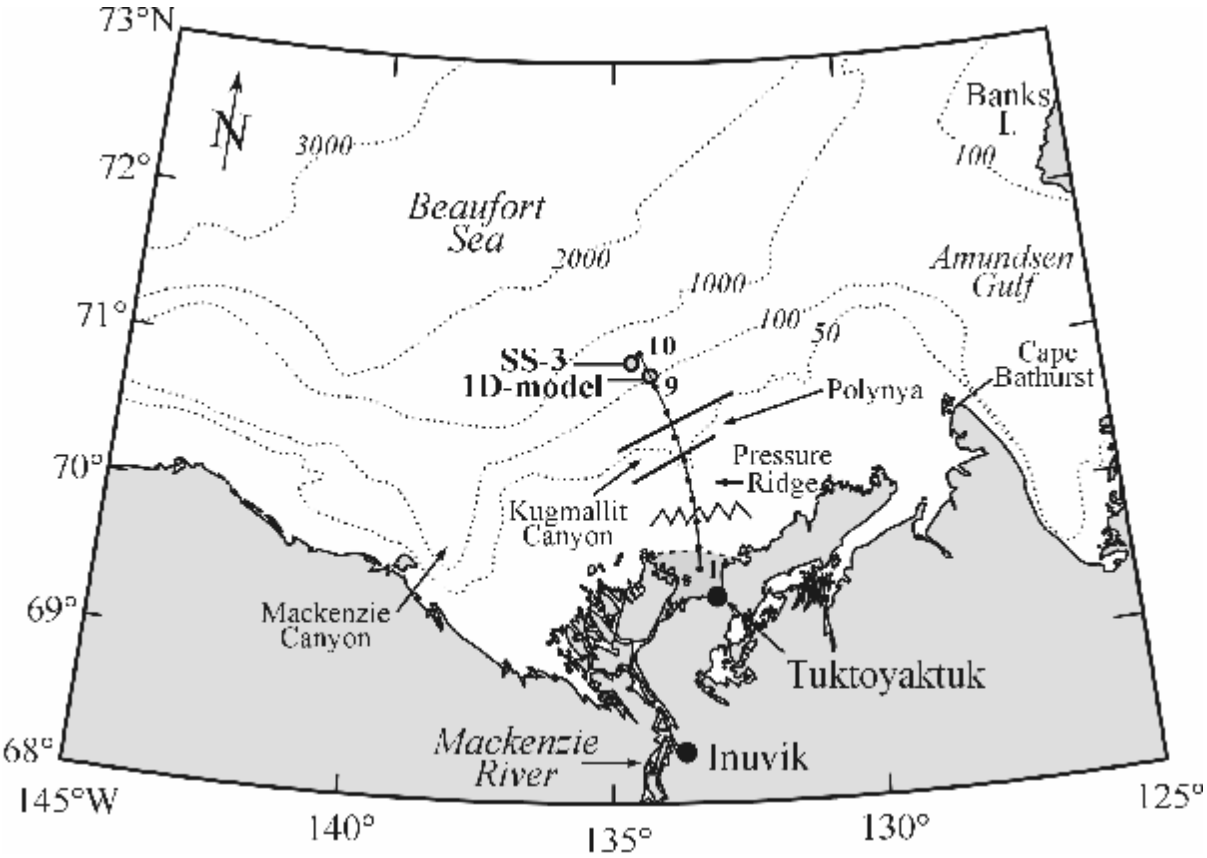

Figure 4.1. Study area and location of the sampling stations (dots) in the Beaufort Sea of the Arctic Ocean. Also marked is the site upon which the 1D model was based and the sediment trap SS-3 (circles) site where particle fluxes were measured throughout a full year (1987-88).

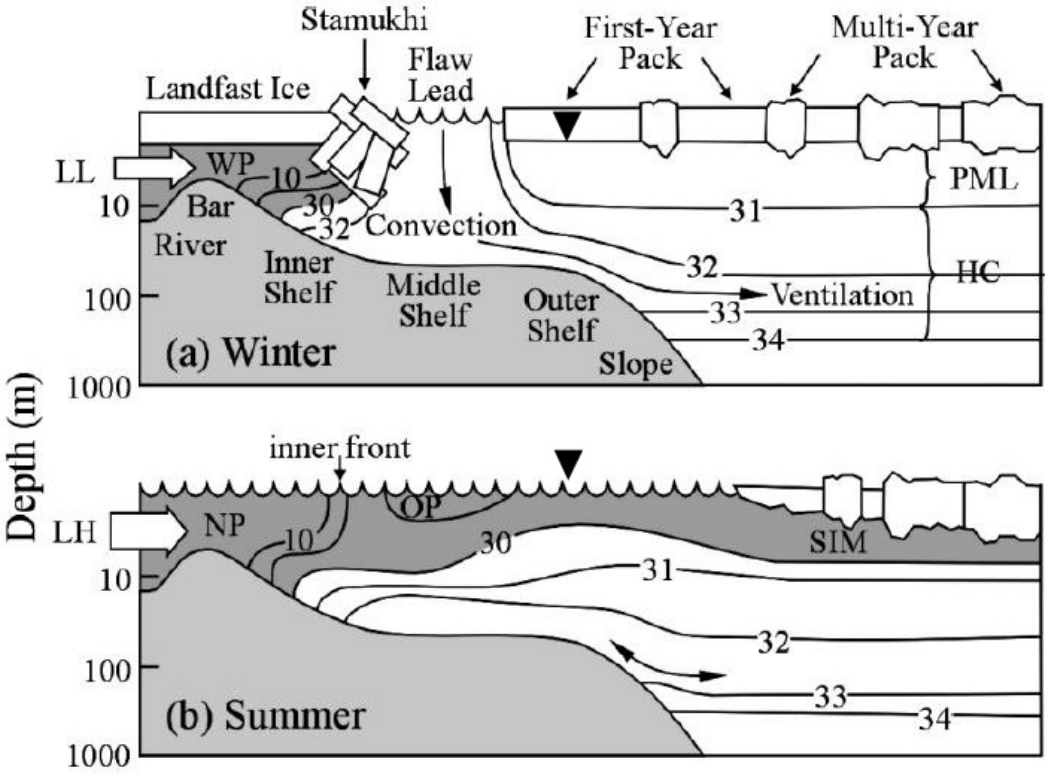

Figure 4.2. A schematic representation of the Mackenzie Shelf in (a) winter and (b) summer (from Carmack et al. [2004]). A mid-shelf section perpendicular to the coast (see Figure 4.1) shows the water mass structure (depicted by isolines of salinity) out to and beyond the modelling site (approximate location indicated by the inverted black triangles). Abbreviations: LL = lower low river discharge, LH = lower high river discharge, WP = winter plume, NP = new (summer) plume, OP = old (winter) plume, PML = polar mixed layer, HC = halocline complex, SIM = sea ice melt.

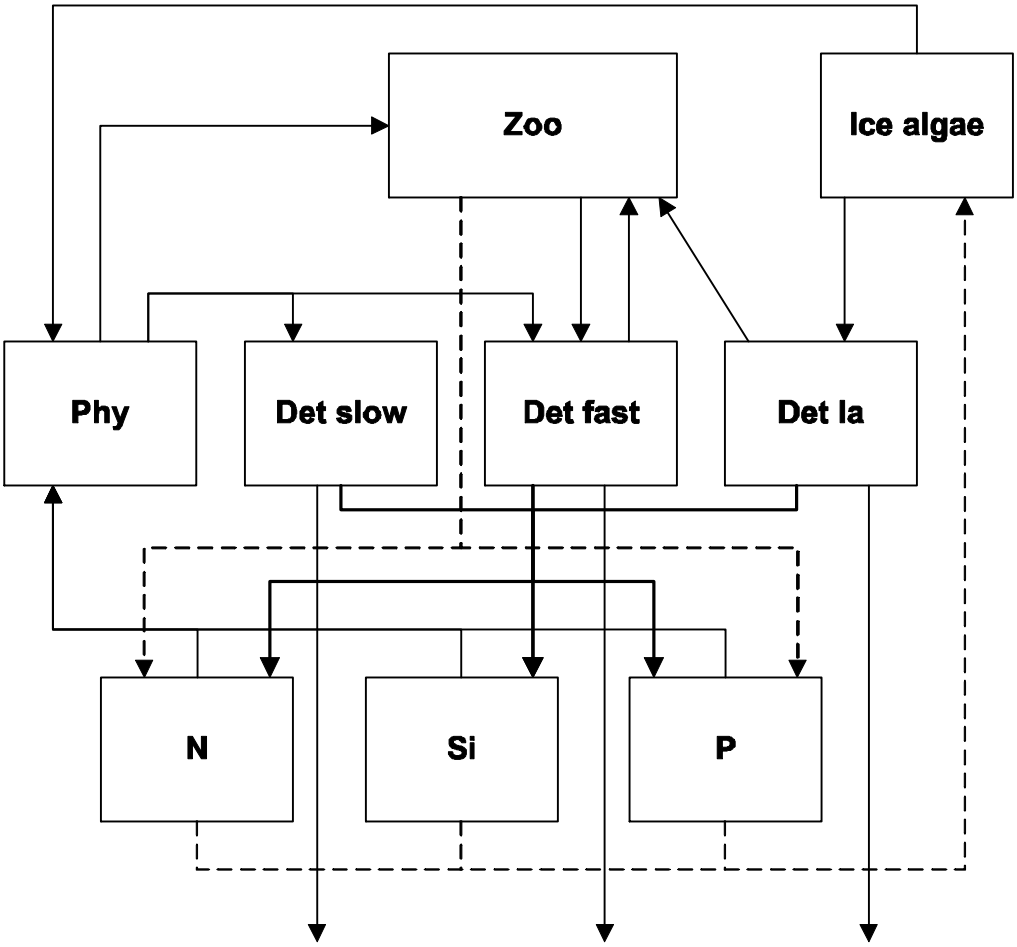

Figure 4.3. Schematic diagram for the biological model.

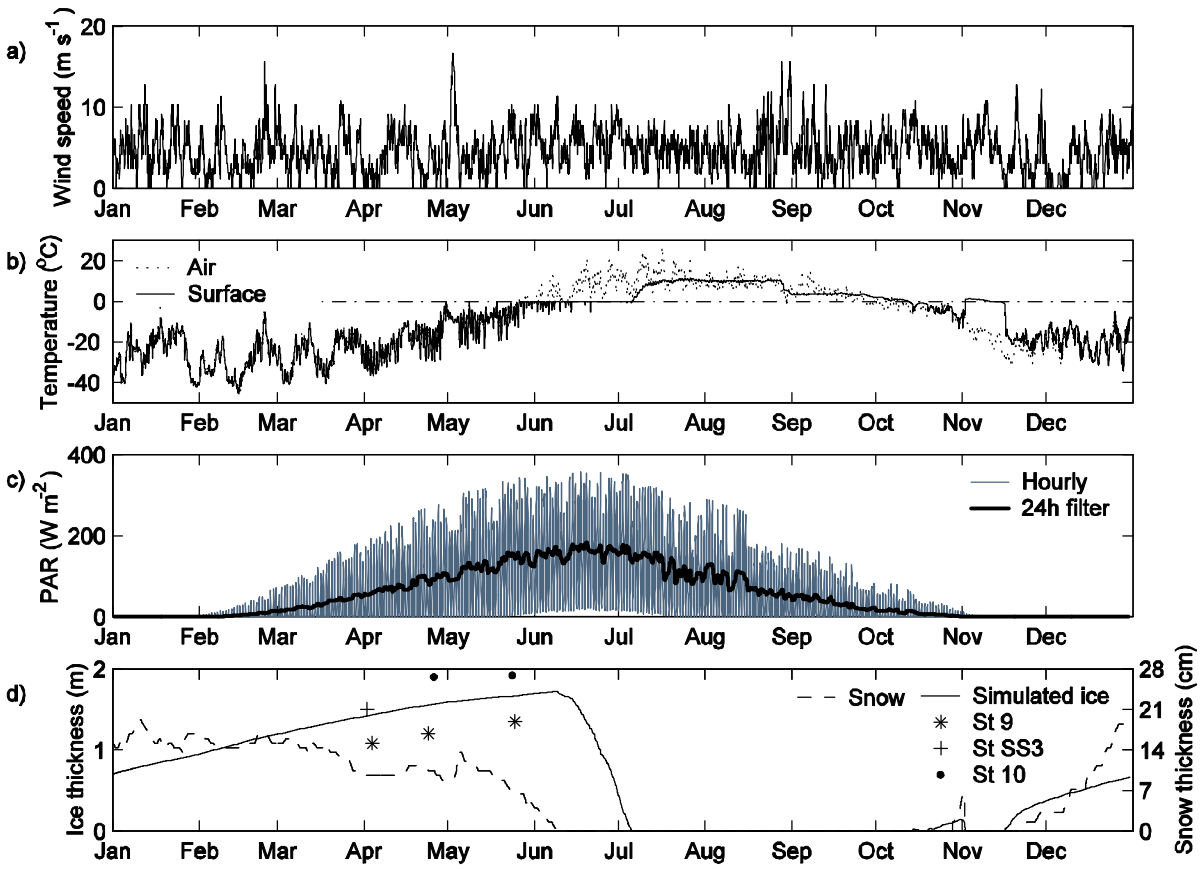

Figure 4.4. Time series of: (a) hourly observed wind speed for 1987 at Tuktoyaktuk (Environment Canada), (b) hourly observed air temperature for 1987 (at Tuktoyaktuk; Environment Canada) and simulated surface temperature, (c) simulated PAR at the modelling site (70° 45'), hourly-averaged and 24h low-passed (d) observed snow thickness, and observed (at stations 9, 10 and SS3 in Figure 4.1) and simulated ice thickness. When sea ice forms, the snow thickness from the previous day is removed from the current day observation since the latter was measured on land.

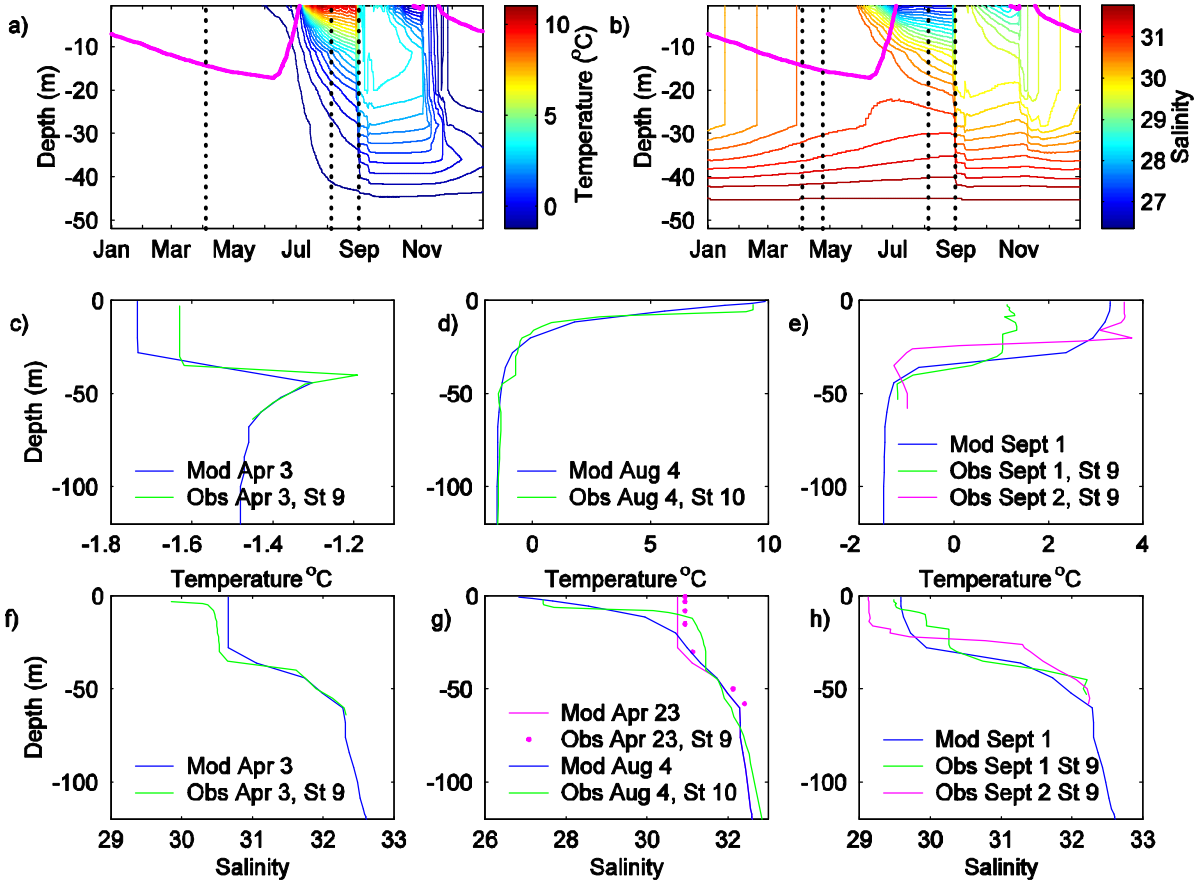

Figure 4.5. Simulated water column (a) temperature and (b) salinity over the year (1987) for the control run. The magenta line denotes ice thickness (in dm projected on the depth axis). The sampling dates are indicated on panels (a) and (b) by dotted lines. Comparison between simulated and observed temperature profiles on (c) April 3, (d) August 4, and (e) September 1 and 2, and comparison between simulated and observed salinity profiles on (f) April 3, (g) April 23, and August 4, and (h) September 1 and 2. The observed salinity on April 23 (g) was sampled with GoFlo bottles [Macdonald et al., 1988b]. The other observations were obtained with a CTD [Macdonald et al., 1988a; Carmack et al., 1989].

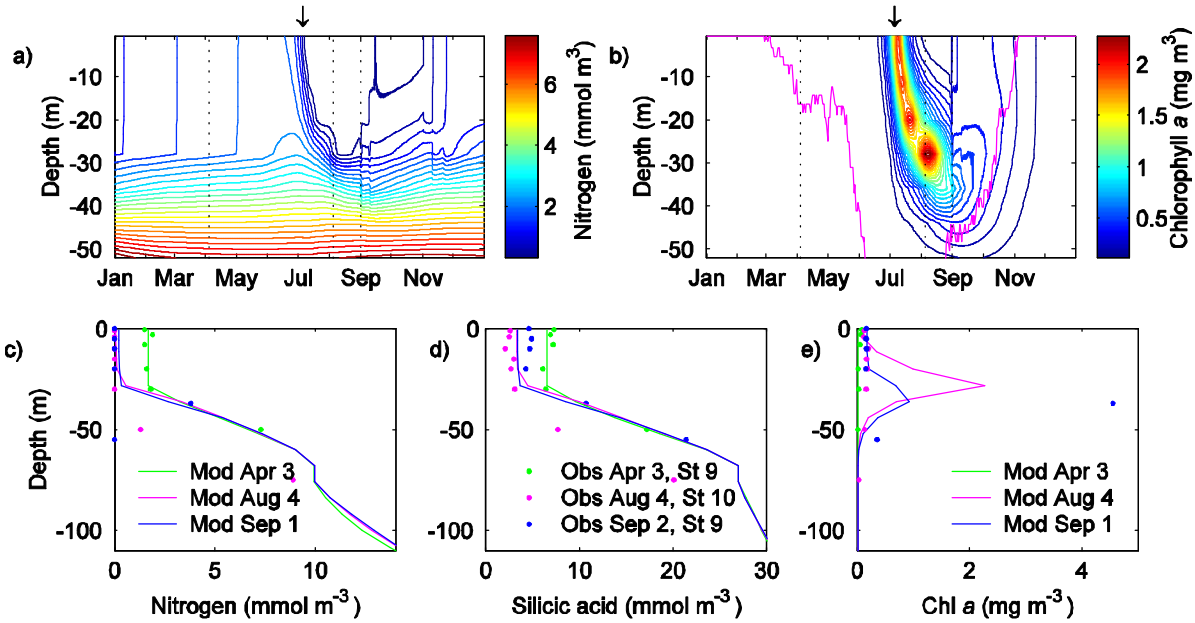

Figure 4.6. Simulated concentration of (a) nitrogen and (b) phytoplankton chl *a* in the water column over the year (1987) for the control run (the magenta line is the daily averaged depth of compensation intensity – where photosynthesis equals respiration). Profiles of simulated and observed concentration [Macdonald et al., 1988b,c] of (c) nitrogen, (d) silicic acid and (e) chl *a* on different dates. Note: nitrogen observations include nitrate only while the simulated nitrogen includes nitrate, ammonium and urea. The dates plotted in the lower panels are indicated on the upper panels by vertical dotted lines.

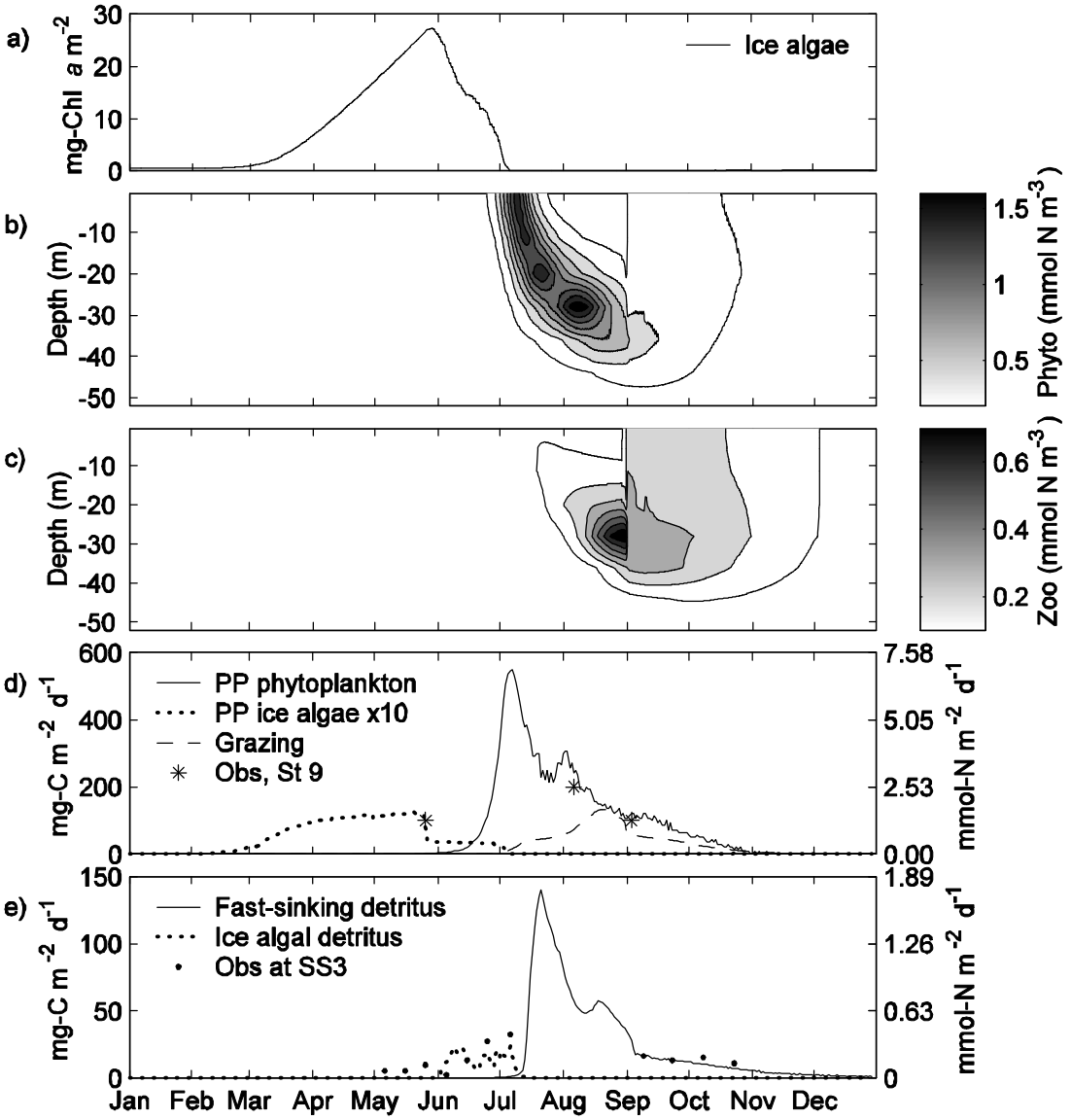

Figure 4.7. Simulated (a) ice algal biomass, (b) phytoplankton biomass, (c) zooplankton biomass, and (d) depth-integrated daily production of ice algae (dotted line) and phytoplankton (solid line), compared with primary production estimated by Carmack et al. [2004] at station #9, and simulated depth-integrated zooplankton grazing rate on phytoplankton, and (e) simulated daily flux of fast-sinking and ice algal detritus below the 118 m depth horizon, compared with biogenic carbon flux measured at a depth of 125 and 128 m at station SS3 and adjusted for 118 m (from Figure 13 of O'Brien et al. [2006]). Right hand axes in (d) and (e) are calculated from left hand axes with a fixed C:N ratio of 6.6:1 (mol:mol). Simulations and observations are for the year 1987.

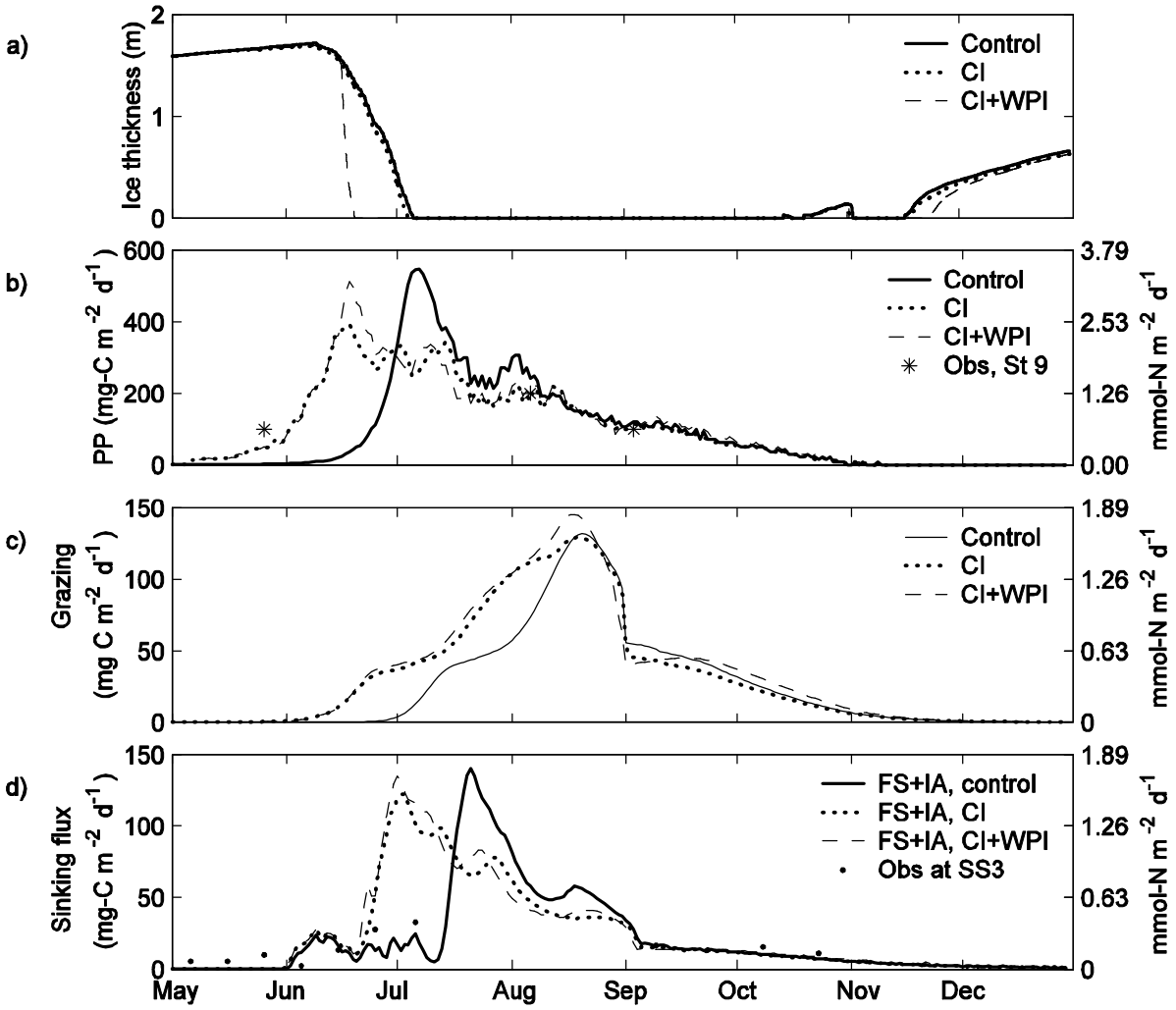

Figure 4.8. (a) Simulated ice thickness for the control, cracked ice (CI) and cracked and wind pushed ice (CI+WPI) runs, (b) observed (1987) and simulated depth-integrated phytoplankton primary production for the three runs, (c) simulated depth-integrated zooplankton grazing rate on phytoplankton for the three runs, and (d) observed detrital flux (1987) from 125 and 128 m at station SS3 adjusted to 118 m, and simulated daily flux of fast-sinking (FS) and ice algal (IA) detritus below the 118 m depth horizon for the three runs.

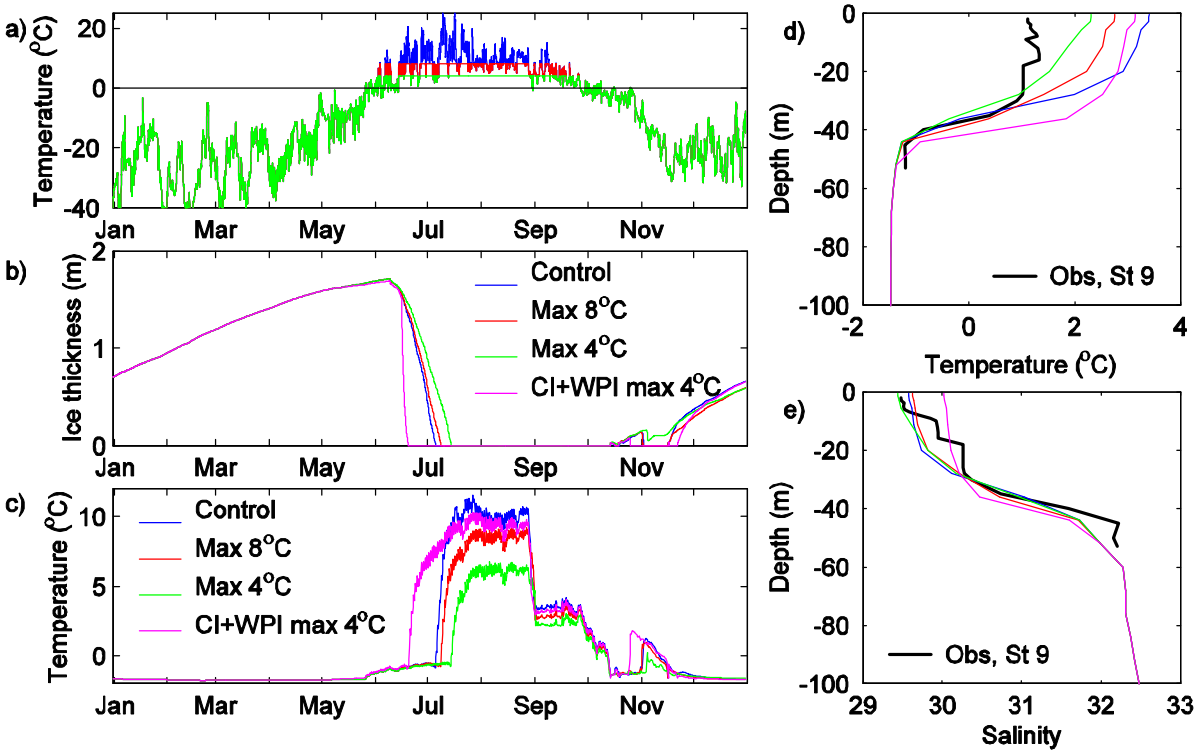

Figure 4.9. (a) Observed air temperature for 1987 (blue), limited to a maximum of 8ºC (red) and 4ºC (green), (b) simulated sea ice thickness with the observed air temperature (1987 control), with a maximum air temperature of 8ºC and 4ºC, and for the CI+WPI run with a maximum air temperature of 4ºC, (c) simulated sea surface temperature for the same runs as in (b), and simulated and observed (d) temperature and (e) salinity profiles at the beginning of September 1987 for the same runs as in (b).

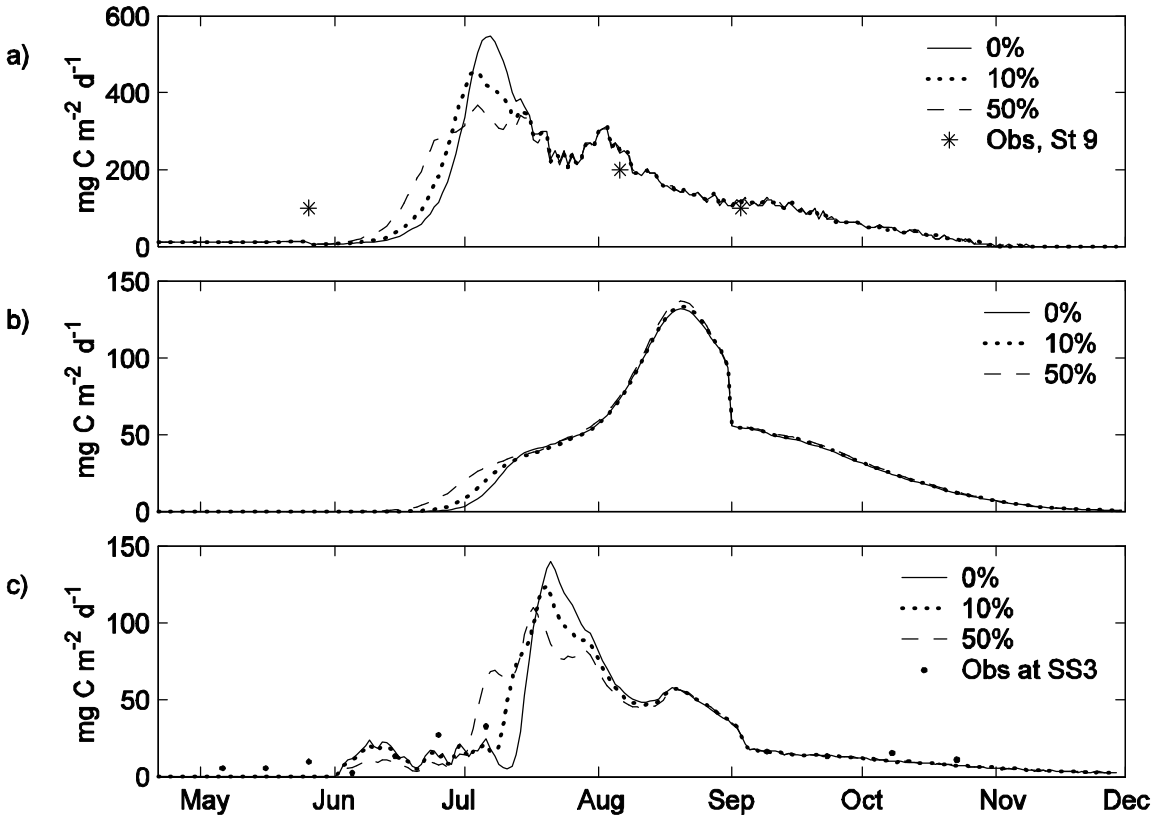

Figure 4.10. (a) Observed and simulated phytoplankton primary production with varying percentage of sloughed ice algal cells used as seeding for the phytoplankton bloom (0% (control run), 10% and 50%), (b) simulated zooplankton grazing on phytoplankton in the same runs as in (a), and (c) observed detrital flux at 125-128 m at station SS3 (1987) adjusted to 118 m, and simulated detrital fluxes at 118 m for the same runs as in (a).

5. Effects of future climate change on primary productivity and export fluxes in the Beaufort Sea.

5.1. Introduction

Sea ice exerts important controls for primary production on Arctic shelves: by providing a substrate for algal growth on the underside of the ice, by limiting the availability of solar irradiance to primary producers, by limiting the development of thermal or freshwater stratification in the freezing season (while enhancing it during the thawing season), and by variously promoting or suppressing diapycnal mixing and shelf-break upwelling [Carmack et al., 2004; Williams et al., 2006]. The distribution of sea ice cover is highly variable on interannual [e.g., Macdonald et al., 1987; O'Brien et al., 2005], decadal and multi-decadal [Polyakov and Johnson, 2000; Polyakov et al., 2002] timescales. An appreciable reduction in perennial ice cover has been observed [Comiso and Parkinson, 2004] and recent rapid reduction in summer minimum sea ice extent [Stroeve et al., 2007] shows observations of ice loss running ahead of the most pessimistic model projections [IPCC, 2007]. Even greater changes are predicted as a consequence of global warming [Anisimov et al., 2004; Johannessen et al., 2004; ACIA, 2005; Holland et al., 2006]. The decline in sea ice extent and thickness is expected to promote increased primary production [e.g., Gradinger, 1995; Loeng et al., 2005]. This increase in primary production would result not so much from an increase in light availability but rather from an increased nutrient supply through wind mixing and shelf-break upwelling [Carmack et al., 2004; Loeng et al., 2005]. It is uncertain, however, to what extent the supply of nutrients to the mixed layer will increase in the highly stratified environment of Arctic shelves, since an increase in freshwater runoff has also been observed and is expected to continue [e.g., Miller and Russell, 2000; Wu et al., 2005; Peterson et al., 2002]. To investigate the impacts on primary production of an increase in freshwater runoff and in the length of the ice-free season, we present projections of future primary production and export fluxes generated with a one-dimensional sea ice-ocean model coupled to a marine ecosystem model [Lavoie et al., 2008]. Forcing is based on observations plus future climate change projections simulated by the Canadian Global Climate Model (CGCM2,

[Flato et al., 2000; Flato and Boer, 2001]) that are applied to the local area with a standard downscaling technique [e.g., Dumas et al., 2006].

5.2. Historical data and climate projections

The model is implemented over the outer shelf region of the Mackenzie Shelf in the Beaufort Sea (see Figure 5.1 and section 4.2 (page 79) for a description of the study area). The model is forced with surface air temperature, wind speed, cloud amount, relative humidity, snowfall and freshwater runoff. Snowfall rates are computed from the daily snow depth accumulation rate. Meteorological data for Tuktoyaktuk Airport were obtained from the Meteorological Service of Canada. Mackenzie River discharge data (at Arctic Red River) were obtained from the Water Survey of Canada (HYDAT CD-ROM). Simulated ice and snow thicknesses are compared with historical data obtained from the Canadian Ice Service at Sachs Harbour (about 360 km away from the modelling site, see Figure 5.1).

We used a 19-year period from the meteorological observations (the years 1974 to 1992 had the least missing data) to force the “present day” simulation. To make projections of future primary production, we used output from the Canadian Centre for Climate Modelling and Analysis (CCCma) coupled global climate model (CGCM2) for the years 1970 to 1989, 2041 to 2060 and 2081 to 2100 (available at http://www.cccma.bc.ec.gc.ca) for four grid cells surrounding the study area (see Figure 5.1). Simulated daily data for the time period 1961-1989 were produced from a CGCM2 simulation forced with historical equivalent greenhouse gas concentrations to 1990. After 1990, the CGCM2 simulation was forced with the SRES 'A2' emissions scenario, often referred to as the “business as usual” scenario [Nakicenovic and Swart, 2000].

We applied a standard downscaling technique to the CGCM2 output to obtain a better approximation of the local conditions (as described in Dumas et al. [2006]). The change in each quantity simulated with CGCM2 is computed between corresponding years of each period (between 1970-1989 and 2041- 2060, and between 1970-1989 and 2081-

2100) and averaged to obtain daily mean changes for each period. We then added the daily mean changes (Figure 5.2) to the 1974-1992 observations to obtain forcing data for the two periods in the future. Note the large increases in wind and temperature during winter months and in precipitation during summer months. In the rest of the paper, we identify each period by its central year (i.e. 1983, 2050 and 2090).

An additional condition has been applied to the air temperature because we found (see section 4.5.1.2, page 95) that using the air temperature measured at Tuktoyaktuk Airport led to excessive warming of the ocean surface at the modelling site. Here we use a maximum forcing temperature of 8ºC at the modelling site for the present day simulation (i.e. temperatures above the maximum are set to the maximum), with a one degree increase for the 2050 and 2090 periods (i.e. 9 and 10ºC respectively). This one degree increase was estimated from the maximum offshore surface air temperature simulated by CGCM2 for each time period in our study area. From Figure 4 of Wu et al. [2005], we estimated an increase in freshwater runoff of 0.01 Sv (or 9%) in total Arctic river inflow between 1983 and 2050. Therefore, we applied a 9% increase in freshwater runoff for the 2050 period and an additional 2% runoff increase between the 2050 and 2090 periods. Results of Miller and Russell [2000] suggest that the increase for the latter period could be higher. However, this 2% increase is similar to the average increase in precipitation minus evaporation (P-E) simulated by CGCM2 between 2050 and 2090 in our study area and corresponds to the total increase of 10% in P-E projected for the Mackenzie watershed between the periods 1960-90 and 2070-90 by Serreze and Barry [2005]. Since the initial concentration of nutrients and profiles of temperature and salinity are the same for the three simulations (January 1987, section 4.3.5, page 88), we removed the first year of each period from our analyses to allow for an adjustment of the mixed layer. The model projections are thus presented as the difference between the average conditions over each 18-year period.

5.3. Results

5.3.1 Present day analysis

We compare the ice thickness simulated with the 1D model for the period 1975-1992 with landfast ice thickness measured at Sachs Harbour (SH) and with pack ice thickness measured at three stations close to the modelling site in 1987 (stations #9, SS3 and #10, Figure 5.3a). Figure 5.3b shows the simulated seasonal evolution of the mixed layer salinity, which is controlled by the input of freshwater from ice melt and river runoff and mixing by winds and convection during ice formation. The first half of the 1980s stands out as a period with less freshwater runoff (Figure 5.3c). This reduction of freshwater flux to the top of the mixed layer led to a reduction of the simulated freshwater inventory (H_f) in the mixed layer (Figure 5.3c) and to deeper convective mixing in winter, as illustrated by the deepening of the nitracline in Figure 5.4. The freshwater inventory in the upper 40 m is expressed as equivalent thickness of freshwater and calculated as $H_f = \int_{-40m}^{0m} \left((S_d - S(z)) / S_d \right) dz$, where $S(z)$ is the salinity at depth z, and S_d=31.74 is the initial salinity in layer 9 (between 40 and 48 m depths) of the model. The simulated ice thickness (Figure 5.3a) is in general agreement with that observed near the modelling site (i.e., in 1987 the simulated ice thickness is an average of the ice thickness measured at nearby sites). Although Sachs Harbour is located slightly inland and northward from the modelling site, which could result in colder winter air temperature, discrepancies between the observed and modelled ice thicknesses result from the difference in observed and modelled on-ice snow thickness. The largest differences occur when the simulated snow cover significantly differs from that observed (e.g. 1975 to 1978).

Figure 5.4 shows the annual cycle of simulated concentration of nitrogen (total inorganic nitrogen, the most limiting nutrient in the present day simulation) in the mixed layer for years 1975 to 1992. Inorganic nitrogen concentration in the mixed layer is controlled primarily by wind mixing (more intense in fall), convection during winter and uptake by primary producers during spring and summer. In general, the lowest surface nitrogen concentration in spring occurs during the first few years of the 18-year simulation, when

the freshwater content in the mixed layer is higher (Figure 5.3c). Higher simulated nitrogen concentrations in spring, starting in 1979 and peaking in 1983-1984, are linked to the deeper winter convective mixing, as indicated by higher salinities (Figure 5.3b) and entrainment of higher concentrations of deep nitrate into the surface layer (Figure 5.4) between April and May. The spring bloom is generally more important during these years (see 1983 and 1984 in Figure 5.5) but, on average, the correlation between annual phytoplankton primary production and the concentration of nitrogen available in the surface layer in spring is low (R^2=0.39, n=18). The length of the period when the modelling site is free of ice has a greater impact on the annual phytoplankton production (R^2=0.51) (see Figures 5.5 and 5.6, and Table 5.1). Although simulated phytoplankton primary production varies little from year to year (22.1±1.8 g-C m^{-2}), we can clearly see that the lowest annual phytoplankton production occurs in years with few open water days (e.g. 1978, and 1986), while the highest annual production is found in years with a high number of open water days (e.g. 1977, 1981, and 1988) or in years with high spring biomass concentration resulting from deep convective mixing and a higher availability of nutrient such as in 1983 and 1984 (see Figures 5.3b, 5.4 and 5.5). High ice algal production and biomass occur in years when thin snow cover combines with low freshwater inventory in the mixed layer (and thus higher nutrient availability to the skeletal layer where the ice algae grow) (Figures 5.3 to 5.5 and Table 5.1). Adding ice algal production to phytoplankton production increases the correlation between primary production and the concentration of nitrogen available in the surface layer in spring (R^2=0.55). The year 1984 was the most productive, combining high ice algal production, an intense spring bloom and high summer phytoplankton production (Figure 5.5 and Table 5.1).

Figure 5.7 shows the total detrital export for two contrasting years of the series: 1975 and 1984. The detrital flux is much higher in 1984 than in 1975 (see Table 5.1) as expected from the higher primary production. However, the ratio of export to total primary production (see *'e*-ratio' in Table 5.1) also increases. This increase results from the greater contribution of ice algae and of the phytoplankton spring bloom to the total primary production. Both are decoupled from the secondary producers which are

associated with the subsurface bloom (see section 4.5.1.5, page 99), and thus a greater proportion of the bloom sinks to the bottom.

5.3.2 Future scenarios

In this section, we compare the average values for each period (1983, 2050 and 2090). The maximum average ice thicknesses are 1.9, 1.6 and 1.3 m respectively, while the maximum average snow thicknesses are 16, 11.3 and 11.9 cm (Figure 5.8a). The decrease in snow thickness in the future projections is linked with delayed ice formation in fall (Figure 5.8a) and with changes in precipitation (general decrease in November and December, Figure 5.2e). The slightly greater snow thickness in 2090 compared to 2050 results from the increase in precipitation at the end of January and beginning of February (Figure 5.2e). The average projected ice-free period (i.e. ice cover absent or with thickness <1 cm) at the modelling site varies from 112 days for 1983, to 148 for 2050, to 159 for 2090 ('OWD' in Table 5.2), representing an increase of 5.4 days per decade for the first period, and 2.8 days per decade for the second period. The ice decrease is more important in spring (Figure 5.8a): the peak rate of ice loss occurs about three weeks earlier by 2050 (relative to 1983) and about five weeks earlier by 2090.

The reduction in simulated ice thickness in the future runs leads to reduced mixing in winter resulting from reduced friction velocities between the ice and the surface of the water column, which are indirectly a function of ice thickness (through the roughness length, see section 4.3.2, page 82). The increase in freshwater runoff combined with reduced mixing leads to a decrease in the mean simulated surface salinity in the upper 40 m (by about 1 psu, Figure 5.8b). Maximum salinity occurs at the time of maximum ice thickness and minimum salinity at the onset of ice formation. The average freshwater inventory in the upper 40 m increases from 1.5 m for 1983, to 2.1 m in 2050, to 2.6 m in 2090. Reduced salinities in the upper layer also lead to a reduction in the depth of winter convective mixing and a shallowing of the mixed layer depth during the period of ice cover (Figure 5.8c). Reduction of the mixed layer depth leads to a reduction of the average nitrate concentration in the top 40 m of the water column (Figure 5.8d) and of nitrate concentration in the top 20 m between February and April, that in turn leads to a

reduction in spring bloom chl *a* concentration. However, the subsurface bloom lasts longer, owing to the longer ice-free period, penetrates deeper, and reaches higher chl a concentrations (not shown). These changes result in a modest increase in the average simulated primary production between periods (Figure 5.9). Average total annual primary production increases by 6% between 1983 and 2050, and by 9% between 1983 and 2090, representing an increase of about 3% between 2050 and 2090 (see Table 5.2).

The contribution of ice algal to total annual primary production decreases in the future scenarios (Table 5.2). Daily ice algal growth increases early in the season due to the increase in light availability (thinner ice and snow cover) but decreases thereafter due to the higher freshwater inventory that reduces the availability of nutrient below the ice (see section 5.3.1). The contribution of ice algal production to the total annual production is reduced due to a shorter production season: ice algal production starts at approximately the same time of the year, i.e., at the end of the "winter night", but ends earlier in the future simulations due to earlier ice melt.

The simulated *e*-ratio (calculated for each year and then averaged over the period) increases in the future projections (see Table 5.2). This increase results from the greater increase in secondary production relative to primary production, which results from the longer subsurface bloom that favors zooplankton development. In the model, the contribution of zooplankton to the detrital pool via fecal pellets and mortality is proportional to the zooplankton biomass. On the other hand, there is little change in the proportion of the flux of diatoms to the fast-sinking detritus pool in the future projections due to the decrease in the relative importance of the spring bloom (when sedimentation of phytoplankton aggregates are more important), at the expense of the subsurface bloom. The contribution of zooplankton to the detritus pool (relative to the phytoplankton contribution) increases from 41% in the present-day simulation to 44% in the 2090 period.

5.4. Discussion

Few observations are available from the modelling site to compare directly with the "present day" model results, but our results are generally within the ranges of published observations. Simulated annual primary production (between 20.1 and 26.7 g-C m^{-2} yr^{-1}, including ice algal production, see Table 5.1) falls within the range of estimates for the Mackenzie shelf and other Arctic shelves (15 to 50 g-C m^{-2} yr^{-1} [Subba Rao and Platt, 1984; Legendre et al., 1992; Macdonald et al., 1987, 1998; Carmack et al., 2004; Sakshaug, 2004]). Ice thickness and surface salinities are also in the range reported for this region [e.g., Moore et al., 1992; Melling, 1993; Macdonald et al., 1995]. The increase in simulated ice-free days on the shelf during the 1974 to 1992 period (0.54 days per year) is similar to the observed increase in number of melt days (0.53 days per year) over perennial ice between 1979 and 1996 [Smith, 1998]. The downscaling technique we use provides the best available projection of local forcing. We are thus confident that our model, calibrated with biological observations in the Beaufort Sea (Chapter 4), is a useful tool to investigate how changes in annual sea ice (thickness and duration) and freshwater flux may affect primary productivity.

5.4.1 Changes in primary production

Global marine primary production is expected to decrease with climate change due mostly to an increase in surface layer stratification (resulting both from surface warming and freshening, depending of the region) inhibiting entrainment of nutrients from below [e.g., Bopp et al., 2001; Boyd and Doney, 2002; LeQuéré et al., 2003]. When removing the 1997-98 El Niño data from analysis, satellite observations indeed indicate a decline in global ocean annual primary production since the early 1980's, which is attributed to both surface ocean warming [Gregg et al., 2003; Behrenfeld et al., 2006] and a decrease in atmospheric iron deposition [Gregg et al., 2003]. However, such a decline was not observed when looking at high latitudes only [e.g., Behrenfeld et al., 2006]. Primary production in many high-latitude regions is light limited due to deep mixing depth. These high-latitude regions are generally salinity stratified and thus less affected by future warming than lower-latitude oceanic regions [see Carmack, 2007]. However, the

freshwater flux in the Arctic is also expected to increase with climate change, thus leading to a reduction of the mixed layer depth and to a lengthening of the growing season in these regions. Bopp et al. [2001] indeed simulated an increase in productivity and export production at high latitudes with their model (up to 10% over 75 years, starting at present day). However, their results apply mainly to the Southern Ocean, as the Arctic Ocean is not well resolved with their GCM. Moreover, most Arctic shelves (except for the Barents Sea) are already strongly stratified and are nutrient, rather than light, limited [e.g., Carmack et al., 2004]. In this context, an increased stratification does not promote an increase in productivity. Even though the mechanisms differ (lengthening of the subsurface bloom duration), our projected increase in total primary production for the Beaufort Sea shelf (9%) is of the same order of magnitude as that of Bopp et al. [2001]. However, some changes that are difficult to predict could influence the model results: (1) changes in the amount and seasonality of river runoff, (2) changes in the concentration of the subsurface nutrient pool, (3) changes in the frequency of storms, (4) changes in the timing and coupling between primary and secondary production, (5) a shift in dominant species or functional groups, (6) changes in ice cover concentration and in sea ice redistribution by winds, and (7) changes in water turbidity. Next, we explore the potential influence that some of these aspects could have on our estimates of future primary production.

5.4.2 Freshwater runoff

Both the amount and seasonality of river runoff are expected to change in the future. The amplitude of the annual freshet is expected to decrease [Carmack and Macdonald, 2002] due to earlier onset of snowmelt and to thawing of permafrost [Anisimov et al., 2001; Lawrence and Slater, 2005]. The latter, combined with an increase in precipitation [Miller and Russell, 2000; Wu et al., 2005], would lead to an increase in annual runoff. The freshwater flux to the surface mixed layer can affect the delivery of nutrients from the subsurface pool through its effect on stratification, but the local flux of freshwater is difficult to predict. The estimated increase in freshwater runoff that we use is derived from predictions made for all Arctic Ocean rivers, but changes in runoff will likely differ between regions. Peterson et al. [2002] observed a 7% increase in the average annual

discharge of freshwater from the six largest Eurasian rivers for the 1936 to 1999 period, with a larger increase in the last 30 years, while Déry and Wood [2005] observed no significant trends in North American river discharge to the western Arctic Ocean for the 1964 to 2003 period, and Stewart [2000] observed a slight decrease in Mackenzie River discharge over the last few decades. The Mackenzie River runoff could thus remain unchanged in the future or increase less than estimated for our simulations, which could allow deeper wind mixing on the Beaufort Sea shelf and increased nutrient supply leading to an increase in primary production larger than the 15% we obtained. A decrease in local freshwater amount could also occur through advection of sea ice or freshwater towards the basin. Thinner ice cover can be advected away from the shelf more easily after break-up, reducing *in situ* ice melt. Additionally, increasing areas of open water on the shelf seas, resulting from the reduction of the perennial pack ice extent, combined with favorable winds, provide a greater opportunity for runoff to escape the shelves to the open ocean [Guay et al., 2001; Macdonald et al., 2002; Melling, 1993; Maslanik et al., 1999]. On the other hand, the potential continuation of the increase in freshwater storage in the Canada Basin [Proshutinsky et al., 2005], which is linked to amplification of the Northern Annular mode [NAM, e.g., Peterson et al., 2006], could eventually increase the stratification on the shelf. It has indeed been argued that an increase in greenhouse gas could result in lower Arctic surface pressures through its effect on the polar stratospheric vortex [see Serreze and Francis, 2006 and references therein].

To examine the potential effect of a lower supply of freshwater to the modelling area, due either to a runoff lower than predicted or to redistribution by winds, we conducted sensitivity simulations with reduced freshwater flux. In the first sensitivity simulation (FWpres), we apply the present-day (1983) freshwater flux to both future periods (i.e. no increase in freshwater flux in 2050 and 2090). In the second simulation (WindAdv), the freshwater flux is reduced to a fixed value of 0.05 g m^{-2} s^{-1} for the months of September and October to simulate freshwater removal from the shelf by fall winds (see Figure 5.10 and Table 5.2). And finally, to examine the effect of an earlier freshet resulting from the earlier onset of snowmelt, we conducted a simulation (Freshet) without the one month lag in runoff that was applied in the model to account for the travel time of the river flow

between the river runoff measurement site (Arctic Red River) and the modelling site (section 4.3.2, page 82). The exact change in the future timing of the river freshet is not known but the average temperature simulated by CGCM2 in our study area reaches positive values two and three weeks earlier in 2050 and 2090 compared with 1983, which gives an idea of the difference in snowmelt onset. The primary production increases by about 3% in the reduced freshwater flux scenarios in 2050 (representing a 10% increase relative to 1983), due to a deepening of the winter mixed layer (see Figure 5.10 and Table 5.2) that leads to greater nutrient replenishment in the surface layer. On the other hand, the increase in primary production is negligible in the 2090 sensitivity simulations. Lengthening of the open water period leads to deeper subsurface blooms. This deepening of the subsurface bloom leads to nutrient being depleted at greater depths during summer. The combination of a reduction in winter mixing depth (compared to the 1983 and 2050 periods) with a deeper nutrient pool leads to reduced replenishment of nutrient in the surface layer and explains the small sensitivity of primary production results to changes in the freshwater flux in 2090.

The season in which the lengthening of the ice-free water period takes place (spring versus fall) thus has important consequences on primary production of the Beaufort Sea shelf. If the bulk of the increase in open water days was shifted towards fall, the more intense and frequent storms during that season could favor the input of nutrients into the mixed layer, directly from upwelling and mixing or indirectly by pre-conditioning shelf waters to deeper winter convective mixing [Melling and Moore, 1995], and could lead to higher production.

5.4.3 Changes in the nutrient pool

Our results show that the amount of freshwater present in the surface mixed layer influences the supply of nutrients from deeper nutrient-rich layers through winter convection and wind mixing. In the Canada Basin, the maximum nutrient concentration occurs at a salinity of ~33.1 (middle halocline), between depths of 100 to 200 m [e.g., Kinney et al., 1970; Coachman and Barnes, 1961]. This high concentration of nutrients results from ventilation of the halocline with Pacific waters transported through and

"transformed" over the Bering and Chukchi Seas in winter, at a time when nutrient uptake by phytoplankton is low and when regeneration is occurring at depth near the shelf bottom [Coachman and Barnes, 1961; Codispoti et al., 2005; Mathis et al., 2007]. The upper halocline, just below the mixed layer, is supplied by inflow from the Pacific Ocean that transits through the Bering Strait and across the Chukchi Shelf in the productive summer season, thus having a lower nutrient concentration than the middle halocline waters below. Upwelling events have the potential to transport these nutrient-rich halocline waters onto the shelf where they can be mixed with the surface layer [see Carmack et al., 2004; Williams et al., 2006]. At the bottom of the model domain, the concentration of nutrients below the mixed layer is restored to its initial value (~30 mmol-Si m^{-3} and 14 mmol-N m^{-3} at a salinity of ~32.6, see Figures 4.5 and 4.6) for all the simulations. However, both the concentration of nutrients in the halocline and their delivery to the shelf through upwelling could change in the future.

The location of the ice edge relative to the shelf break exerts control of the upwelling of halocline water onto the shelf [Carmack and Chapman, 2003]. These authors argue that upwelling is more intense when the ice edge is beyond the shelf break, a situation that could occur more often with climate change with the reduction of the perennial ice pack extent. Increased upwelling of nutrient-rich waters could enhance biological production if these nutrients are subsequently mixed with surface layer water. Moreover, the nutrient maximum (middle halocline) became more shallow between the mid-80s and the mid-90s [McLaughlin et al., 2002, 2004], thereby moving closer to the depth of the Mackenzie shelf break (~100 m). If this shallowing persists, middle halocline water could be advected onto the shelf more often. However, the concentration of the middle halocline nutrient maximum could also decrease, as observed off the Siberian shelf [McLaughlin et al., 2002, 2004], making it difficult to predict the final net effect. The Bering and Chukchi Seas are also sites of denitrification [e.g., Devol et al., 1997; Tanaka et al., 2004; Lehmann et al., 2005], which could increase with climate warming, thereby reducing the concentration of nitrate in waters that ventilate the halocline [Yamamoto-Kawai et al., 2006].

5.4.4 Export production and carbon sequestration

A change in the fraction of primary production that will be exported below the mixed layer is generally expected with climate change, but more by the alteration of the timing and coupling of environmental cycles, than by changes in their magnitudes [e.g., Carmack and Macdonald, 2002]. The rapid development of the spring bloom on Arctic shelves favors the decoupling between primary and secondary producers and the direct sinking of phytoplankton aggregates to depth [Wassmann et al., 2004 and references therein]. More intense ice algal and phytoplankton spring blooms indeed lead to higher *e*-ratios in the present day simulation. However, the reduced contribution of the ice algal and spring blooms to the total primary production and the longer subsurface bloom in the future simulations increase the coupling between the main primary and secondary producers. The repackaging of phytoplankton newly-produced in the subsurface bloom into fast-sinking fecal pellets accelerates the transfer below the mixed layer, thereby increasing the *e*-ratio. Such an acceleration of the detrital flux in association with grazing of the subsurface Chl *a* maximum was observed in the study area [Forest et al., 2007; 2008] but the representativeness of these predictions will depend on changes in water masses and their circulation. The main copepod species accounting for the bulk of the mesozooplankton biomass on the Mackenzie shelf (*C. glacialis and C. hyperboreus* [Forbes et al., 1992; Forest et al., 2008]) overwinter in the deep water of the Arctic Basin and are advected onto the outer shelves of the Chukchi and Beaufort Seas in the summer after their ascent back into surface waters [Ashjian et al., 2003; Lane et al., and references therein]. It is uncertain how changes in circulation resulting from climate warming will affect the dominance of one species over another. In a changing climate, advection of Pacific species to the Chukchi and Beaufort Sea shelves could increase, as could the advection of Arctic Basin species due to increased upwelling onto the shelf. Such a reorganization of copepod species, related to modifications in water masses and currents, has been observed in the North Atlantic [Beaugrand et al., 2002; Greene and Pershing, 2007]. If a shift in the main zooplankton species were to occur, it would not necessarily cause a change in the coupling/decoupling of phytoplankton and zooplankton development. However, it could affect export of biogenic carbon from the mixed layer,

since the type of grazer determines whether sedimentation occurs in the form of faeces or whether it is delayed until after heavy grazing [Wassmann et al., 1991].

Future changes in export production may also be decoupled from future changes in primary production due to potential changes in the proportion of recycling by the microbial loop and possible changes in phytoplankton species composition. The size composition of phytoplankton communities also influences particle export [Wassmann, 1990; Tremblay et al., 1997; Dunne et al., 2005]. However, based on our simulations, changes in community structure are unlikely to occur on the Mackenzie shelf in the near future because the increase in temperature and freshwater input prevent increased deepening of the mixed layer, which would favour non-diatom species [see Sakshaug and Walsh, 2000]. The question of interest to climate scientists is not whether export production will increase, but rather, whether biogenic carbon sequestration will. From analysis of sediment cores in the Arctic basin, Gobeil et al. [2001] found evidence of an increase in the flux of organic carbon to deep sediments over the last 50 years, which they attribute to a large-scale decrease in Arctic sea ice that increased productivity and the export of particulate organic carbon. This hypothesis is further supported by the modelling work of Katsev et al. [2006]. It thus seems that increased sequestration of biogenic carbon of marine origin is a plausible consequence of projected increases in export production.

5.5. Conclusion

Using projections of climate change generated by the Canadian Global Climate Model (CGCM2) to provide future forcing for our coupled 1D model, we have investigated the impact of a reduction in duration and thickness of sea ice cover and an increase in freshwater flux to the Canadian Beaufort Sea shelf on primary and export production. Model results show a relatively modest increase of up to 10% in average total annual primary production (per unit area) between the present day simulation and the 2050 and 2090 simulations respectively. Although a higher increase could have been expected from the lengthening of the growing season resulting from the earlier disappearance of the ice

cover, the increase in the mixed layer freshwater inventory maintains the present state of low nutrient concentrations and suppresses them even further during spring. The relative contribution of the ice algal and spring phytoplankton blooms to the annual primary production is thus reduced in the future runs. On the other hand, the duration of the subsurface bloom increases, which favors the development of the main copepod species and leads to an increase in export production (16% per unit ocean surface area between 1975-1992 and 2082-2099) that is greater than the increase in primary production. Primary production may respond differently in other high latitude regions, such as the Canadian Archipelago, where freshwater supply might be more or less important and where ice algae contribute a higher proportion to annual primary production. The larger extent of open water will also increase the spatially integrated primary production. However a 3D model of the whole Arctic basin will be necessary to address these issues.

Table 5.1. Number of open water days (OWD), total annual phytoplankton (Phyto) and ice algal (Ia) primary production, secondary production (Zoo), total annual flux of detritus below the 50 m depth horizon (Detritus) and ratio of export to total (phytoplankton + ice algal) primary production (*e*-ratio) for each year. Units are g-C m^{-2} (except for the *e*-ratio).

Year	1975	1976	1977	1978	1979	1980	1981	1982	1983	1984	1985	1986	1987	1988	1989	1990	1991	1992
OWD	104	112	127	97	119	114	128	113	107	119	105	95	114	122	113	109	119	95
Phyto	19.8	21.6	23	19.2	21.9	20.7	23.6	24	23.8	25.1	22.9	18.8	22.5	23.8	21.9	21.5	23.2	20.5
Ia	0.3	0.4	0.3	1.7	1.4	1.7	1.3	1.5	1.9	1.6	1.6	1.5	0.8	1.3	1.4	1.5	0.9	1.6
Zoo	4.6	5.2	5.5	4.4	5.2	4.7	5.5	5.7	5.7	6.2	5.6	4	5.4	5.6	5.1	5	5.5	4.7
Detritus	8.5	9.3	10.3	8.9	10.4	9.7	10.7	10.1	11.2	11.8	10.8	8.2	10	10.9	10.5	10.1	10.7	9.7
***e*-ratio**	0.42	0.42	0.44	0.43	0.44	0.43	0.43	0.4	0.44	0.44	0.44	0.41	0.43	0.43	0.45	0.44	0.44	0.44

Table 5.2. Number of open water days (OWD), maximum mixed layer depth (mld), total annual primary production (PP, phytoplankton + ice algae), contribution of ice algae to total annual primary production (Ia contrib.), secondary production (Zoo), total annual flux of detritus below the 50 m depth horizon (Det) and ratio of export to total primary production (*e*-ratio) for each year for the standard simulation as well as for the sensitivity runs using reduced freshwater fluxes and described in section 5.4.2 (FwPres, Freshet, and WindAdv).

Period	**1983**	**2050**				**2090**				**% change between periods**		
Sensitivity analysis		**Standard**	**FwPres**	**Freshet**	**WindAdv**	**Standard**	**FwPres**	**Freshet**	**WindAdv**	**1983-2050**	**2050-2090**	**1983-2090**
OWD	112	148	149	149	149	159	161	160	160	32	8	42
Max mld	31.2	25.5	28.5	29.4	28.5	21.0	23.4	23.3	23.3	-18	-18	-33
PP (g-C m^{-2})	23.4	24.8	25.6	25.7	25.6	25.5	25.6	25.5	25.5	6	3	9
Ia contrib (%)	5.4	4.1	4.0	4.0	4.0	3.0	2.9	3.0	3.0	-20	-24	-39
Zoo (g-C m^{-2})	5.2	5.6	5.9	5.9	5.9	6.2	6.2	6.1	6.1	8	9	19
Det (g-C m^{-2})	10.1	11.2	11.5	11.6	11.5	11.7	11.7	11.7	11.7	11	4	16
***e*-ratio**	0.39	0.42	0.42	0.42	0.42	0.44	0.44	0.44	0.44	7	3	10

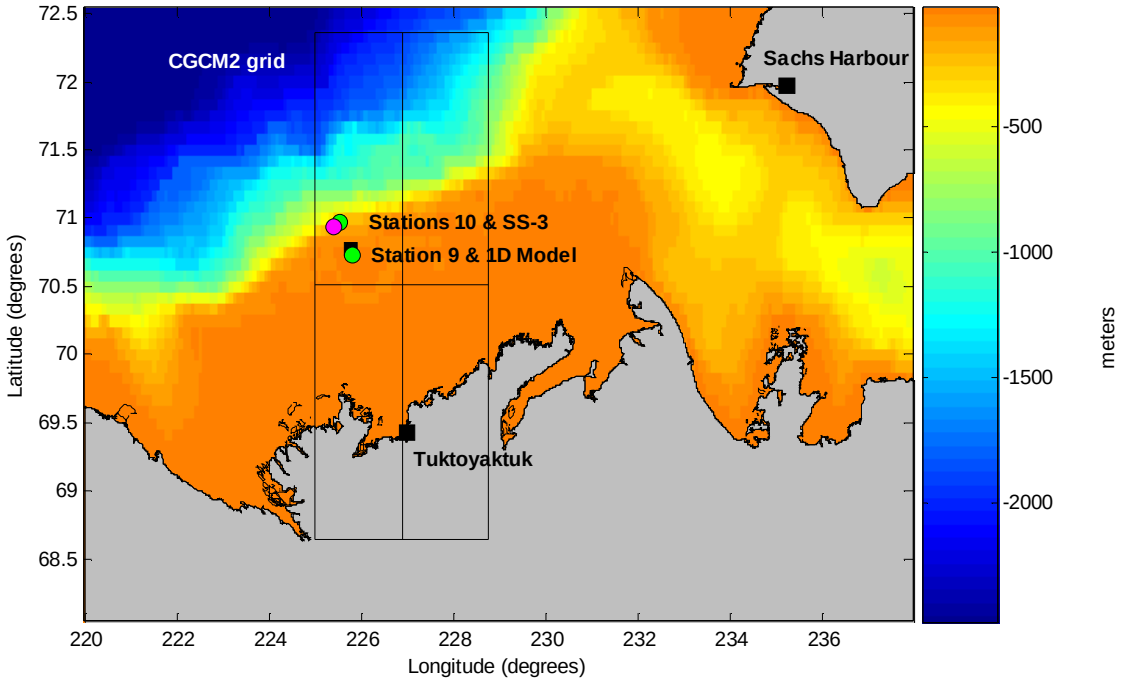

Figure 5.1. Study area and location of the meteorological station (Tuktoyaktuk), sampling stations (Stations 9 and 10 (green circles), SS-3 (magenta circle) and Sachs Harbour), modelling site (square) and of the CGCM2 grid cells used to build the forcing data for the future runs.

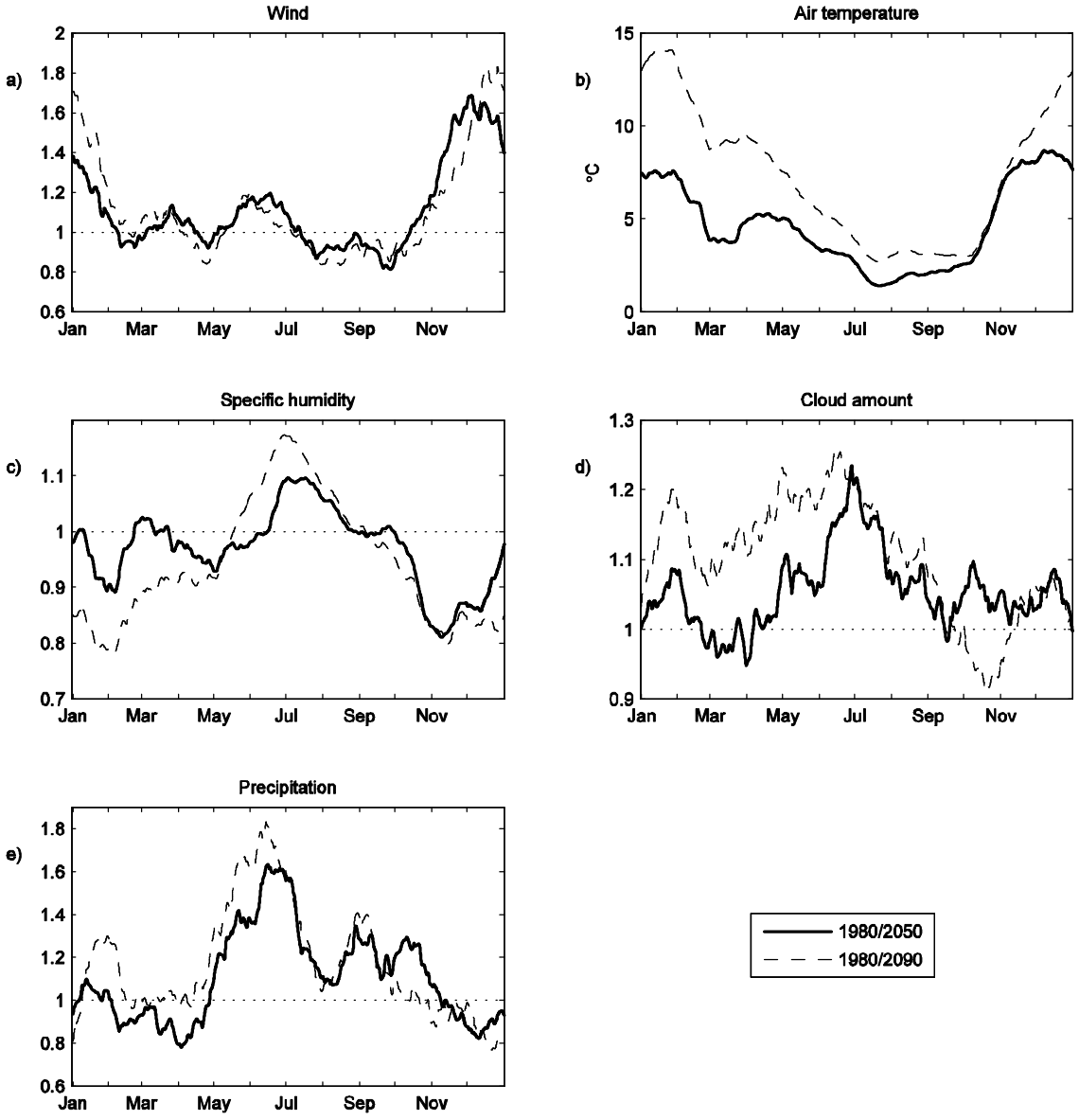

Figure 5.2. Daily mean change of different climate variables simulated with the CGCM2 between present day (1970-1989) and 2041-2060, and between present day and 2081-2100. The change is represented as a ratio, except for air temperature (°C).

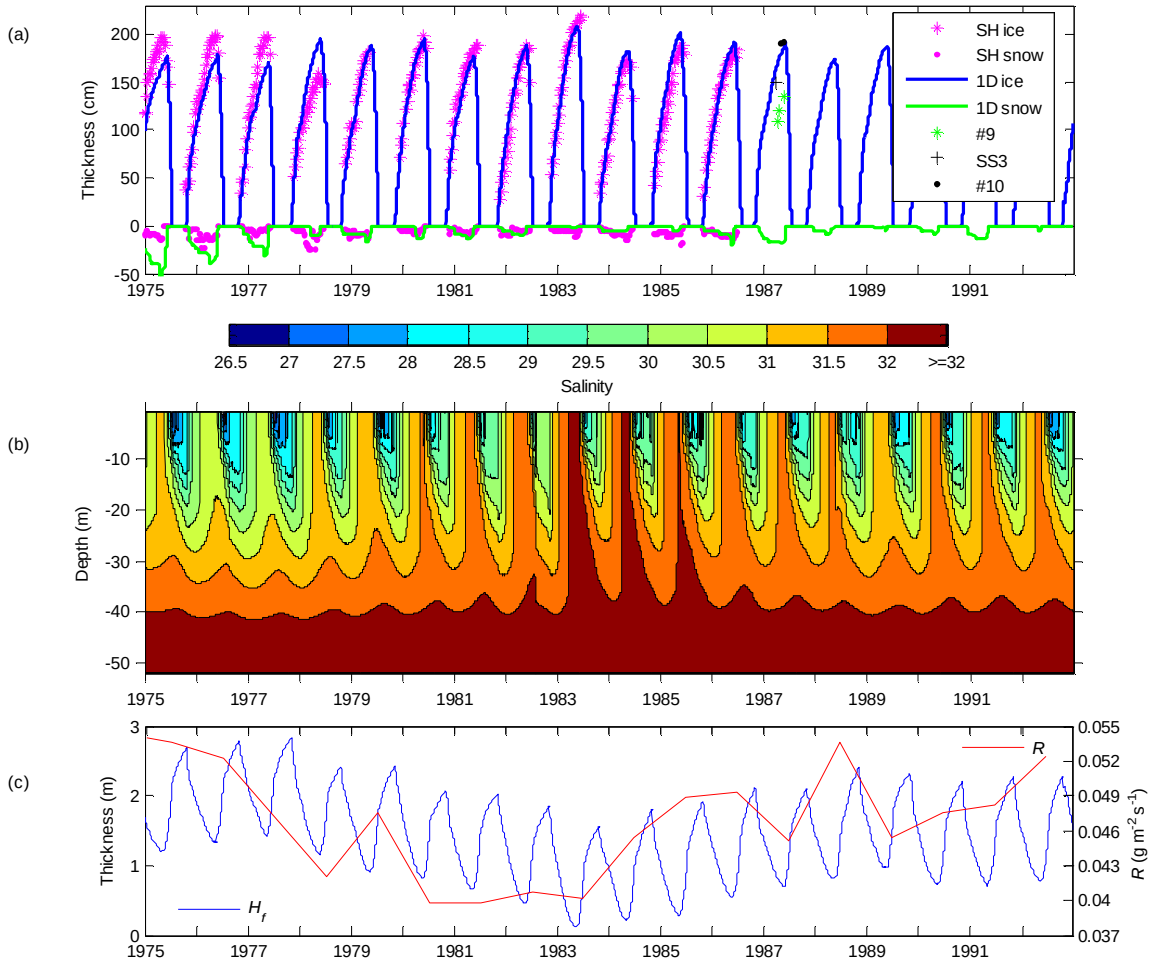

Figure 5.3. (a) Simulated (line) and observed (symbols, Sachs Harbour 'SH', and stations nearby the modelling site: '#9', '#10' and 'SS-3') ice (positive upwards) and snow (positive downwards) thicknesses, (b) mixed layer salinity for the present day period 1975-1992, and (c) mean annual flux of freshwater applied at top of the mixed layer (R), and modelled freshwater inventory (H_f in m) in the top 40 m.

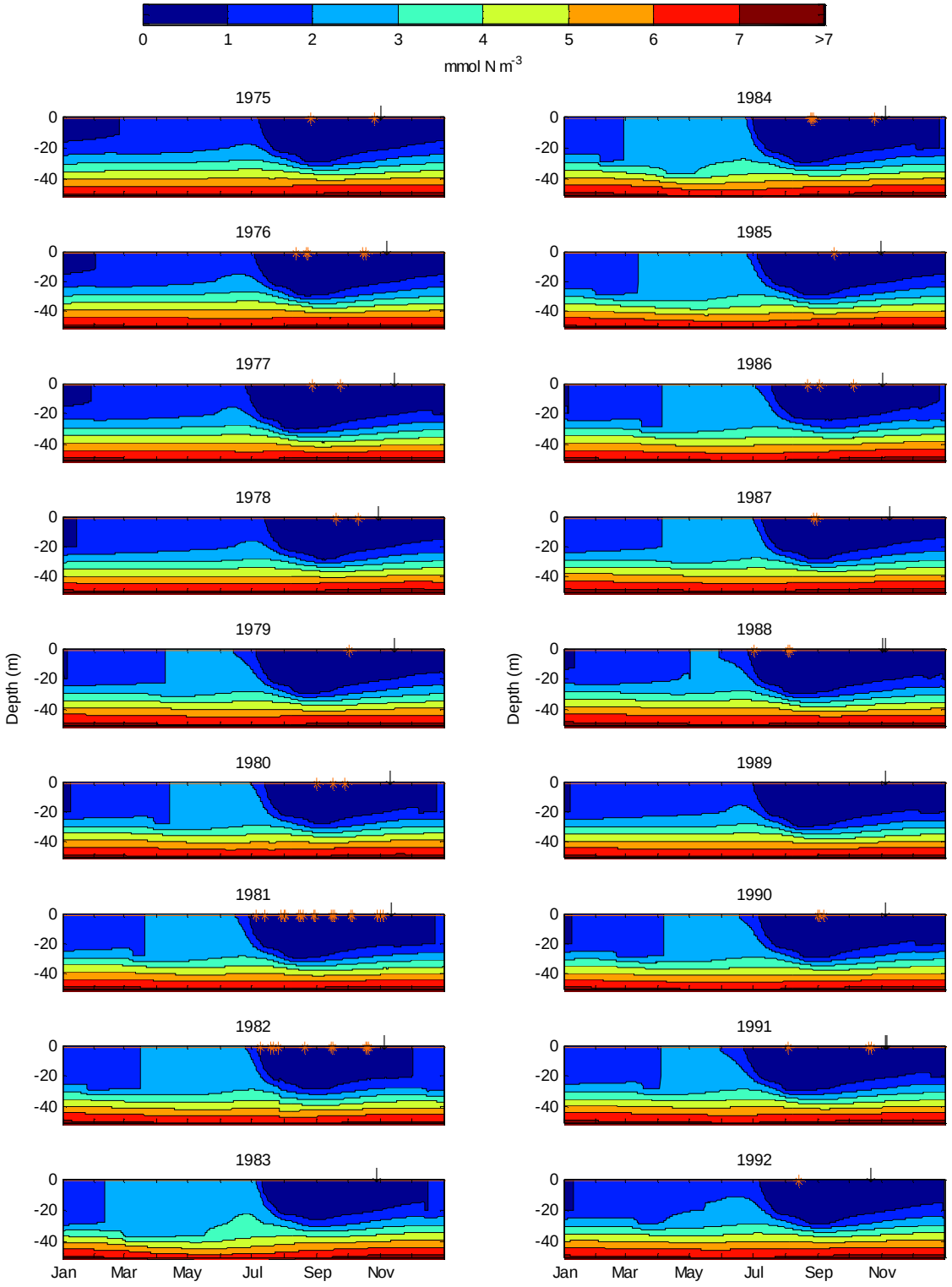

Figure 5.4. Nitrogen concentration in the top 50 m of the ocean from 1975 to 1992. The orange stars on top of the panels indicate days with winds greater than 15 m s^{-1}, while the arrows indicate the onset of ice formation (the ice sometimes melts back for a few days before growing again).

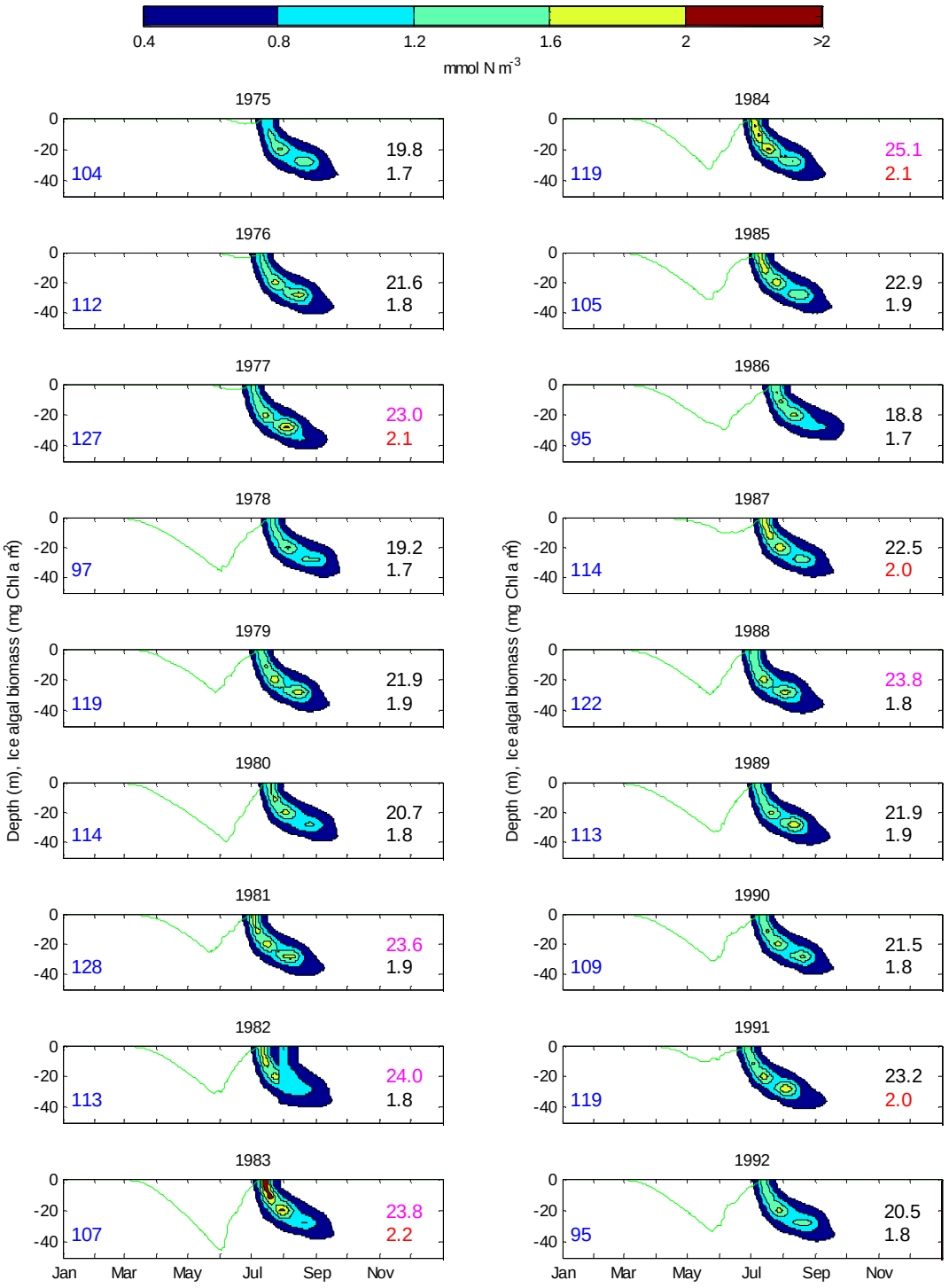

Figure 5.5. Simulated water column phytoplankton biomass for the years 1975 to 1992. For each year: ice-free period in days (lower left corner, in blue), annual phytoplankton production (lower right corner, top, mg-C m^{-2} yr^{-1}, values ≥23.5 in magenta) and maximum phytoplankton biomass concentration (lower right corner, bottom, mmol-N m^{-3}, values ≥2.0 in red) are indicated on each panel. The green line denotes ice algal biomass (in mg-Chl *a* m^{-2} projected on the depth axis).

Figure 5.6. Normalized number of modelled open water days (OWD), annual phytoplankton production (PP), and nitrogen concentration in the top 20 m between February and April.

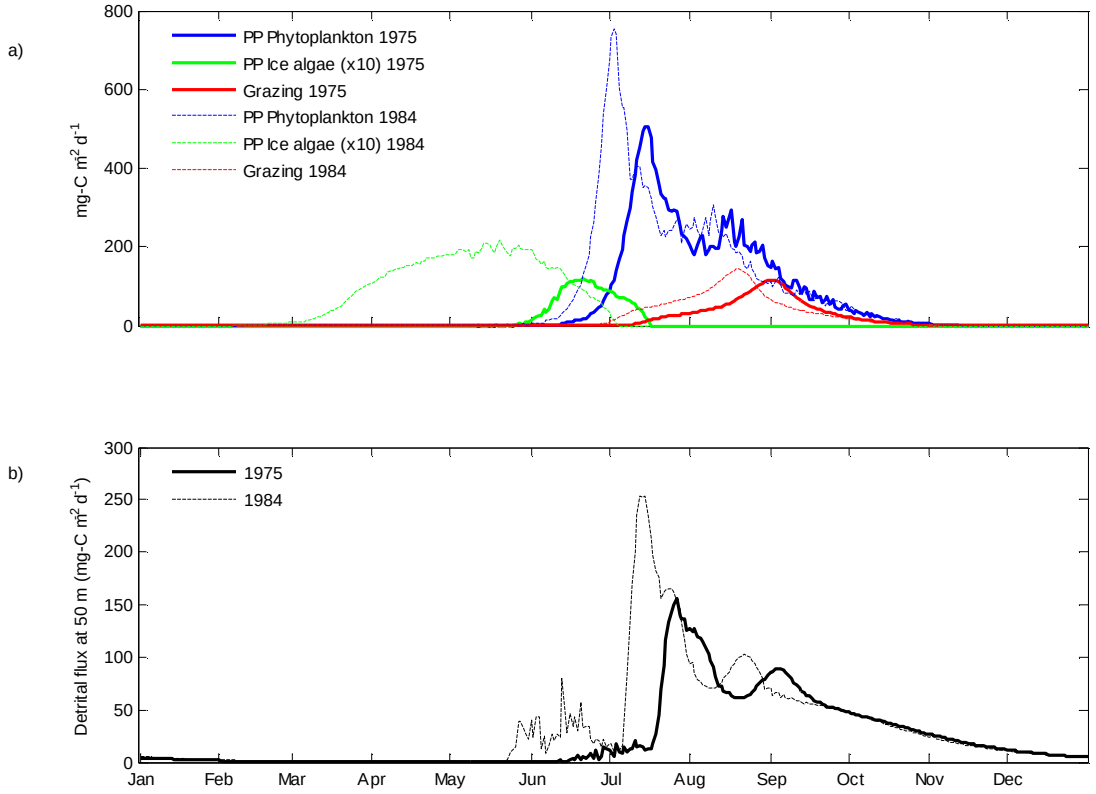

Figure 5.7. Simulated (a) depth-integrated daily production of ice algae (green, $x10^{-1}$) and phytoplankton (solid line), and simulated depth-integrated zooplankton grazing rate on phytoplankton, and (e) simulated daily flux of detritus (from all sources) below the 50 m depth horizon.

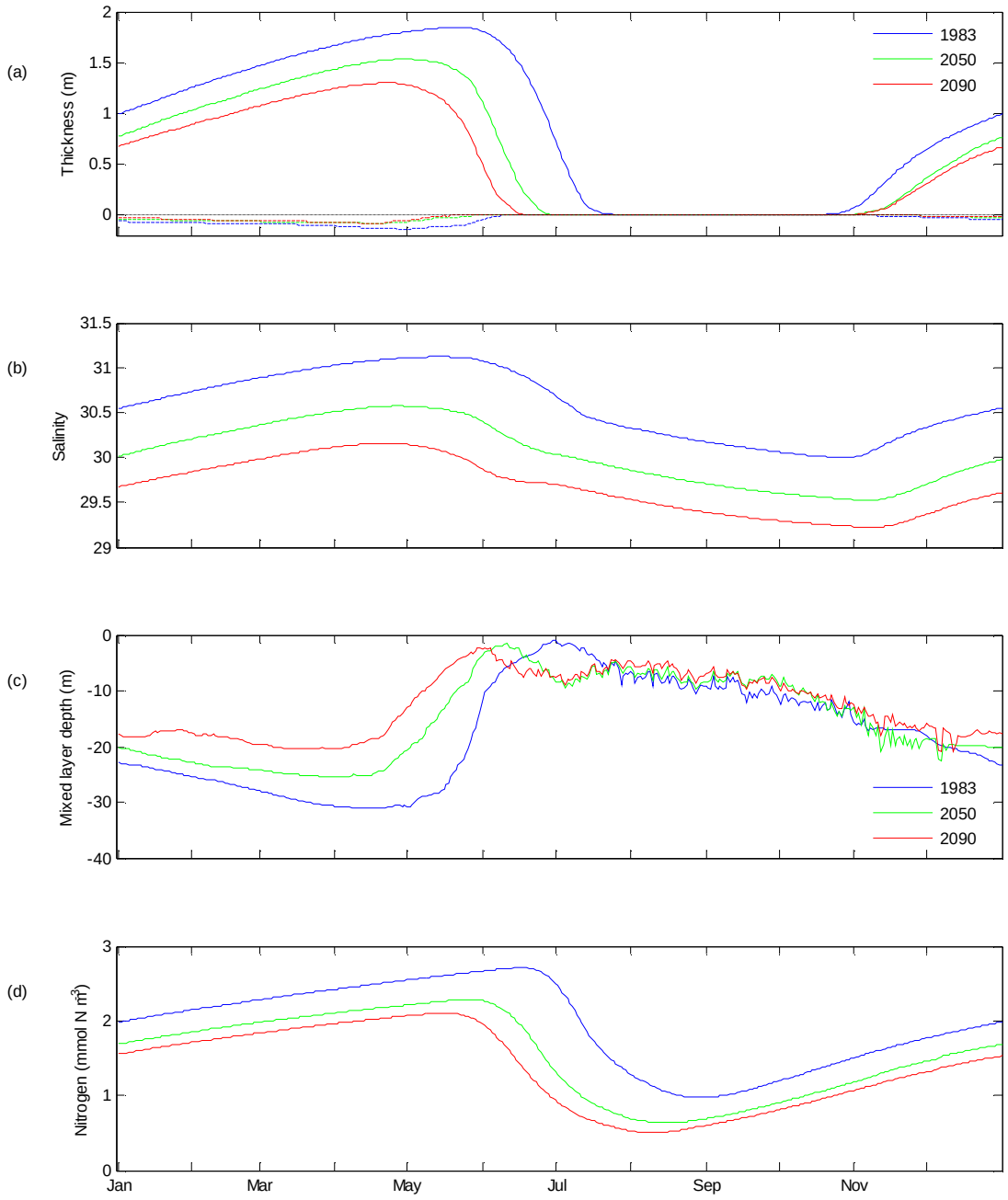

Figure 5.8. Simulated average annual cycle for each 18-year period: (a) ice (positive) and snow (negative, dashed lines) thickness, (b) salinity of the top 40 m, (c) mixed layer depth, and (d) nitrogen concentration of the top 40 m.

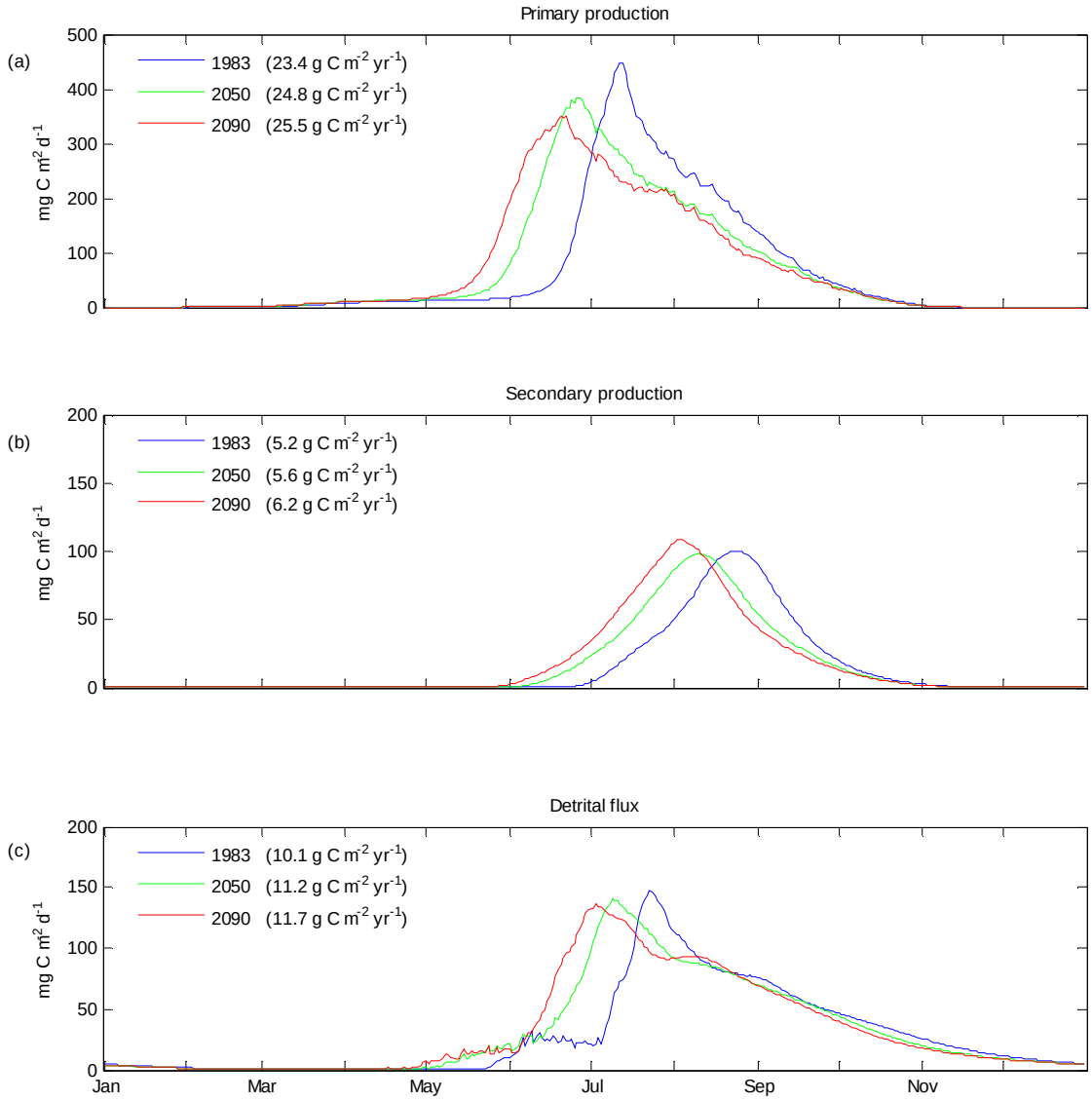

Figure 5.9. Simulated average annual cycle for each period: (a) depth-integrated primary production (phytoplankton and ice algae), (b) depth-integrated zooplankton production, and (c) flux of detritus below the 50 m depth horizon.

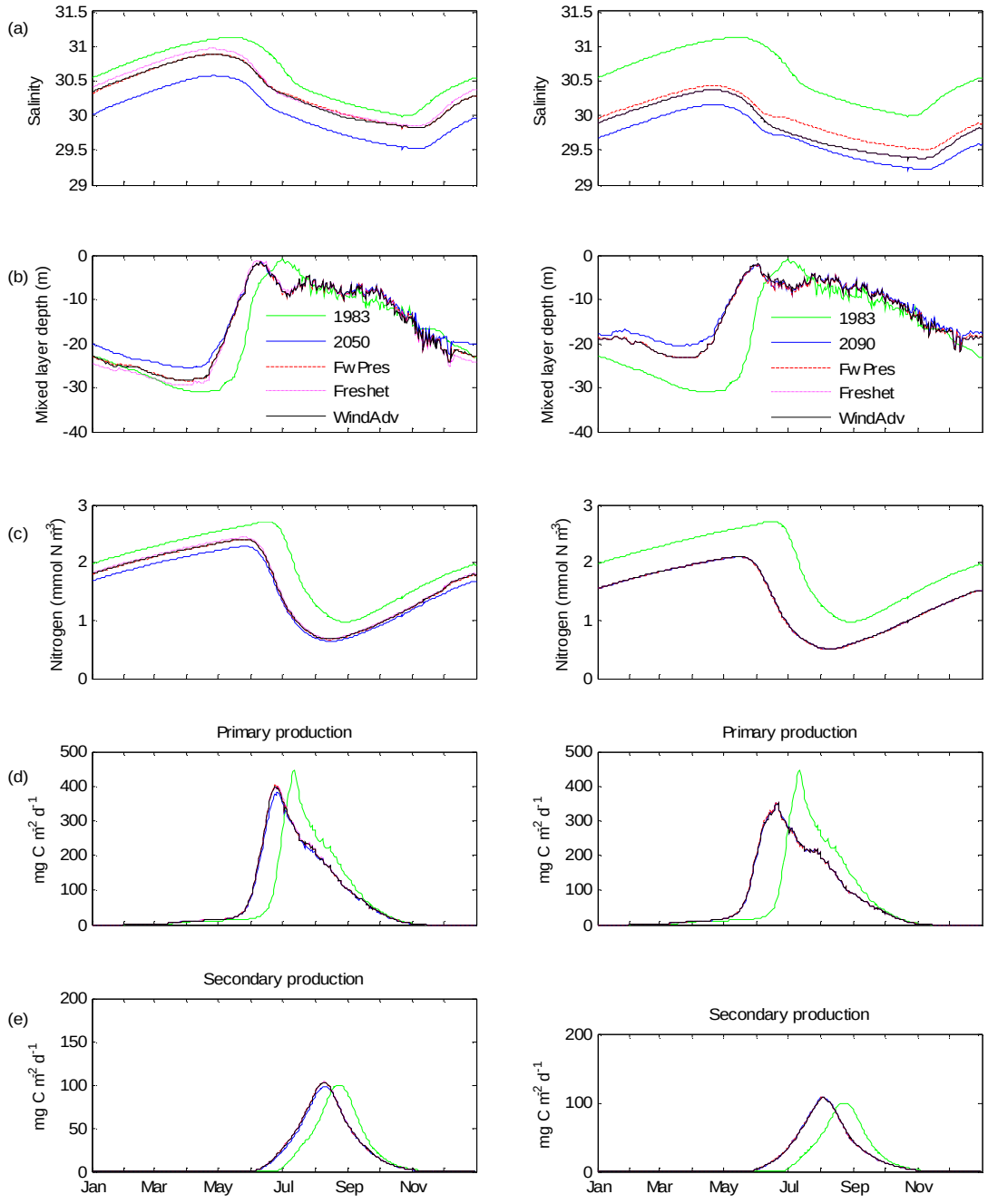

Figure 5.10. Simulated average annual cycle for each period of: (a) salinity of the top 40 m, (b) mixed layer depth, (c) nitrogen concentration of the top 40 m, (d) depth-integrated primary production (phytoplankton and ice algae), and (e) depth-integrated zooplankton production, for 1983 and 2050 (left), and 1983 and 2090 (right) for the standard simulations as well as for the sensitivity runs using reduced freshwater fluxes (FwPres, Freshet, and WindAdv, see Table 5.2 and section 5.4.2). In rows c, d, and e, all four simulations for 2090 (right) are identical and appear to be one curve.

6. Discussion and conclusions

The coupled sea ice-ocean-biological 1D model developed in this thesis is, to my knowledge, the first model that dynamically couples the sea ice physical, optical, and biological properties with the ocean physical and biological properties in the Arctic. The physically-based approach (inclusion of an ice algal loss term related to the ice growth rate, as well as the detailed treatment of the boundary layer between the upper ocean and underside of the sea ice) to understanding the temporal patterns observed in ice algae is also novel, and as mentioned by an anonymous reviewer of the ice algae paper (Chapter 3), it "represents an important advance in our understanding of sea ice ecology". In addition, the primary production predictions found in this thesis are the first ones obtained with the use of a coupled model in the Arctic (again to my knowledge).

6.1 Model Results

The model proves to be a useful tool to study the interactions between sea-ice cover dynamics and biological processes, and explains observations in the difficult to sample Arctic shelves environment. The model simulations confirm and emphasize the importance of the bottom sea ice growth rate (positive and negative) in controlling the accumulation of ice algae at the bottom of the ice, as suggested by Legendre et al. [1991] and Gosselin et al. [1997]. Cota et al. [1987] suggested that fluctuations in the supply of nutrient resulting from changes in the thickness of the molecular sublayer with the fortnightly tides were responsible for the fluctuations in ice algal biomass observed at the bottom of Resolute's first-year sea ice. The model results show that the ice algal biomass does fluctuate with the fortnight changes in the thickness of the molecular sublayer through an interplay between the heat fluxes, causing bottom ice melt rate, and the nutrient fluxes, rather than through the nutrient supply only as suggested by Cota et al. [1987]. Although tides in the Beaufort Sea are much weaker than in Resolute and nutrient concentration in the mixed layer is low year-round, the modelled ice algal biomasses for the Beaufort Sea compare well with data from the surrounding area, demonstrating the validity of the model in different first-year sea ice environments.

An important result of this study is the high contribution in some years of the phytoplankton spring bloom to the annual primary production on the Beaufort Sea shelf, when conditions the previous fall lead to higher nutrient replenishment in the mixed layer by wind and winter convective mixing [Melling and Moore, 1995]. The importance of the spring bloom to the annual primary production is not well-supported by observations, largely because of the difficulties in making observations as the ice breaks up and open water develops: e.g. Carmack et al. [2004] did not observe a strong spring bloom in 1987, but they could easily have missed it due to the large sampling gap. Similarly, Tremblay et al. [2008] and Forest et al. [2008] did not observe an important surface spring bloom in 2004 in a nearby area (Cape Bathurst Polynya), even though they had a good temporal coverage. However, as shown in the present day 18-year simulation in Chapter 5, the surface spring bloom is not important every year. This is well illustrated in Arrigo and Van Dijken [2004] who observed an important surface bloom in the spring of 1998 in Cape Bathurst polynya, but not in the following years (1999 to 2002). Their results should however be used with care since their chl *a* concentration estimates appear to be contaminated with chromophoric DOM [Ben Mustapha and Larouche, 2008]. Also, the full impact of fall storms on freshwater and pack ice advection, upwelling and mixing on the shelf (and thus on the nutrient supply to the mixed layer and primary production) cannot be properly addressed with a 1D model and will require the development of a 3D shelf model.

Another important finding is the future decrease of the relative importance of the phytoplankton spring bloom compared with the subsurface bloom, resulting mainly from the increased stratification that reduces the depth of winter convective mixing, and thus nutrient replenishment in the surface layer prior to the spring bloom. This shift in the relative importance of the surface vs. subsurface bloom could lead to a greater underestimation of chl *a* concentration and primary production estimates using satellite sensors, such as in Pabi et al. [2008], since the subsurface chl *a* maximum is not detected by these sensors. This effect of stratification on the projected Beaufort Sea shelf primary production could be representative of other Arctic Shelf Seas affected by high freshwater

runoff such as the Laptev and Siberian Seas. However, each shelf is unique and extrapolation of results from one shelf to the other should be made with caution [e.g., Carmack et al., 2006]. It is also unclear how primary production in the central Arctic will be affected by the decrease in the minimum summer extent of Arctic sea ice (and eventual disappearance of the summer multi-year ice pack). Although the latter will undoubtedly lead to an increase both in the length of the ice-free period and in the total area integral of primary and export production, the nutrient concentration in the surface waters of the central Arctic Ocean is low [Gradinger, 1999] and will limit an increase in primary production. However, a subsurface bloom might develop due to the increase in light availability, and a looser winter ice pack could favor episodic supply of nutrients to the mixed layer through storm-driven mixing [Yang et al., 2004]. However, regardless of the increase in the total area of ice-free water and episodic winter mixing events, the results of this thesis suggest that the strong stratification of Arctic waters will prevent any significant increase in total primary production in the future, unless there are significant increases during the ice-free season in the entrainment of nutrients into the surface layer through increased wind mixing.

6.2 Future work

The biological model was kept simple in order to be coupled to a large-scale 3D ocean model without requiring unreasonable computing time. A next step would thus be to couple the biological model to a 3D shelf model. The present scarcity of observations makes it difficult to build initial and boundary conditions for a 3D biological model as well as to validate it, but current projects in the Arctic will certainly help. The output of a general circulation model (GCM) could however provide forcing for the shelf model. An important addition to such a model would be a snow component (including snow redistribution by wind), as snow remains the most important variable to improve in the model presented in this thesis. Snow cover controls ice growth rate and the amount and timing of light availability at the underside of the ice, which in turn regulate ice algal bloom onset, biomass accumulation, and termination of the ice algal bloom (this study and Mundy et al. [2005]). The snow cover also controls the onset and magnitude of the

phytoplankton spring bloom, through its effect on winter convective mixing and timing of ice disappearance.

Although the simulated detrital flux is comparable with the mean annual particulate organic carbon flux estimated from sequential sediment traps (Chapter 4), the microbial loop (small phytoplankton and zooplankton, dissolved organic matter (DOM), NH_4 and bacteria) could be added explicitly in the biological model. This loop appears to contribute more to primary production and export production than previously believed [Garneau et al., 2008]. DOM concentrations in Arctic rivers are among the highest in the world [Dittmar and Kattner, 2003]. Dissolved organic carbon (DOC) supplied by these rivers has traditionally been considered refractory but new studies question this assumption and suggest that DOC delivered by rivers during the spring freshet would be more labile [Holmes et al., 2008; and references therein]. Similarly, Garneau et al. [2008] found that some areas of the Mackenzie shelf environment could be a source of CO_2 due to high bacterial production, and they suggest that the bacterial to primary production ratio could increase in the future due to the increase in allochthonous substrate supplied by rivers. The simulated detrital flux could also be improved with the addition of a zooplankton life-history model to better resolve the coupling between phytoplankton and zooplankton production.

The ice algal model could also be refined to include the production of dissolved organic carbon (DOC) and extracellular polymeric substances (EPS) by ice algae and their subsequent recycling by bacteria, which appears to play an important role in organic carbon cycling within the sea ice [Krembs et al., 2002; Riedel et al., 2006, 2007, 2008]. EPS are sticky and play an important role in cell aggregation and sinking. Although ice algae do not represent a significant fraction of annual primary production (and this fraction is expected to decrease in the future), their actual influence on the export of organic carbon could be significant. A refinement of the sea ice and ice algal components of the model could also allow the study of CO_2 gas fluxes through the ice. Sea ice has generally been considered to impede gas exchange between the ocean and the atmosphere. However, recent studies indicate that exchange could occur through sea ice,

with a net atmospheric uptake by sea ice during the spring/summer period most likely driven by increased photosynthetic activity by ice algae and under ice phytoplankton [Semiletov et al., 2004].

Alternatively to refining the model to study particular aspects at a smaller scale, the biological component could be coupled, as such, to a 3D model of the whole Arctic Ocean to simulate differences in the spatial pattern of primary production and biogenic material export in the different shelf seas. The ice algal (sea ice) model should however be developed further to include the multi-year ice habitat found in the central ocean. The more porous multi-year ice is indeed inhabited throughout its entire thickness and with distinct communities at the surface, in the interior and at the bottom [e.g., Gradinger, 1999].

Finally, the statistical downscaling method used in this thesis to provide forcing for the future projections is limited by the ability of the global model (GCM) to represent important meso-scale features and processes. In the long term, dynamical downscaling, where the output from one (or more) global climate model(s) is used to force a finer resolution regional climate model that can represent physical processes more accurately on regional scales [e.g., Liang et al., 2008], should be developed. Both of these methods will benefit from the continuously improving representation of the Arctic Ocean in GCMs, which in general have difficulties in reproducing observed sea ice cover [e.g., Parkinson et al., 2006, and references therein].

7. Bibliography

Aagaard, K. (1984), The Beaufort undercurrent, in *The Alaskan Beaufort Sea; Ecosystems and Environments*, edited by P. W. Barnes, D. M. Schell, and E. Reimnitz, pp. 47-71, Academic Press.

Aagard, K., and E. C. Carmack (1994), The Arctic Ocean and climate: a perspective, in *The Polar Oceans and Their Role in Shaping the Global Environment*, Geophysical Monograph Series, Volume 85, edited by O. M. Johannessen, R. D. Muench, and J. E. Overland, pp. 5-20, American Geophysical Union, Washington D.C.

Aagaard K., L. K. Coachman, and E. C. Carmack (1981), On the halocline of the Arctic Ocean, *Deep-Sea Res. Part A, 28*, 3821-3827.

ACIA (2005), Arctic Climate Impact Assessment, 1038 pp., Cambridge University Press, New York.

Ackley, S. F., and C. W. Sullivan (1994), Physical controls on the development and characteristics of Antarctic sea ice biological communities - a review and synthesis, *Deep-Sea Res. I, 41*(10), 1583-1604.

Anderson, M. R., and S. D. Drobot (2001), Spatial and temporal variability in snowmelt onset over Arctic sea ice, *Ann. Glaciol., 33*, 74-78.

Anderson, L.G., and S. Kaltin (2001), Carbon fluxes in the Arctic Ocean – potential impact by climate change, *Polar Res., 20*(2), 225-232.

Anderson, L. G., E. P. Jones, and J. H. Swift (2003), Export production in the central Arctic Ocean evaluated from phosphate deficits, *J. Geophys. Res, 108*(C6), 3199, doi: 10.1029/2001JC001057.

Andreas, E. L. (1987), A theory for the scalar roughness and the scalar transfer coefficients over snow and sea ice, *Boundary-Layer Meteorol., 38*, 159-184.

Ahlenius, H., K. Johnsen, and C. Nelleman (Eds) (2005), *Vital Arctic Graphics*, UNEP/GRID-Arendal, Arendal, Norway, 43 pp.

Anisimov, O., B. Fitzharris, J. O. Hagen, R. Jefferies, H. Marchant, F. Nelson, T. Prowse, and D. G. Vaughan (2001), Polar regions (Arctic and Antarctic), in *Climate Change 2001: Impacts, Adaptation, and Vulnerability*, Intergovernmental Panel on Climate Change, edited by J. J. McCarthy, O. F. Canziani, N. A. Leary, D. J. Dokken, and K. S. White, pp. 801-841, Cambridge University Press, Cambridge.

Applin, K. R. (1987), The diffusion of dissolved silica in dilute aqueous solution, *Geochim. Cosmochim. Acta, 51*, 2147-2151.

Arrigo, K. R., J. N. Kremer, and C. W. Sullivan (1993), A simulated Antarctic fast-ice ecosystem. *J. Geophys. Res., 98*(C4), 6929-6946.

Arrigo, K. R., G. L. Van Dijken (2004), Annual cycles of sea ice and phytoplankton in Cape Bathurst polynya, southeastern Beaufort Sea, Canadian Arctic, *Geophys. Res. Lett., 31*, L08304, doi:10.1029/2003GL018978.

Ashjian, C. J., R. G. Campbell, H. E. Welch, M. Butler, and D. Van Keuren (2003), Annual cycle in abundance, distribution, and size in relation to hydrography of important copepod species in the western Arctic Ocean, *Deep-Sea Res. I, 50*, 1235-1261.

Barry, R. G. (1989), The present climate of the Arctic Ocean and possible past and future states, in *The Arctic Seas: Climatology, Oceanography, Geology, and Biology*, edited by Y. Herman, pp. 1-46, Van Nostrand Reinhold Company, New-York, 888 pp.

Beaugrand, G., P. C. Reid, F. Ibañez, J. A. Lindley, and M. Edwards (2002), Reorganization of North Atlantic marine copepod biodiversity and climate. *Science, 296*, 1692-1694.

Behrenfeld, M. J., R. T. O'Malley, D. A. Siegel, C. R. McClain, J. L. Sarmiento, G. C. Feldman, A. J. Milligan, P. G. Falkowski, R. M. Letelier, and E. S. Boss (2006), Climate-driven trends in contemporary ocean productivity, *Nature, 444*, 752-755.

Ben Mustapha, S., and P. Larouche (2008), Evaluation of MODIS and SeaWiFS ocean color algorithms in the canadian arctic waters: the Cape Bathurst polynya, Proceedings of IGARSS' 08, Boston, USA, 7-11 July 2008.

Bidle, K. D., and F. Azam (1999), Accelerated dissolution of diatom silica by marine bacterial assemblages, *Nature, 397*, 508-512.

Bopp, L., P. Monfray, O. Aumont, J.-L. Dufresne, H. Le Treut, G. Madec, L. Terray, and J. C. Orr (2001), Potential impact of climate change on marine export production, *Global Biogeochem. Cycles, 15*(1), 81-99.

Boyd, P. W., and S. C. Doney (2002) Modeliing regional responses by marine pelagic ecosystems to global climate change, *Geophys. Res. Lett.*, *29*(16), 1806, doi: 10.1029/2001GL014130.

Brown, R. D., and P. Cote (1992), Interannual variability of landfast ice thickness in the Canadian High Arctic, 1950-89, *Arctic, 45*, 273-284.

Carmack, E. C. (1990), Large-scale physical oceanography of polar oceans, in *Polar Oceanography, Part A: Physical Science*, edited by W. O. Smith Jr., pp. 171-222, Academic Press Inc., San Diego.

Carmack, E. C. (2000), The Arctic Ocean's freshwater budget: sources, storage and export, in *The Freshwater Budget of the Arctic Ocean*, edited by E. L. Lewis, pp. 91-126, NATO, ASI Series.

Carmack, E., and D. C. Chapman (2003), Wind-driven shelf/basin exchange on an Arctic shelf: The joint roles of ice cover extent and shelf-break bathymetry, *Geophys. Res. Lett., 30*(14), 1778, doi:10.1029/2003GL017526.

Carmack, E. C., and E. A. Kulikov (1998), Wind-forced upwelling and internal Kelvin wave generation in Mackenzie Canyon, Beaufort Sea, *J. Geophys. Res., 103*(C9), 18447-18458.

Carmack, E. C., and R. W. Macdonald (2002), Oceanography of the Canadian shelf of the Beaufort Sea: a setting for marine life, *Arctic, 55*, Suppl. 1, 29-45.

Carmack, E., D. Barber, J. Christensen, R. Macdonald, B. Rudels, E. Sakshaug (2006), Climate variability and physical forcing of the food webs and the carbon budget on panarctic shelves, *Progress in Oceanography*, 71, 145–181.

Carmack, E. C., R. W. Macdonald, and S. E. Jasper (2004), Pelagic phytoplankton productivity on Canadian shelf of the Beaufort Sea, *Mar. Ecol. Prog. Ser., 277*, 37-50.

Carmack, E. C., J. E. Papadakis, D. M. Macdonald, and R. W. Macdonald (1989), NOGAP B.6; Volume 6, Physical data collected in the Beaufort Sea, summer, 1987, *Canadian Data Report of Hydrography and Ocean Sciences, 60*(6), 219 pp.

Carmack, E. C., R. W. Macdonald, R. G. Perkin, F. A. McLaughlin, and R. J. Pearson (1995), Evidence for warming of Atlantic water in the southern Canadian Basin of the Arctic Ocean: results from the Larsen-93 expedition, *Geophys. Res. Lett., 22*(9), 1061-1064.

Chai, F., R. C. Dugdale, T.-H. Peng, F. P. Wilkerson, and R. T. Barber (2002), One-dimensional ecosystem model of the equatorial Pacific upwelling system. Part I: model development and silicon and nitrogen cycle, *Deep-Sea Res. II, 49*, 2713-2745.

Coachman, L. K., and C. A. Barnes (1961), The contribution of Bering Sea water to the Arctic Ocean, *Arctic*, *14*, 147-161.

Codispoti, L. A., G. E. Friederich, C. M. Sakamoto, and L. I. Gordon (1991), Nutrient cycling and primary production in the marine systems of the Arctic and Antarctic, *J. Mar. Syst., 2*, 359-384.

Codispoti, L. A., C. Flagg, V. Kelly, and J. H. Swift (2005), Hydrographic conditions during the 2002 SBI process experiments, *Deep-Sea Res. II, 52*, 3199-3226.

Comiso J. C., and C. L. Parkinson (2004), Satellite-observed changes in the Arctic, *Physics Today, 57*, 38-44.

Conover, R. J., A. W. Herman, S. J. Prinsenberg, and R. Harris (1986), Distribution and feeding by the copepod *Pseudocalanus* under fast ice during the Arctic spring, *Science, 232*, 1245-1247.

Conover, R. J., G. F. Cota, W. G. Harrison, E. P. W. Horne, and R. E. H. Smith (1990), Ice/water interactions and their effect on biological oceanography in the Arctic Archipelago, in *Canada's missing dimension: science and history in the Canadian Arctic Islands*, edited by C. R. Harrington, pp. 204-228, Canadian Museum of Nature, Ottawa.

Cota, G. F., and E. P. W. Horne (1989), Physical control of Arctic ice algal production, *Mar. Ecol. Prog. Ser., 52*, 111-121.

Cota, G. F., and R. E. H. Smith (1991), Ecology of bottom ice algae: II. Dynamics, distributions and productivity, *J. Mar. Syst., 2*, 279-295.

Cota, G. F., S. J. Prinsenberg, E. B. Bennett, J. W. Loder, M. R. Lewis, J. L. Anning, N. H. F. Watson, and L. R. Harris (1987), Nutrient fluxes during extended blooms of arctic ice algae, *J. Geophys. Res., 92*, 1951-1962.

Cota, G. F., J. L. Anning, L. R. Harris, W. G. Harrison, and R. E. H. Smith (1990), Impact of ice algae on inorganic nutrients in seawater and sea ice in Barrow Strait, NWT, Canada, during spring, *Can. J. Fish. Aquat. Sci., 47*, 1402-1415.

Cota, G. F., L. Legendre, M. Gosselin, and R. G. Ingram (1991), Ecology of bottom ice algae: I. Environmental controls and variability, *J. Mar. Syst., 2*, 257-277.

Cota, G. F., L. R. Pomeroy, W. G. Harrison, E. P. Jones, F. Peters, W. M. Sheldon Jr, and T. R. Weingartner (1996), Nutrients, primary production and microbial heterotrophy in the southeastern Chukchi Sea: Arctic summer nutrient depletion and heterotrophy, *Mar. Ecol. Prog. Ser., 135*(1-3), 247-258.

Curry, J. A., J. L. Schramm, and E. E. Ebert (1995), Sea ice-albedo climate feedback mechanism, *J. Clim., 8*, 240–247.

Crawford, G., L. Padman, and M. McPhee (1999), Turbulent mixing in Barrow Strait, *Cont. Shelf Res., 19*, 205-245.

Davis, J., and R. Benner (2005), Seasonal trends in the abundance, composition and bioavailability of particulate and dissolved organic matter in the Chukchi/Beaufort Seas and western Canada Basin, *Deep-Sea Res. II, 52*, 3396-3410.

Davis, J., and R. Benner (2007), Quantitative estimates of labile and semi-labile dissolved organic carbon in the Western Arctic Ocean: a molecular approach, *Limnol. Oceanogr., 52*(6), 2434-2444.

Denman, K. L., and M. A. Peña (1999), A coupled 1-D biological/physical model of the northeast subarctic Pacific Ocean with iron limitation, *Deep-Sea Res. II, 46*, 2877-2908.

Déry, S. J., and E. F. Wood (2005), Decreasing river discharge in northern Canada, *Geophys. Res. Lett., 32*, L10401, doi:10.1029/2005GL022845.

Devol, A. H., L. A.Codispoti, and J. P. Christensen (1997), Summer and winter denitrification rates in western Arctic shelf sediments, *Cont. Shelf Res., 17*, 1029–1050.

Dickson, B. (1999), All change in the Arctic, *Nature, 397*, 389-391.

Dittmar, T., G. Kattner (2003), The biogeochemistry of the river and shelf ecosystem of the Arctic Ocean: a review, *Mar. Chem.*, *83*, 103-120.

Dugdale, R. C., and J. J. Goering (1967), Uptake of new and regenerated forms of nitrogen in primary productivity, *Limnol. Oceanogr., 12*, 196-206.

Dumas, J., E. Carmack, and H. Melling (2005), Climate change impacts on the Beaufort shelf landfast ice, *Cold Reg. Sci. Technol*., *42*, 41-51.

Dumas, J., G. M. Flato, R. D. Brown, and O. Saenko (2006), Future projections of landfast ice thickness and duration in the Canadian Arctic, *J. Clim.*, *19*, 5175-5189.

Dunne, J. P., R. A. Armstrong, A. Gnanadesikan, and J. L. Sarmiento (2005), Empirical and mechanistic models for the particle export ratio, *Global Biogeochem. Cycles*, 19, GB4026, doi:10.1029/2004GB002390.

Ebert, E. E., and J. A. Curry (1993), An intermediate one-dimensional thermodynamic sea ice model for investigating ice-atmosphere interactions, *J. Geophys. Res.*, *98*(C6), 10085-10109.

Ebert, E. E., J. L. Schramm, and J. A. Curry (1995), Disposition of solar radiation in sea ice and the upper ocean, *J. Geophys. Res.*, *100*(C8), 15965-15975.

Eicken, H. (1992), The role of sea ice in structuring Antarctic ecosystems, *Polar Biol.*, *12*, 3-13.

Ekwurzel, B., P. Schlosser, R. A. Mortlock, R. G. Fairbanks, and J. H. Swift (2001), River runoff, sea ice meltwater, and Pacific water distribution and mean residence times in the Arctic Ocean, *J. Geophys. Res.*, *106*(C5), 9075–9092.

Eppley, R. W. (1972), Temperature and phytoplankton growth in the sea, *Fish. Bull., 70*, 1063-1085.

Eppley, R. W., and B. J. Peterson (1979), Particulate organic matter flux and planktonic new production in the deep ocean, *Nature, 282*, 677-680.

Fissel, D. B., and H. Melling (1990), Interannual variability of oceanographic conditions in the Southeastern Beaufort Sea, *Canadian Contractor Report of Hydrography and Ocean Sciences, 35*, 102 pp.

Flato, G. M., and R. D. Brown (1996), Variability and climate sensitivity of landfast Arctic sea ice, *J. Geophys. Res., 101*(C10), 26767-25777.

Flato, G. M., and G. J. Boer (2001), Warming asymmetry in climate change simulation, *Geophys. Res. Lett., 28*, 195-198.

Flato, G. M., G. J. Boer, W. G. Lee, N. A. McFarlane, D. Ramsden, M. C. Reader, and A. J. Weaver (2000), The Canadian centre for climate modelling and analysis global coupled model and its climate, *Clim. Dyn.*, *16*, 451-467.

Forbes, J. R., R. W. Macdonald, E. C. Carmack, K. Iseki, and M. C. O'Brien (1992), Zooplankton retained in sequential sediment traps along the Beaufort Sea shelf break during winter, *Can. J. Fish. Aquat. Sci.*, *49*, 663-670.

Forest, A., M. Sampei, H. Hattori, R. Makabe, H. Sasaki, M. Fukuchi, P. Wassmann, and L. Fortier (2007), Particulate organic carbon fluxes on the slope of the Mackenzie Shelf (Beaufort Sea): Physical and biological forcing of shelf-basin exchanges, *J. Mar. Syst.*, *68*(1-2), 39-54.

Forest A., M. Sampei, R. Makabe, H. Sasaki, D. Barber, Y. Gratton, P. Wassmann, and L. Fortier (2008), The annual cycle of particulate organic carbon export in Franklin Bay (Canadian Arctic): Environmental control and food web implications, *J. Geophys. Res.*, 113. C03S05, doi:10.1029/2007JC004262.

Fortier, L., and J. K. Cochran (2008), Introduction to special section on Annual Cycles on the Arctic Ocean Shelf, *J. Geophys. Res.*, *113*, C03S00, doi:10.1029/2007JC004457.

Fortier, M., L. Fortier, C. Michel, and L. Legendre (2002), Climatic and biological forcing of the vertical flux of biogenic particles under seasonal Arctic sea ice, *Mar. Ecol. Prog. Ser.*, *225*, 1-16.

Frankenstein, G., and R. Garner (1967), Equations for determining the brine volume of sea ice from -0.5°C to -22.9°C, *J. Glaciol.*, *6*, 943-944.

Fransson, A., M. Chierici, L. G. Anderson, I. Bussmann, G. Kattner, E. P. Jones, and J. H. Swift (2001), The importance of shelf processes for the modification of chemical constituents in the waters of the Eurasian Arctic Ocean: implication for carbon fluxes, *Cont. Shelf Res.*, *21*, 225-242.

Garneau, M.-E., S. Roy, C. Lovejoy, Y. Gratton, and W. F. Vincent (2008), Seasonal dynamics of bacterial biomass and production in a coastal arctic ecosystem: Franklin Bay, western Canadian Arctic, *J. Geophys. Res.*, *113*, C07S91, doi:10.1029/2007JC004281.

Garrison, D. L., and K. R. Buck (1986), Organism losses during ice melting: A serious bias in sea ice community studies, *Polar Biol.*, *6*, 237-239.

Gobeil, C., B. Sundby, R. W. Macdonald, and J. N. Smith (2001), Recent change in organic carbon flux to Arctic Ocean deep basins: Evidence from acid volatile sulfide, manganese and rhenium discord in sediments. *Geophys. Res. Lett.*, *28*(9), 1743-1746.

Gosselin, M., L. Legendre, S. Demers, and R.G. Ingram (1985), Responses of sea-ice microalgae to climatic and fortnightly tidal energy inputs (Manitounuk Sound, Hudson Bay), *Can. J. Fish. Aquat. Sci., 42*, 999-1006.

Gosselin, M., L. Legendre, J.-C. Therriault, S. Demers, and M. Rochet (1986), Physical control of the horizontal patchiness of sea-ice microalgae, *Mar. Ecol. Prog. Ser., 29*, 289-298.

Gosselin, M., L. Legendre, J.-C. Therriault, and S. Demers (1990), Light and nutrient limitation of sea-ice microalgae (Hudson Bay, Canadian Arctic), *J. Phycol., 26*, 220-232.

Gosselin, M., M. Levasseur, P. A. Wheeler, R. A. Horner, and B. C. Booth (1997), New measurements of phytoplankton and ice algal production in the Arctic Ocean, *Deep-Sea Res. II, 44*(8), 1623-1644.

Golden, K. M. (2001), Brine percolation and the transport properties of sea ice, *Ann. Glaciol., 33*, 28-36.

Gradinger, R. (1995), Climate change and biological oceanography of the Arctic Ocean, *Phil. Trans. R. Soc. Lond. A, 352*, 277-286.

Gradinger, R. (1999), Vertical fine structure of the biomass and composition of algal communities in Arctic pack ice, *Mar. Biol., 133*, 745-754.

Gradinger, R., M. Spindler, and D. Henschel (1991), Development of Arctic sea-ice organisms under graded snow cover, *Polar Res., 10*, 295-307.

Grainger, E. H. (1975), Biological productivity of the Southern Beaufort Sea: the physical-chemical environment and the plankton, *Beaufort Sea Technical Report,* no 12a.

Grant, W. S., and R. Horner (1976), Growth responses to salinity variation in four Arctic ice diatoms, *J. Phycol., 12*, 180-185.

Gregg, W. W., M. E. Conkright, P. Ginoux, J. E. O'Reilly, and N.W. Casey (2003), Ocean primary production and climate: global decadal changes, *Geophys. Res. Lett., 30*(15), 1809, doi:10.1029/2003GL016889.

Grenfell, T. C., and G. A. Maykut (1977), The optical properties of ice and snow in the Arctic basin, *J. Glaciol., 18*(80), 445-463.

Guay, C. K. H., K. K. Falkner, R. D. Muench, M. Mensch, M. Frank, and R. Bayer (2001), Wind-driven transport pathways for Eurasian Arctic river discharge, *J. Geophys. Res., 106*(C6), 11469-11480.

Hansen, A. S., T. G. Nielsen, H. Levinsen, S. D. Madsen, T. F. Thingstad, and B. W. Hansen (2003), Impact of changing ice cover on pelagic productivity and food web structure in Disko Bay, West Greenland: a dynamic model approach, *Deep-Sea Res. I, 50*, 171-187.

Harrison, W. G., and G. F. Cota (1991), Primary production in polar waters: relation to nutrient availability, *Polar Res., 10*, 87-104.

Harrison, W. G., and T. Platt (1986), Photosynthesis-irradiance relationships in polar and temperate phytoplankton populations, *Polar Biol., 5*, 135-164.

Harrison, W. G., T. Platt, and B. Irwin (1982), Primary production and nutrient assimilation by natural phytoplankton populations of the Eastern Canadian Arctic, *Can. J. Fish. Aquat. Sci., 39*, 335-345.

Hattori, H., and H. Saito (1997), Diel changes in vertical distribution and feeding activity of copepods in ice-covered Resolute Passage, Canadian Arctic, in spring 1992, *J. Mar. Syst., 11*, 205-219.

Héquette, A., and P. R. Hill (1993), Storm-generated currents and offshore sediment transport on a sandy shoreface, Tibjak Beach, Canadian Beaufort Sea, *Mar. Geol., 113*, 283-304.

Hill, V., and G. Cota (2005), Spatial patterns of primary production on the shelf, slope and basin of the Western Arctic in 2002, *Deep-Sea Res. II, 52*, 3344-3354.

Holland, M. M., C. M. Bitz, and B. Tremblay (2006), Future abrupt reductions in the Summer Arctic sea ice, *Geophys. Res. Lett., 33*, L23503, doi:10.1029/2006GL028024.

Holland, M. M., Curry J. A., and J. L. Schramm (1997), Modeling the thermodynamics of a sea ice thickness distribution 2. Sea ice/ocean interactions, *J. Geophys. Res., 102*, 23,093-23,107.

Holloway, G., and T. Sou (2002), Has Arctic sea ice rapidly thinned?, *J. Clim., 15*, 1691-1701.

Holmes, R. H., J. W. McClelland, P. A. Raymond, B. B. Frazer, B. J. Peterson, and M. Stieglitz (2008), Lability of DOC transported by Alaskan rivers to the Arctic Ocean, *Geophys. Res. Lett., 35*, L03402, doi:10.1029/2007GL032837.

Hopky, G. E., M. J. Lawrence, D. B. Chiperzak, and S. M. McRae (1994), NOGAP B2; Data on *in situ* water irradiance, temperature and fluorescence, solar irradiance, and ice algae and related physical parameters from the Canadian Beaufort Sea shelf, 1985 to 1988, *Canadian Data Report of Fisheries and Aquatic Sciences*, 934, 112 pp.

Horner, R. A. (1985), Taxonomy of sea ice microalgae, in *Sea Ice Biota*, edited by R. A. Horner, pp. 147-158, CRC Press, Boca Raton, Florida.

Horner, R., and G. C. Schrader (1982), Relative contributions of ice algae, phytoplankton, and benthic microalgae to primary production in nearshore regions of the Beaufort Sea, *Arctic*, *35*(4), 485-503.

Hsiao, S. I. C., M. G. Foy, and D. W. Kittle (1977), Standing stock, community structure, species composition, distribution and primary production of natural populations of phytoplankton in the southern Beaufort Sea, *Can. J. Bot.*, *55*, 685-694.

Hudier, E., and G. Ingram (1994), Small-scale melt proceses governing the flushing of nutrients from a first-year sea ice, Hudson Bay, Canada, *Oceanol. Acta*, *17*, 397-405.

IPCC (2007), Climate Change 2007: The Physical Science Basis. Contribution of Working Group I to the Fourth Assessment Report of the Intergovernmental Panel on Climate Change [Solomon, S., D. Qin, M. Manning, Z. Chen, M. Marquis, K.B. Averyt, M. Tignor and H.L. Miller (eds.)]. Cambridge University Press, Cambridge, United Kingdom and New York, NY, USA, 996 pp.

Jassby, A. D., and T. Platt (1976), Mathematical formulation of the relationship between photosynthesis and light for phytoplankton, *Limnol. Oceanogr.*, *21*, 540-547.

Johannessen, O. M., E. V.Shalina, and M. W. Miles (1999), Satellite evidence for an arctic sea ice cover in transformation, *Science, 286*, 1937–1939.

Johannessen, O. M., L. Bengtsson, M. W. Miles, S. I. Kuzmina, V. A.. Semenov, G. V. Alekseev, A. P. Nagurnyi, V. F. Zakharov, L. P. Bobylev, L. H. Pettersson, K. Hasselmann, and H. P. Cattle (2004), Arctic climate change: observed and modeled temperature and sea-ice variability, *Tellus, 56*A, 328-341.

Jones, E. P., L. G. Anderson, and J. H. Swift (1998), Distribution of Atlantic and Pacific waters in the upper Arctic Ocean: implications for circulation, *Geophys. Res. Lett.*, *25*(6), 765-768.

Jones, P. D., M. New, D. E. Parker, S. Martin, and I. G. Rigor (1999), Surface air temperature and its changes over the past 150 years, *Rev. Geophys.*, *37*, 173.

Jones, E. P., J. H. Swift, L.G. Anderson, M. Lipizer, G. Civitarese, K. K. Falkner, G. Kattner, and F. McLaughlin (2003), Tracing Pacific water in the North Atlantic Ocean, *J. Geophys. Res.*, *108*(C4), 13.

Karcher, M., F. Kauker, R. Gerdes, E. Hunke, and J. Zhang (2007), On the dynamics of Atlantic Water circulation in the Arctic Ocean, *J. Geophys. Res.*, 112, C04S02, doi:10.1029/2006JC003630.

Katsev, S., B. Sundby, and A. Mucci (2006), Modeling vertical excursions of the redox boundary in sediments: Application to deep basins of the Arctic Ocean, *Limnol. Oceanogr.*, *51*(4), 1581-1593.

Kattsov, V. M., E. Källén, H. Cattle, J. Christensen, H. Drange, I. Hanssen-Bauer, T. Jóhannesen, I. Karol, J. Räisänen, G. Svensson, S. Vavulin, D. Chen, I. Polyakov, and A. Rinke (2005), Future climate change: modeling and scenarios for the Arctic, in *Arctic Climate Impact Assesment*, edited by C. Symon, L. Arris, and B. Heal, pp. 99-150, Cambridge University Press.

Kinnard, C., C. M. Zdanowicz, R. M. Koerner, and D. A. Fisher (2008), A changing Arctic seasonal ice zone: Observations from 1870–2003 and possible oceanographic consequences, *Geophys. Res. Lett.*, 35, L02507, doi:10.1029/2007GL032507.

Kinney, P., M. E. Arhelger, and D. C. Burrell (1970), Chemical characteristics of water masses in the Amerasian Basin of the Arctic Ocean, *J. Geophys. Res., 75, 4097-4104.*

Kirk, J. T. O. (Ed) (1983), *Light and Photosynthesis in Aquatic Ecosystems*, 401 pp., Cambridge Univ. Press, Cambridge.

Krembs, C., R. Gradinger, and M. Splinder (2000), Implications of brine channel geometry and surface area for the interaction of sympagic organisms in Arctic sea ice, *J. Exp. Mar. Biol. Ecol., 243*, 55-80.

Krembs, C., T. Mock, and R. Gradinger (2001), A mesocosm study on physical-biological interactions in artificial Arctic sea ice, *Polar Biol., 24*, 356-364.

Krembs, C., H. Eicken, K. Junge, and J. W. Deming (2002), High concentrations of exopolymeric substances in Arctic winter sea ice: implications for the polar ocean carbon cycle and cryoprotection of diatoms, *Deep-Sea Res. I, 49*, 2163-2181.

Kulikov, E. A., E. C. Carmack, and R. W. Macdonald (1998), Flow variability at the continental shelf break of the Mackenzie Shelf in the Beaufort Sea, *J. Geophys. Res., 103*(C6), 12725-12741.

Kulikov, E. A., A. B. Rabinovich, and E. C. Carmack (2004), Barotropic and baroclinic tidal currents on the Mackenzie shelf break in the southeastern Beaufort Sea, *J. Geophys. Res., 109*,doi:1029/2003JC001986.

Lancelot, C., E. Hannon, S. Becquevort, C. Veth, and H. J. W. De Baar (2000), Modeling phytoplankton blooms and carbon export production in the Southern Ocean: dominant controls by light and iron in the Atlantic sector in Austral spring 1992, *Deep-Sea Res. I, 47*, 1621-1662.

Large, W. G., and S. Pond (1981), Open ocean momentum flux measurements in moderate to strong winds, *J. Phys. Oceanogr., 11*, 324-336.

Lawrence, D. M., and A. G. Slater (2005), A projection of severe near-surface permafrost degradation during the 21st century, *Geophys. Res. Lett.*, 32, L24401, doi:10.1029/2005GL025080.

Laws, E. A., P. G. Falkowski, W. O. Smith Jr., H. Ducklow, and J. J. McCarthy (2000), Temperature effects on export production in the open ocean, *Global Biogeochem. Cycles, 14*(4), 1231-1246.

Legendre, L., M. Aota, K. Shirasawa, M. J. Martineau, and M. Ishikawa (1991), Crystallographic structure of sea ice along a salinity gradient and environmental control of microalgae in the brine cells, *J. Mar. Syst., 2*, 347-357.

Legendre L., S. F. Ackley, G. S. Dieckmann, B. Gulliksen, R. Horner, T. Hoshiai, I. A. Melnikov, W. S. Reeburgh, M. Spindler, and C. W. Sullivan (1992), Ecology of sea ice biota. 2. Global significance, *Polar Biol., 12*, 429-444.

Lehmann, M. F., D. M. Sigman, D. C. McCorkle, B. G. Brunelle, S. Hoffmann, M. Kienast, G. Cane, and J. Clement (2005), Origin of the deep Bering Sea nitrate deficit: Constraints from the nitrogen and oxygen isotopic composition of water column nitrate and benthic nitrate fluxes, *Global Biogeochem. Cycles., 19*, 10.1029/2005GB002508.

LeQuéré, C., O. Aumont, P. Monfray, and J. Orr (2003), Propagation of climatic events on ocean stratification, marine biology, and CO_2: Case studies over the 1979-1999 period, *J. Geophys. Res., 108*(C12), 3375, doi:10.1029/2001JC000920.

Leventer, A. (2003), Particulate flux from sea ice in polar waters, in *Sea Ice: an Introduction to its Physics, Chemistry, Biology and Geology*, edited by D. N. Thomas and G. S. Dieckmann, pp. 303-332, Blackwell Science Ltd, Oxford.

Li, Y.-H., and S. Gregory (1974), Diffusion of ions in sea water and in deep-sea sediments, *Geochim. Cosmochim. Acta, 38*, 703-714.

Liang, X.-Z, K. E. Kunkel, G. A. Meehl, R. G. Jones, and J. X. L. Wang (2008), Regional climate models downscaling analysis of general circulation models present climate biases propagation into future change projections, *Geophys. Res. Lett., 35*, L08709, doi:10.1029/2007GL032849.

Lizotte, M. P. (2003), The microbiology of sea ice, in *Sea ice: an introduction to its physics, chemistry, biology and geology*, edited by D. N. Thomas and G. S. Dieckmann, pp. 184-210, Blackwell Science Ltd, Oxford.

Loeng, H., K. Brander, E. Carmack, S. Denisenko, K. Drinkwater, B. Hansen, K. Kovacs, P. Livingston, F. McLaughlin, and E. Sakshaug (2005), Marine Sytems, in *Arctic Climate Impact Assesment*, edited by C. Symon, L. Arris, and B. Heal, pp. 453-538, Cambridge University Press.

Macdonald, R. W. (2000), Arctic estuaries and ice: a positive-negative estuarine couple, in *The Freshwater Budget of the Arctic Ocean*, edited by E. L. Lewis, pp. 383-407, NATO, ASI Series.

Macdonald, R. W., C. S. Wong, and P. E. Erickson (1987), The distribution of nutrients in the southeastern Beaufort Sea: Implication for water circulation and primary production, *J. Geophys. Res., 92*, 2939-2952.

Macdonald, D. M., L. E. Cuypers, D. McCullough, E. Carmack, and R. W. Macdonald (1988a), NOGAP B.6; Volume 2, Physical data collected in the Beaufort Sea, March - June 1987, *Canadian Data Report of Hydrography and Ocean Sciences, 60*(2), 157 pp.

Macdonald, R. W., K. Iseki, M. C. O'Brien, F. A. McLaughlin, D. McCullough, D. M. Macdonald, E. C. Carmack, M. Yunker, S. Buckingham, and G. Miskulin (1988b), NOGAP B.6; Volume 5, Chemical data collected in the Beaufort Sea and Mackenzie River Delta, March - July 1987, *Canadian Data Report of Hydrography and Ocean Sciences, 60*(5), 56 pp.

Macdonald, R. W., K. Iseki, M. C. O'Brien, F. A. McLaughlin, D. McCullough, D. M. Macdonald, E. C. Carmack, H. Adams, M. Yunker, G. Miskulin, and S. Buckingham (1988c), NOGAP B.6; Volume 4, Chemical data collected in the Beaufort Sea, summer, 1987, *Canadian Data Report of Hydrography and Ocean Sciences*, *60*(4), 103 pp.

Macdonald, R. W., E. C. Carmack, F. A. McLaughlin, K. Iseki, D. M. Macdonald, and M. C. O'Brien (1989), Composition and modification of water masses in the Mackenzie Shelf Estuary, *J. Geophys. Res., 94*(C12), 18057-18070.

Macdonald, R. W., D. W. Paton, and E. C. Carmack (1995), The freshwater budget and under-ice spreading of Mackenzie River water in the Canadian Beaufort Sea based on salinity and $^{18}O/^{16}O$ measurements in water and ice, *J. Geophys. Res., 100*, 895-919.

Macdonald, R. W., S. M. Solomon, R. E. Cranston, H. E. Welch, M. B. Yunker, and C. Gobeil (1998), A sediment and organic carbon budget for the Canadian Beaufort shelf. *Mar. Geol., 144*, 255-273.

Macdonald, R. W., E. C. Carmack, F. A. McLaughlin, K. K. Falkner, and J. H. Swift (1999), Connections among ice, runoff and atmospheric forcing in the Beaufort Gyre, *Geophys. Res. Lett., 26*(15), 2223-2226.

Macdonald, R. W., F. A. McLaughlin, and E. C. Carmack (2002), Fresh water and its sources during the SHEBA drift in the Canada Basin of the Arctic Ocean, *Deep-Sea Res. I, 49*, 1769-1785.

Macdonald, R. W., E. Sakshaug, and R Stein (2004), The Arctic Ocean: modern status and recent climate change, in *The Organic Carbon Cycle in the Arctic Ocean*, edited by R. Stein and r. W. Macdonald, pp. 6-21, Springer-Verlag, Heidelberg-Berlin-New York.

Maslanik, J. A., M. C. Serreze, and T. Agnew (1999), On the Record Reduction in 1998 Western Arctic Sea-Ice Cover, *Geophys. Res. Lett., 26*, 1905-1908.

Mathis, J. T., R. S. Pickart, D.A. Hansell, D. Kadko (2007), Eddy transport of organic carbon and nutrients from the Chukchi Shelf: Impact on the upper halocline of the western Arctic Ocean, *J. Geophys. Res., 112*, C05011, doi:10.1029/2006JC003899.

Maykut, G. A. (1985), The ice environment, in *Sea Ice Biota*, edited by R. A. Horner, pp. 21-82, CRC Press, Boca Raton, Florida.

Maykut, G. A., and P. E. Church (1973), Radiation climate of Barrow, Alaska, 1962-66, *J. Appl. Meteorol., 12*, 620-628.

Maykut, G. A., and N. Untersteiner (1971), Some results from a time-dependent thermodynamic model of sea ice, *J. Geophys. Res., 76*(6), 1550-1575.

McCullough, D., R. W. Macdonald, K. Iseki, and E. C. Carmack (1989), NOGAP B.6; Volume 3, Beaufort Sea current measurements, September 1987 – March 1988, *Canadian Data Report of Hydrography and Ocean Sciences, 60*(3), 37 pp.

McLaughlin, F. A., E. C. Carmack, R. W. Macdonald, and J. K. Bishop (1996), Physical and geochemical properties across the Atlantic/Pacific water mass front in the Southern Canadian Basin, *J. Geophys. Res., 101*(C1), 1183-1197.

McLaughlin, F. A., E. C. Carmack, R. W. Macdonald, A. J. Weaver, and J. Smith (2002), The Canada Basin, 1989-1995: upstream events and far-field effects of the Barents Sea, *J. Geophys. Res., 107*(C7), 101029-101049.

McLaughlin, F. A., E. C. Carmack, R. W. Macdonald, H. Melling, J. H. Swift, P. A. Wheeler, B. F. Sherr, and E. B. Sherr (2004), The joint roles of Pacific and Atlantic-origin waters in the Canada Basin, 1997-1998, *Deep-Sea Res. I, 51*, 107-128.

McPhee, M. G. (1990), Small-scale processes, in *Polar Oceanography. Part A. Physical Science*, edited by W. O. Smith, Jr., pp. 287-334, Academic Press Inc. San Diego.

McPhee, M. G. (1992), Turbulent heat flux in the upper ocean under sea ice, *J. Geophys. Res., 97*(C4), 5365-5379.

Meguro, H., K. Ito, and H. Fukushima (1967), Ice flora (bottom type): a mechanism of primary production in polar seas and the growth of diatoms in sea ice, *Arctic, 20*, 114-133.

Melling, H. (1993), The formation of a haline shelf front in wintertime in an ice-covered arctic sea, *Cont. Shelf Res., 101*, 1183-1197.

Melling, H. (1998), Hydrographic changes in the Canada Basin of the Arctic Ocean, 1979-1996, *J. Geophys. Res., 103*(C4), 7637-7645.

Melling, H. (2000), Exchanges of freshwater through the shallow straits of the North American Arctic, in *The Freshwater Budget of the Arctic Ocean*, edited by E. L. Lewis et al., pp. 479-502, Kluwer Academic Publishers, Dordrecht, The Netherlands.

Melling, H., and R. M. Moore (1995), Modification of halocline source waters during freezing on the Beaufort Sea shelf: evidence from oxygen isotopes and dissolved nutrients, *Cont. Shelf Res.*, *15*(1), 89-113.

Mellor, G. L., and L. Kantha (1989), An ice-ocean coupled model, *J. Geophys. Res.*, *94*(C8), 10937-10954.

Mellor, G. L., and T. Yamada (1974), A hierarchy of turbulent-closure models for planetary boundary layer, *J. Atmos. Sci., 31*, 1791-1806.

Mellor, G. L., and T. Yamada (1982), Development of a turbulence closure model for geophysical fluid problems, *Rev. Geophys Space Phys., 20*(4), 851-875.

Mellor, G. L., M. G. McPhee, and M. Steele (1986), Ice-seawater turbulent boundary layer interaction with melting or freezing, *J. Phys. Oceanogr., 16*, 1829-1846.

Melling, H. (1993), The formation of a haline shelf front in wintertime in an ice-covered arctic sea, *Cont., Shelf Res., 13*(10), 1123-1147.

Melnikov, I. A. (2000), The Arctic Sea ice ecosystem and global warming, in *Impacts of Changes in Sea Ice and Other Environmental Parameters in the Arctic*, Final Report of the Marine Mammal Commission Workshop, Alaska, 95-110.

Michel, C., L. Legendre, S. Demers, and J.-C. Therriault (1988), Photoadaptation of sea-ice microalgae in springtime: Photosynthesis and carboxylating enzymes, *Mar. Ecol. Prog. Ser., 50*, 177-185.

Michel, C., L. Legendre, R. G. Ingram, M. Gosselin, and M. Levasseur (1996), Carbon budget of sea-ice algae in spring: Evidence of a significant transfer to zooplankton grazers, *J. Geophys. Res., 101*(C8), 18345-18360.

Michel, C., L. Legendre, and S. Taguchi (1997), Coexistence of microalgal sedimentation and water column recycling in a seasonally ice-covered ecosystem (Saroma-ko Lagoon, Sea of Okhotsk, Japan), *J. Mar. Syst., 11*, 133-148.

Miller, J. R., and G. L. Russell (2000), Projected impact of climate change on the freshwater and salt budgets of the Arctic Ocean by a global climate model, *Geophys. Res. Lett., 27*(8), 1183-1186.

Moore, R. M., H. Melling, and K. R. Thompson (1992), A description of water types on the Mackenzie Shelf of the Beaufort Sea during winter, *J. Geophys. Res., 97*(C8), 12607-12618.

Moore, J. K., S. C. Doney, D. M. Glover, and I. Y. Fung (2002), Iron cycling and nutrient-limitation patterns in surface waters of the world ocean, *Deep-Sea Res. II, 49*, 463-507.

Moran, S. B., and J. N. Smith (2000), ^{234}Th as a tracer of scavenging and particle export in the Beaufort Sea, *Cont. Shelf Res., 20*, 153-167.

Morel, A., and R. C. Smith (1974), Relation between total quanta energy for aquatic photosynthesis, *Limnol. Oceanogr., 19*(4), 591-600.

Morison, J., K. Aagaard, and M. Steele (2000), Recent environmental changes in the Arctic: a review, *Arctic, 53*(4), 359-371.

Morison, J., M. Steele, and R. Andersen (1998) Hydrography of the upper Arctic Ocean measured from the nuclear submarine U.S.S. *Pargo, Deep-Sea Res. I, 45*, 15-38.

Mundy, C. J., D. G. Barber, and C. Michel (2005), Variability of snow and ice thermal, physical and optical properties pertinent to sea ice algae biomass during spring, *J. Mar. Syst., 58*, 107-120.

Murray, F. W. (1967), On the computation of saturation vapor pressure, *J. Appl. Meteorol., 6*, 203-204.

Nakicenovic, N., and R. Swart (Eds.) (2000), Emissions Scenarios. Special Report of the Intergovernmental Panel on Climate Change, 570 pp., Cambridge University Press, UK.

O'Brien, M. C., R. W. Macdonald, H. Melling, and K. Iseki (2006), Particle fluxes and geochemistry on the Canadian Beaufort Shelf: Implications for sediment transport and deposition, *Cont. Shelf Res.*, 26, 41-81.

Omstedt, A., E. C. Carmack, and R. W. Macdonald (1994), Modeling the seasonal cycle of salinity in the Mackenzie shelf/estuary, *J. Geophys. Res., 99*(C5), 10011-10021.

Overland, J. E., and M. Wang (2008), Future regional Arctic sea ice declines, *Geophys. Res. Lett.*, 34, L17705, doi:10.1029/2007GL030808.

Pabi, S., G. L. van Dijken, and K. R. Arrigo (2008), Primary production in the Arctic Ocean, 1998–2006, 2006, *J. Geophys. Res., 113*, C08005, doi:10.1029/2007JC004578

Parkinson, L., and W. M. Washington (1979), A large-scale numerical model of sea ice, *J. Geophys. Res., 84*(C1), 311-337.

Parkinson, C. L., D. J. Cavalieri, P. Gloersen, H. J. Zwally, and J. C. Comiso (1999), Arctic sea ice extents, areas, and trends, 1978-1996, *J. Geophys. Res., 104*(C9), 20837-20856.

Parkinson, C. L., K. Y. Vinnikov, and D. J. Cavalieri (2006), Evaluation of the simulation of the annual cycle of Arctic and Antarctic sea ice coverage by 11 major global climate models, *J. Geophys. Res.*, *111*, C07012, doi:10.1029/2005JC003408.

Parsons, T. R., Y. Maita, and C. M. Lalli (Eds) (1984), *A manual of chemical and biological methods for seawater analysis*, 187 pp., Pergamon Press, Oxford.

Parsons, T. R., D. G. Webb, H. Dovey, R. Haigh, M. Lawrence, and G. E. Hopky (1988), Production studies in the Mackenzie River - Beaufort Sea estuary, *Polar Biol.*, *8*, 235-239.

Parsons, T. R., D. G. Webb, B. E. Rokeby, M. Lawrence, G. E. Hopky, and D. B. Chiperzak (1989), Autotrophic and heterotrophic production in the Mackenzie River/Beaufort Sea estuary, *Polar Biol.*, *9*, 261-266.

Pegau, W. S. (2002), Inherent optical properties of the central Arctic surface waters, *J. Geophys. Res.*, *107*(C10), 8035, doi:10.1029/2000JC000382.

Perovich, D. K. (1998), The optical properties of sea ice, in *Physics of Ice-Covered Seas*, edited by M. Leppäranta, pp. 195-230, University of Helsinki, Finland.

Perovich, D. K., G. F. Cota, G. A. Maykut, and T. C. Grenfell (1993), Bio-optical observations of first-year arctic sea ice, *Geophys. Res. Lett.*, *20*, 1059-1062.

Peterson, B. J., R. M. Holmes, J. W. McClelland, C. J. Voeroesmarty, R. B. Lammers, A. I. Shiklomanov, I. A. Shiklomanov, and S. Rahmstorf (2002), Increasing river discharge to the Arctic Ocean, *Science*, *298*, 2171-2173.

Peterson, B. J., J. W. McClelland, R. Curry, R. M. Holmes, J. E. Walsh, and K. Aagaard (2006), Trajectory shifts in the Arctic and Subarctic freshwater cycle, *Science*, *313*, 1061-1066.

Petit, J. R., J. Jouzel, D. Raynaud, N. I. Barkov, J.-M. Barnola, I. Basile, M. Bender, J. Chappellaz, M. Davis, G. Delaygue, M. Delmotte, V. M. Kotlyakov, M. Legrand, V. Y. Lipenkov, C. Lorius, L. Pépin, C. Ritz, E. Saltzman, and M. Stievenard (1999), Climate and atmospheric history of the past 420000 years from the Vostok ice core, Antarctica, *Nature*, *399*, 429-436.

Platt, T., C. L. Gallegos, and W. G. Harrison (1980), Photoinhibition of photosynthesis in natural assemblages of marine phytoplankton, *J. Mar. Res.*, *38*, 687-701.

Platt, T., P. Jauhari, and D. Sathyendranath (1992), The importance and measurement of new primary production, in *Primary Productivity and Biogeochemical Cycles in the Sea*, edited by P. G. Falkowski and A. D. Woodhead, pp. 273-284, Plenum Press, New-York.

Polovina, J.J., E.A. Howell, and M. Abecassis (2008), Ocean's leats productive waters are expanding, *Geophys. Res. Lett.*, 35, L03618, doi:10.1029/2007GL031745.

Polyakov, I. V., and M. A. Johnson (2000), Arctic decadal and interdecadal variability, *Geophys. Res. Lett., 27*(24), 4097-4100.

Polyakov, I. V., A. Y. Proshutinsky, and M. A. Johnson (1999), Seasonal cycles in two regimes of Arctic climate, *J. Geophys. Res., 104*, 25761-25788.

Polyakov, I. V., G. V. Alekseev, R.V. Bekryaev, U. Bhatt, R. L. Colony, M. A. Johnson, V. P. Karklin, A. P. Makshtas, D. Walsh, and A. V. Yulin (2002), Observationally based assessment of polar amplification of global warming, *Geophys. Res. Lett., 29*(18), 1878, doi 10.1029/2001GL011111.

Polyakov, I. V., R. V. Bekryaev, G. V. Alekseev, U. Bhatt, R. L. Colony, M. A. Johnson, A. P. Makshtas, and D. Walsh (2003), Variability and trends of air temperature and pressure in the maritime Arctic, 1875-2000, *J. Clim., 16*, 2067-2077.

Prinsenberg, S. J., and E. B. Bennett (1987), Mixing and transports in Barrow Strait, the central part of the Northwest Passage, *Cont. Shelf Res., 7*, 913-935.

Prentice, I. C., G. D. Farquhar, M. J. R. Fasham, *et al*. (2001), The carbon cycle and atmospheric carbon dioxide, in *Climate Change 2001: The Scientific Basis*, Contribution of Working Group I to the Third Assessment Report of the Intergovernmental Panel on Climate Change , edited by J. T. Houghton *et al.*, pp. 183–237, Cambridge University Press, Cambridge, UK.

Proshutinsky A., J. Yang, R. Krishfield, R. Gerdes, M. Karcher, F. Kauker, and C. Koeberle, S. Hakkinen, W. Hibler, D. Holland, M. Maqueda, G. Holloway, E. Hunke, W. Maslowski, M. Steele, and J. Zhang (2005), Arctic Ocean study: synthesis of model results and observations, *EOS, Transactions of the American Geophysical Union*, *86* (40), 368-371.

Redfield A. C., B. H. Ketchum, and F. A. Richards (1963), The influence of organisms on the composition of sea-water, in *The Sea*, edited by M. N. Hill, pp. 26-77, Wiley-Interscience, New York.

Riebesell, U., I. Schloss, and V. Smetacek (1991), Aggregation of algae released from melting sea ice: implications for seeding and sedimentation, *Polar Biol.*, 11, 239-248.

Reeburgh, W. S. (1984), Fluxes associated with brine motion in growing sea ice, *Polar Biol., 3*, 29-34.

Riedel, A., C. Michel, M. Gosselin, and B. Leblanc (2008), Winter-spring dynamics in sea-ice carbon cycling in the coastal Arctic Ocean, *J. Mar. Syst.*, doi:10.1016/j.jmarsys.2008.01.003.

Riedel, A., C. Michel, M. Gosselin, and B. Leblanc (2007), Enrichment of nutrients, exopolymeric substances and microorganisms in newly formed sea ice on the Mackenzie shelf, *Mar. Ecol. Prog. Ser., 342*, 55-67.

Riedel, A., C. Michel, and M. Gosselin (2006), Seasonal study of sea-ice exopolymeric substances on the Mackenzie shelf: implications for transport of sea-ice bacteria and algae, *Aquat. Microb. Ecol., 45*, 195-206.

Reigstad, M., P. Wassmann, C. Wexels Riser, S. Øygarden, and F. Rey (2002), Variations in hydrography, nutrients and chlorophyll *a* in the marginal ice-zone and the central Barents Sea, *J. Mar. Syst., 38*, 9-29.

Rey, F., and H. Loeng (1985), The influence of ice and hydrographic conditions on the development of phytoplankton in the Barents Sea, in *Marine Biology of Polar Regions and Effects of Stress on Marine Organisms*, edited by J. S. Gray, and M. E. Christiansen, pp. 49-63, Wiley-Interscience, Chichester, UK.

Roach, A. T., K. Aagaard, C. H. Pease, S. A. Salo, T. Weingartner, V. Pavlov, and M. Kulakov (1995), Direct measurements of transport and water properties through the Bering Strait, *J. Geophys. Res., 100*(C9), 18443-18457.

Rothrock, D. A., Y. Yu, and G. A. Maykut (1999), Thinning of the Arctic sea-ice cover, *Geophys. Res. Lett., 26*(23), 3469-3472.

Rudels, B., and H. J. Friedrich (2000), The transformations of Atlantic Water in the Arctic Ocean and their significance for the freshwater budget, in *The Freshwater Budget of the Arctic Ocean*, edited by E. L. Lewis, pp. 503–532, Kluwer Academic Publishers, Dordrecht, The Netherlands.

Rudels, B., Larsson, A.-M., and P.-I. Sehlstedt (1991), Stratification and water mass formation in the Arctic Ocean: Some implications for the nutrient distribution, *Polar Res., 1*0(1), 19-31.

Rudels, B., E. P. Jones, L. G. Anderson, and G. Kattner (1994), On the intermediate depth waters of the Arctic Ocean, in *The Polar Oceans and Their Role in Shaping the Global Environment,* Geophysical Monograph Series, Volume 85, edited by O. M. Johannessen, R. D. Muench, and J. E. Overland, pp. 33-46, American Geophysical Union, Washington, D.C.

Sakshaug, E. (2004), Primary and secondary production in the Arctic Seas, in *The Organic Carbon Cycle in the Arctic Ocean*, edited by R. Stein, and R. W. Macdonald, pp. 57-81, Springer-Verlag, Heidelberg-Berlin-New York.

Sakshaug, E., and D. Slagstad (1991), Light and productivity of phytoplankton in polar marine ecosystems: a physiological view, *Polar Res., 10*, 69–85.

Sakshaug, E., and D. Slagstad (1992), Sea ice and wind: effects on primary productivity in the Barents Sea, *Atm-Ocean, 30*, 579-591.

Sakshaug, E, and J. J. Walsh (2000), Marine biology: biomass, productivity distributions and their variability in the Barents and Bering Seas, in *The Arctic: Environment, People, Policy*, edited by M. Nuttall and T. V. Callaghan, pp163-196, Harwood Academic Publishers, Australia.

Sambrotto R. N., J. J. Goering, and C. P. McRoy (1984), Large yearly production of phytoplankton in the western Bering Strait, *Science, 225*, 1147-1150.

Sarthou, G., K. R. Timmermans, S. Blain, and P. Tréguer (2005), Growth physiology and fate of diatoms in the ocean: a review, *J. Sea Res., 53*, 25-42.

SEARCH SSC (2001), *Study of Environmental Arctic Change, Science Plan*, Polar Science Center, Applied Physics Laboratory, University of Washington, Seattle, Washington, 89 pp.

Semiletov, I., A. Makshtas, and S.-I. Akasofu (2004), Atmospheric CO_2 balance: The role of Arctic sea ice, *Geophys. Res. Lett., 31*, L05121, doi:10.1029/2003GL017996.

Semtner, A. J. Jr. (1976), A model for the thermodynamic growth of sea ice in numerical investigations of climate, *J. Phys. Ocean., 6*, 379-389.

Serreze, M. C., and R. G. Barry (2005), Recent climate variability, trends and the future, in *The Arctic Climate System*, edited by M. C. Serreze, and R. G. Barry, pp 291-334, Cambridge University Press.

Serreze, M. C., and J. A. Francis (2006), The Arctic amplification debate, *Clim. Change, 76*, 241–264

Serreze, M. C., J. E. Walsh, F. S. Chapin III, T. Osterkamp, M. Dyurgerov, V. Romanovsky, W. C. Oechel, J. Morison, T. Zhang, and R. G. Barry (2000), Observational evidence of recent change in the northern high-latitude environment, *Clim. Change, 46*, 159-207.

Shimada, K., T. Kamoshida, M. Itoh, S. Nishino, E. Carmack, F. McLaughlin, S. Zimmermann, and A. Proshutinsky (2006), Pacific Ocean inflow: influence on catastrophic reduction of sea ice cover in the Arctic Ocean, *Geophys. Res. Lett.*, *33*, L08605, doi:10.1029/2005GL025624.

Shirasawa, K., and R. G. Ingram (1997), Currents and turbulent fluxes under the first-year sea ice in Resolute Passage, Northwest Territories, Canada, *J. Mar. Syst., 11*, 21-32.

Shuert, P. G., and J. J. Walsh (1993), A coupled physical-biological model of the Bering-Chukchi seas, *Cont. Shelf Res., 13*(5-6), 543-573.

Slagstad, D., and P. Wassmann (1996), Climate change and carbon flux in the Barents Sea: 3-D simulations of ice-distribution, primary production and vertical export of particulate organic matter. Memoirs of the National Institute of Polar Research, Tokyo, Special Issue *51*, 119–141.

Slagstad, D., K. Downing, F. Carlotti, and H.-J. Hirche (1999), Modelling the carbon export and air-sea flux of CO_2 in the Greenland Sea, *Deep-Sea Res. II, 46*, 1511-1530.

Smith, D.M. (1998), Recent increase in the length of the melt season of perennial Arctic sea ice, *Geophys. Res. Lett., 25*(5):655-658.

Smith, S. D. (1988), Coefficients for sea surface wind stress, heat flux, and wind profiles as a function of wind speed and temperature, *J. Geophys. Res., 93*, 15467-15472.

Smith, R. C., and K. S. Baker (1978), Optical classification of natural waters, *Limnol. Oceanogr., 23*, 260-267.

Smith, R. E. H., J. Anning, P. Clement, and G. Cota (1988), Abundance and production of ice algae in Resolute Passage, Canadian Arctic, *Mar. Ecol. Prog. Ser., 48*, 251-263.

Smith, R. E. H., W. G. Harrison, L. R. Harris, and A. W. Herman (1990), Vertical fine structure of particulate matter and nutrients in sea ice of the high Arctic, *Can. J. Fish. Aquat. Sci., 47*, 1348-1355.

Smith, R. E. H., M. Gosselin, and S. Taguchi (1997), The influence of major inorganic nutrients on the growth and physiology of high arctic ice algae, *J. Mar. Syst., 11*, 63-70.

Smith, W. Jr., M. Gosselin, L. Legendre, D. Wallace, K. Daly, and Gerhard Kattner (1997), New production in the Northeast Water Polynya: 1993, *J. Mar. Syst., 10*, 199-209.

Springer, A. M. (2000) Climate change and marine ecosystems of the western Arctic, in *Impacts of Changes in Se Ice and Other Environmental Parameters in the Arctic*, edited by H. P. Huntington, pp.11-122, Marine Mammal Commission, Bethesda, Maryland, USA.

Steele, M., and T. Boyd (1998), Retreat of the cold halocline layer in the Arctic Ocean, *J. Geophys. Res., 103*(C5), 10419-10435.

Steele, M., G. L. Mellor, and M. G. McPhee (1989), Role of the molecular sublayer in the melting or freezing of sea ice, *J. Phys. Oceanogr., 19*, 139-147.

Steele, M., J. Morison, W. Ermold, I. Rigor, M. Ortmeyer, and K. Shimada (2004), Circulation of summer Pacific halocline water in the Arctic Ocean. *J. Geophys. Res., 109*, C02027, doi:10.1029/2003JC002009.

Stewart, R. E. (2000), The variable climate of the Mackenzie river basin: its water cycle and freshwater discharge, in *The Freshwater Budget of the Arctic Ocean*, edited by E. L. Lewis et al., pp. 367-381, Kluwer Academic Publishers, Dordrecht, The Netherlands.

Stroeve, J., M. M. Holland, W. Meier, T. Scambos, and M. Serreze (2007), Arctic sea ice decline: Faster than forecast, *Geophys. Res. Lett., 34*, doi:10.1029/2007GL029703.

Stroeve, J., M. Serreze, S. Drobot, S. Gearheard, M. Holland, J. Maslanik, W. Meier, and T. Scambos (2008), Arctic Sea Ice Extent Plummets in 2007, *EOS, Transactions of the American Geophysical Union, 89* (2), 13.

Subba Rao, D. V., and T. Platt (1984), Primary production of Arctic waters, *Polar Biol., 3*(4), 191-201.

Suzuki, Y., S. Kudoh, and M. Takahashi (1997), Photosynthetic and respiratory characteristics of an Arctic ice algal community living in low light and low temperature conditions, *J. Mar. Syst., 11*, 111-121.

Tanaka, T., L. Guo, C. Deal, N. Tanaka, T. Whitledge, and A. Murata (2004), N deficiency in a well-oxygenated cold bottom water over the Bering Sea shelf: influence of sedimentary denitrification, *Cont. Shelf Res., 24*, 1271–1283.

Tennekes, H., and J. L. Lumley (Eds.) (1972), *A First Course in Turbulence*, 300 pp., MIT Press, Cambridge, Mass.

Thompson, D. W. J., and J. M. Wallace (1998), The Arctic Oscillation signature in the wintertime geopotential height and temperature fields, *Geophys. Res. Lett., 25*, 1297-1300.

Tremblay, J. E., B. Klein, L. Legendre, R. B. Rivkin, and J.-C. Therriault (1997), Estimation of *f*-ratios in oceans based on phytoplankton size structure, *Limnol. Oceanogr., 42*(3), 595-601.

Tremblay, J. E., K. Simpson, J. Martin, L. Miller, Y. Gratton, D. Barber, and N. M. Price (2008), Vertical stability and the annual dynamics of nutrients and chlorophyll fluorescence in the coastal, southeast Beaufort Sea, *J. Geophys. Res., 113*, C07S90, doi:10.1029/2007JC004547.

Tynan, C. T., and D. P. DeMaster (1997), Observations and predictions of Arctic climatic change: potential effects on marine mammals, *Arctic, 50*(4), 308-322.

Vernet, M., P. A. Matrai, and I. Andreassen (1998), Synthesis of particulate and extracellular carbon by phytoplankton at the marginal ice zone in the Barent Sea, *J. Geophys. Res., 103*(C1), 1023-1037.

Vézina, A. F., S. Demers, I. Laurion, T. Sime-Ngando, S. K. Juniper, and L. Devine (1997), Carbon flows through the microbial food web of first-year ice in Resolute Passage (Canadian High Arctic), *J. Mar. Syst., 11*, 173-189.

Vinnikov, K. Y., A. Robock, R. J. Stouffer, J. E. Walsh, C. L. Parkinson, D. J. Cavalieri, J. F. B. Mitchell, D. Garrett, and V. F. Zakharov (1999), Global warming and Northern Hemisphere sea ice extent, *Science, 286*, 1934-1937.

Von Quillfeldt, C. H. (2000), Common diatom species in Arctic spring blooms: their distribution and abundance, *Bot. Mar., 43*, 499-516.

Wallace, D. W. R., R. M. Moore, and E. P. Jones (1987), Ventilation of the Arctic Ocean cold halocline: rates of diapycnal and isopycnal transport, oxygen utilization and primary production inferred using chlorofluoromethane distributions, *Deep-Sea Res. A, 34*(12), 1957-1979.

Walsh, J. J., and D.A. Dieterle (1994), CO_2 cycling in the coastal ocean. I. A numerical analysis of the southeastern Bering Sea with applications to the Chukchi Sea and the northern Gulf of Mexico, *Prog. Oceanog., 34*, 335-392.

Walsh. J. E., and C. M. Johnson (1979), An analysis of Arctic sea ice fluctuations, 1957-77, *J. Phys. Oceanogr., 9*, 580-591.

Walsh, J. E., W. L. Chapman, and T. L. Shy (1996), Recent decrease of sea level pressure in the central Arctic, *J. Clim.*, 9, 480-486.

Walsh, J. J., D.A. Dieterle, W. Maslowski, and T. E. Whitledge (2004), Decadal shifts in biophysical forcing of Arctic marine food webs: numerical consequences, *J. Geophys. Res., 109*, C05031.

Walsh, J. J., C. P. McRoy, L. K. Coachman, J. J. Goering, J. J. Nihoul, T. E. Whitledge, T. H. Blackburn, P. L. Parker, C. D. Wirick, P. G. Shuert, , J. M. Grebmeier, A. M. Springer, R. D. Tripp, D. A. Hansell, S. Dienidi, E. Deleersnuder, K. Henriksen, B. A. Lund, P. Andersen, F. E. Muller-Karger, and K. Dean (1989), Carbon and nitrogen cycling within the Bering/Chukchi Seas, *Prog. Oceanog., 22*, 277-359.

Wassmann, P. (1990), Relationship between primary and export production in the boreal, coastal zone of the North Atlantic, *Limnol. Oceanogr., 35*, 464-471

Wassmann, P., and D. Slagstad (1993), Seasonal and annual dynamics of particulate carbon flux in the Barents Sea – A model approach, *Polar Biol., 13*, 363-372.

Wassmann, P., R. Peinert, and V. Smetacek (1991), Patterns of production and sedimentation in the boreal and polar Northeast Atlantic, in *Poceedings of the Pro Mare Symposium on the Polar Marine Ecology*, edited by E. Sakshaug, C. C. E. Hopkins, and N. A. Oritsland, pp. 209-228, Trondheim, 12-16 May 1990.

Wassmann, P., E. Bauernfeind, M. Fortier, M. Fukuchi, B. Hargrave, B. Moran, T. Noji, E.-M. Nöthig, K. Olli, R. Peinert, H. Sasaki, and V. Shevchenko (2004), Particulate organic carbon flux to the Arctic Ocean sea floor, in *The Organic Carbon Cycle in the Arctic Ocean*, edited by R. Stein and R. M. Macdonald, pp. 101-138, Springer-Verlag, Heidelberg-Berlin-New York.

Weeks, W. F., and S. F. Ackley (1986), The growth, structure, and properties of sea ice, in *The Geophysics of Sea Ice, NATO ASI Ser., Ser. B, Physics,* vol. 146, edited by N. Untersteiner, pp. 9-164, Plenum Press, New York.

Welch, H. E., and M. A. Bergmann (1989), Seasonal development of ice algae and its prediction from environmental factors near Resolute, N.W.T., Canada, *Can. J. Fish. Aquat. Sci*., *46*(10), 1793-1804.

Wheeler, P. A., M. Gosselin, E. Sherr, D. Thibeault, D. L. Kirchman, R. Benner, and T. E. Whitledge (1996), Active cycling of organic carbon in the central Arctic Ocean, *Nature, 380*, 697-699.

Williams, W. J., E. C. Carmack, K. Shimada, H. Melling, K. Aagaard, R. W. Macdonald, and R. G. Ingram (2006), Joint effect of wind and ice motion in forcing upwelling in Mackenzie Trough, Beaufort Sea, *Cont. Shelf Res., 26*, 2352-2366.

Wu, P., R. Wood, and P. Stott (2005), Human influence on increasing Arctic river discharges, *Gephys. Res. Lett., 32*, L02703, doi: 1029/2004GL021570.

Yamamoto-Kawai, M., E. Carmack, F. McLaughlin (2006), Nitrogen balance and Arctic throughflow, *Nature, 443*, 43.

Yang, J., J. Comiso, D. Walsh, R. Krishfield, and S. Honjo (2004), Storm-driven mixing and potential impact on the Arctic Ocean, *J. Geophys. Res., 109*, C04088, doi:1029/2001JC001248.

Yool, A., A. P. Martin, C. Fernandez, and D. R. Clark (2007), The significance of nitrification for oceanic new production, *Nature, 447*, 999-1002.

Zeebe, R. E., H. Eicken, D. H. Robinson, D. Wolf-Gladrow, and G. S. Dieckmann (1996), Modeling the heating and melting of sea ice through light absorption by microalgae, *J. Geophys. Res., 101*(C1), 1163-1181.

Zhang, X., and J. E.Walsh (2006), Toward a seasonally ice-covered Arctic Ocean: Scenarios from the IPCC AR4 model simulations, *J. Clim.*, 19, 1730-1747.

Vitae

Surname: Lavoie Given Names: Marie-Josée Diane

Place of birth: Rimouski, Québec, Canada

Educational Institution Attented:

Laval University	1988 to 1992
University of Quebec at Rimouski	1993 to 1997

Degrees Awarded:

BSc	Laval University	1992
MSc	University of Quebec at Rimouski	1997

Honours and Awards:

Estelle Laberge Scholarship	1995
University of Quebec at Rimouski Scholarship	1994

Publications :

Lavoie, D., K. Denman, and R. W. Macdonald (2008), Primary productivity and export fluxes on the Canadian shelf of the Beaufort Sea: a modelling study, *J. Mar. Syst.*, doi:10.1016/j.jmarsys.2008.07.007.

Lavoie, D., M. Starr, B. Zakardjian, and P. Larouche (2008), Identification of ecologically and biologically significant areas (EBSA) in the Estuary and Gulf of St. Lawrence: Primary production. DFO, Canadian Science Advisory Secretariat, Research Document, 2007/079, 33 pp.

Lavoie, D., K. Denman, and C. Michel (2005), Modelling ice algal growth and decline in a seasonally ice-covered region of the Arctic (Resolute Passage, Canadian Archipelago), *J. Geophys. Res., 110,* c11009, doi:10.1029/2005JC002922.

Simard, Y., **D. Lavoie**, and F. J. Saucier (2002), From plankton to whales: Oceanography of a traditional whale feeding ground and marine park in the St. Lawrence estuary, ICES CM 2002/N:14.

Simard, Y., **D. Lavoie,** and F. J. Saucier (2002), Channel head dynamics: capelin (Mallotus villosus) aggregation in the tidally driven upwelling system of the Saguenay - St. Lawrence Marine Park's whale feeding ground, *Can. J. Fish. Aquat. Sci., 59*(2), 197-210.

Lavoie, D., Y. Simard, and F. J. Saucier (2000), Aggregations and dispersion of krill at channel heads and shelf edges: the dynamics in the Saguenay - St. Lawrence Marine Park, *Can. J. Fish. Aquat. Sci.*, *57*, 1853-1869.

Simard, Y., and **D. Lavoie** (1999), The rich krill aggregation of the Saguenay - St. Lawrence Marine Park: hydroacoustic and geostatistical biomass estimates, structure, variability and significance for whales, *Can. J. Fish. Aquat. Sci*., *56*, 1182-1197.

Lavoie, D. (1997), *Réponse hydrodynamique de la Baie des Chaleurs au passage d'une forte tempête*, M. Sc. Thesis, University of Quebec at Rimouski, 170 pp.

Lavoie, D., Y. Simard, J. Benoit, P. Larouche, and B. Thibeault (1996), Distribution des masses d'eau à la tête du chenal Laurentien dans l'estuaire du Saint-Laurent aux étés 1994 et 1995, *Rapp. Tech. Can. Hydrogr. Sci. Océan*, *176*, x+126 pp.

Lavoie, D. (1995), Physical features of the Miramichi Estuary, in *Water, Science, and the Public: The Miramichi Ecosystem*, edited by M. Chadwick, pp. 273-277, Canadian Special Publication of Fisheries and Aquatic Sciences 123.